

Nanosatellite attitude control using magnetorquers

DIPLOMA THESIS

Conducted in partial fulfillment of the requirements for the degree of a
Diplom-Ingenieur (Dipl.-Ing.)

supervised by

Univ.-Prof. Dr. techn. A. Kugi
Dipl.-Ing. (FH) B. Bischof
Dipl.-Ing. F. Königseder

submitted at the

TU Wien

Faculty of Electrical Engineering and Information Technology
Automation and Control Institute

by

Martin Meiringer
Matriculation number 0926022
Währinger Gürtel 125/6-7
1180 Wien
Österreich

Vienna, in April 7, 2016

Preamble

This thesis is submitted in partial fulfillment of the requirements for the Diplom Ingenieur (Dipl. Ing.) degree in Energy Systems and Automation Technology at the TU Wien (Vienna University of Technology) and was carried out between 2015 and 2016 at the CDS group of the Automation and Control Institute at TU Wien.

First, I want to thank Univ.-Prof. Dr. techn. A. Kugi for giving me the opportunity to work on a topic without prior research interests of the CDS group, for his support in completing the thesis and for proofreading it.

Furthermore, I want to thank my supervisors Dipl.-Ing. (FH) B.Bischof and Dipl.-Ing. F.Königseder for giving me guidance and motivation for the work and for the very personal and fruitful collaboration.

The major thanks, however, is dedicated to my parents and family for giving me the mental support and help, not only while writing this thesis but during my whole education. In addition, I want to thank my close friends and roommates for the incredible support, especially during the most stressful periods. With you, even the hardest days at the University were no problem after all.

Last but not least, I want to thank my colleagues, who were writing their thesis at the same time, and all my friends from the Fachschaft Elektrotechnik, for the encouraging coffee breaks and discussions about work related problems.

Vienna, in April 7, 2016

Abstract

The aim of this work is to derive an attitude control system for a nanosatellite that stabilizes a defined orientation with respect to the Earth. The work is part of the *CubeSat Pegasus* project of the TU Wien *Space Team* for the international *QB50* mission.

The *CubeSat Pegasus* is built with commercial off-the-shelf hardware and uses a set of magnetic coils to generate a control torque utilizing the Earth's magnetic field. This actuation principle results in an underactuated mechanical system, because the generated torque is restricted to be perpendicular to the local magnetic field.

A mathematical framework including a general model describing the attitude dynamics of a rigid spacecraft is derived. A general formalism for satellite trajectory planning is presented and simplified for the desired task. The environment in the altitude of the satellite's orbit is described using mathematical models of the Earth's magnetic field, the Sun position, and disturbance torques. The satellite's orientation is determined using measurements of the Earth's magnetic field and the Sun's position in an Extended Kalman Filter design.

In order to achieve the given requirements while considering the hardware limitations, a sequential control strategy using two different control laws is developed. In a first control phase, the high angular velocity of the satellite at tip-off is decreased without considering the attitude. When the angular velocities get small enough, a PD control law is applied to stabilize the satellite's attitude at a pre-calculated trajectory. The stability of the control strategy is proven, using Lyapunov methods and Khalil's averaging theory. Thereby, almost global stability of the rigid spacecraft is shown.

The presented theoretical results are supported with simulations of a realistic case study including expected measurement errors. The simulation results show that the given requirements are fulfilled and a realization of the project is possible.

Kurzzusammenfassung

Die vorliegende Arbeit befasst sich mit dem Problem der Lageregelung eines Nanosatelliten. Dieser soll in einer definierten Orientierung in Bezug zur Erde stabilisiert werden. Die Arbeit wurde im Zuge des *CubeSat Pegasus* Projektes des TU Wien Space Teams durchgeführt und soll in der internationalen *QB50* Mission zum Einsatz kommen.

Der *CubeSat Pegasus* Satellit ist aus Standard-Hardware aufgebaut und mit mehreren Luftspulen ausgestattet, um durch Interaktion mit dem Erdmagnetfeld ein gewünschtes Drehmoment zu erzeugen. Diese Art der Aktuierung resultiert in einem unteraktuierten System, da nur Momente orthogonal zum lokalen Magnetfeld erzeugt werden können.

Ein allgemeines mathematisches Modell zur Beschreibung der rotatorischen Bewegung des Satelliten wird hergeleitet. Um die definierte Orientierung zu berechnen, wird eine allgemeine Methode zur Trajektorienplanung für Satelliten auf das gegebene Problem angewandt. Die Umgebungsbedingungen in der Flughöhe des Satelliten werden mit Hilfe mathematischer Modelle des Erdmagnetfeldes, der Sonnenposition und erwarteten Störungen hinreichend genau abgebildet. Die Orientierung des Satelliten wird mit Hilfe von Messungen des Erdmagnetfeldes und der Sonnenposition mittels Extended Kalman Filter geschätzt.

Um die Anforderungen an die Regelung zu erfüllen, wurde unter Berücksichtigung der bestehenden Hardwarelimitierungen eine sequentielle Regelungsstrategie bestehend aus zwei unabhängigen Regelgesetzen entwickelt. Zunächst wird mit einem einfachen Regelgesetz die hohe Winkelgeschwindigkeit des Satelliten nach dem Abwurf reduziert ohne dabei die aktuelle Lage zu berücksichtigen. Sobald die Winkelgeschwindigkeiten einen bestimmten Grenzwert unterschreiten, wird ein PD Regelgesetz zur Stabilisierung der Fluglage verwendet. Die Stabilität der Regelgesetze wird mittels Lyapunov Methoden und der Averaging Theory nach Khalil überprüft. Auf diese Weise kann die sogenannte *almost global stability* nachgewiesen werden.

Die theoretischen Ergebnisse werden mit einer realitätsnahen Simulation unter Berücksichtigung von fehlerhaften Messungen und Rauschen validiert. Die Simulationsergebnisse zeigen, dass die gestellten Anforderungen erfüllt werden und das Projekt erfolgreich umgesetzt werden kann.

Contents

List of Figures	VI
List of Tables	VIII
Nomenclature and abbreviations	IX
1 Introduction	1
1.1 Task description	2
1.2 Literature review	3
1.3 Outline of the thesis	5
2 Modeling	6
2.1 Satellite model	8
2.1.1 Quaternion kinematics	8
2.1.2 Body dynamics	10
2.2 Orbital dynamics	11
2.2.1 Orbit of the <i>QB50</i> mission	12
2.3 Environment model	15
2.3.1 Earth's magnetic field	15
2.3.2 Position of the Sun	16
2.3.3 Disturbance torques	17
2.4 Actuators and sensors	19
2.4.1 Magnetorquer design	20
2.4.2 Sensor models	22
2.5 Chapter conclusion	22
3 Attitude determination and control system	24
3.1 Detumbling control	26
3.2 Extended Kalman Filter	28
3.3 Attitude control	34
3.4 Chapter conclusion	40
4 Implementation and simulation	41
4.1 Implementation	41
4.2 Simulation results	47
4.2.1 Detumbling controller	51
4.2.2 Attitude controller	54
4.2.3 Enlarged view of stabilized flight	57
4.3 Chapter conclusion	65

5 Summary and outlook	66
A Quaternion mathematics	67
Bibliography	70

List of Figures

1.1	<i>CubeSat Pegasus</i> with expanded antennas.	2
2.1	Definition of the used reference frames.	6
2.2	The defined body reference frame of <i>CubeSat Pegasus</i>	8
2.3	About the difference between the true and mean anomaly.	12
2.4	Visualization of the defined orbital elements.	13
2.5	The definition of a Sun-synchronous orbit.	14
2.6	<i>QB50</i> orbit, expressed in the inertial coordinate system.	15
2.7	Visualization of the Earth orbiting the Sun.	17
2.8	Definition of the magnetorquer dimensions.	20
3.1	Flowchart of the proposed control strategy.	25
3.2	Block diagram of the detumbling controller in closed-loop, as used in the simulation.	26
3.3	Block diagram of the PD controller in closed-loop, as used in the simulation.	36
3.4	Eigenvalues of the averaged matrix $\bar{\Gamma}$ along the <i>QB50</i> orbit.	38
4.1	Condition (3.46) along the desired orbit.	46
4.2	Groundtrack of the simulated scenario.	47
4.3	Attitude of the satellite with respect to the inertial frame, for the full simulation time.	48
4.4	Attitude error in r.p.y. angles for the full simulation time. The dashed lines show the required pointing accuracy.	49
4.5	Angular velocity of the satellite w.r.t. the inertial frame for the full simulation.	50
4.6	Simulated gravity gradient and atmospheric drag acting on the satellite for the full simulation.	51
4.7	Angular velocity of the satellite w.r.t. the inertial frame for the detumbling phase.	52
4.8	Current for each magnetorquer (upper graph) and the power consumption (lower graph) for the detumbling phase.	53
4.9	Attitude error in r.p.y. angles for the attitude control phase. The dashed lines show the required pointing accuracy.	54
4.10	Current for each magnetorquer (upper graph) and the power consumption (lower graph) for the attitude control phase.	55
4.11	Control torques for the attitude control phase.	56
4.12	Attitude of the satellite w.r.t. the inertial frame, expressed in r.p.y. angles in a closer view.	57
4.13	Attitude error in r.p.y. angles in a closer view.	58
4.14	Control torque in the stabilized phase.	59

4.15 Gravity gradient and atmospheric drag acting on the satellite in a closer view.	60
4.16 Comparison between the fully actuated torque and the projected torque.	61
4.17 The projection of $\mathbf{u}_{B,c}$ to the effective plane, perpendicular to $\tilde{\mathbf{b}}_B$	62
4.18 Estimation error of the estimated attitude after switching to the EKF.	63
4.19 Error of the estimated angular velocities after switching to the EKF.	64

List of Tables

4.1	Simulation parameters of <i>CubeSat Pegasus</i>	41
4.2	Simulation parameters of the <i>QB50</i> orbit.	42
4.3	Simulation parameters of the environment.	42
4.4	Simulation parameters of the sensors.	43
4.5	Parameters used in the magnetorquer optimization.	44
4.6	Simulation parameters of the actuators.	44
4.7	Simulation parameters of the Extended Kalman Filter.	44
4.8	Simulation parameters of the controllers.	45

Nomenclature and abbreviations

General Notation

a	scalar variable
\mathbf{a}	vector
\mathbf{A}	matrix

Mathematical operators

\otimes	quaternion product
$\frac{d}{dt}$	time derivative
$\frac{\partial}{\partial x}$	partial derivative
mod	modulo operator
\cdot	Euclidean inner product
\times	cross product
$\ \cdot \ $	Euclidean norm
$[\otimes]$	quaternion product matrix
$[\times]$	cross product matrix
∇	vector differential operator
$\sigma(\mathbf{A})$	singular value of \mathbf{A}
$\text{CN}(A)$	condition number of \mathbf{A}

Scalars

β_{amp}	gyroscope bias amplitude
ϵ_o	obliquity
μ	gravitational parameter
ω_{PD}	angular velocity limit
ϕ	geocentric longitude
Ψ	magnetic scalar potential
ρ	atmospheric density
θ	geocentric co-latitude
ϑ	rotation angle
A	area
a	satellite's altitude
C_d	drag coefficient
G	gravitational constant
h_t	trace height
I	intensity of incoming (sun) light
K	scalar quantity in PD proof of

	stability
$k_{\Sigma}, k_{\mathbf{Q}}$	ekf gains
$k_{\mathbf{q}}, k_{\omega}, k_{\mathbf{b}}$	controller gains
l_t	trace length
l_x, l_y, l_z	satellite dimensions
M	Earth's mass
m	satellite's mass
n	number of turns
P_{η}	noise power spectral density
r_E	Earth's radius
r_O	radius of the circular orbit
R_t	electrical resistance
t	time
T_o	orbit period
t_r	relative time
T_s	sampling time
T_{trop}	tropical year
U_s	supply voltage of the actuators
V	lyapunov function candidate
v_b	satellite's velocity
w_s	space between two traces
w_t	trace width
Z_K	attractive set for the averaged system
ν	true anomaly
ν_0	mean anomaly
Ω	right ascension of the ascending node (raan)
ω	argument of perigee
a'	semimajor axis of elliptical orbit
e	orbit eccentricity
i	orbit inclination

Subscripts

ad	atmospheric drag
c	control

d	disturbance	\mathbf{r}	position vector
gc	geometric center	\mathbf{S}	magnetorquer scaling matrix
gg	gravity gradient	\mathbf{x}	state vector of the satellite model
B	body reference frame	\mathbf{z}	state vector of the averaged system
F	Earth fixed reference frame	\mathbf{i}	control current vector
I	inertial reference frame	\mathbf{J}	inertia matrix of the satellite
O	orbit reference frame	\mathbf{l}	angular momentum vector
k	discrete time index	\mathbf{m}	magnetic dipole moment
Vectors and Matrices		$\mathbf{\Gamma}$	input matrix of the satellite model
\mathbf{R}	rotation matrix	$\boldsymbol{\tau}$	torque acting on the satellite
\mathbf{q}	rotation quaternion	\mathbf{b}	magnetic field
\mathbf{I}	identity matrix	$\bar{\mathbf{b}}$	reference magnetic field
\mathbf{q}_i	identity quaternion	$\tilde{\mathbf{b}}$	measured magnetic field
\mathbf{e}	unit vector	β	gyroscope bias
\mathbf{M}	matrix quantity in PD proof of stability	$\hat{\beta}$	estimated gyroscope bias
\mathbf{N}	constant matrix	η_ω	measurement noise of the gyroscopes
\mathbf{u}	desired control action	η_b	measurement noise of the magnetometers
$\boldsymbol{\chi}$	state vector of observer model	η_s	measurement noise of the Sun sensors
σ^2	statistical variance	$\tilde{\boldsymbol{\omega}}$	measured angular velocity
ζ	estimation error	$\boldsymbol{\omega}$	angular velocity
\mathbf{Q}	model error covariance matrix	\mathbf{s}	Sun vector
\mathbf{w}	vector of disturbances	$\bar{\mathbf{s}}$	reference Sun vector
Φ, Λ	discrete system and input matrix of the observer model	$\tilde{\mathbf{s}}$	measured Sun vector
\mathbf{A}, \mathbf{B}	system and input matrix of the observer model	Abbreviations	
\mathbf{H}	measurement sensitivity matrix	<i>ADCS</i>	attitude determination and control system
\mathbf{h}	measurement function	<i>gmst</i>	Greenwich Mean Sideral Time
\mathbf{L}	Kalman gain matrix	<i>PSD</i>	power spectral density
$\boldsymbol{\Sigma}$	noise covariance matrix	<i>r.p.y.</i>	roll pitch yaw
$\delta\boldsymbol{\vartheta}$	small angular error	<i>w.r.t.</i>	with respect to
$\boldsymbol{\vartheta}$	axis-angle vector	<i>EKF</i>	Extended Kalman Filter
\mathbf{f}	force		
\mathbf{k}	Keplerian elements		
\mathbf{n}	Nadir vector		

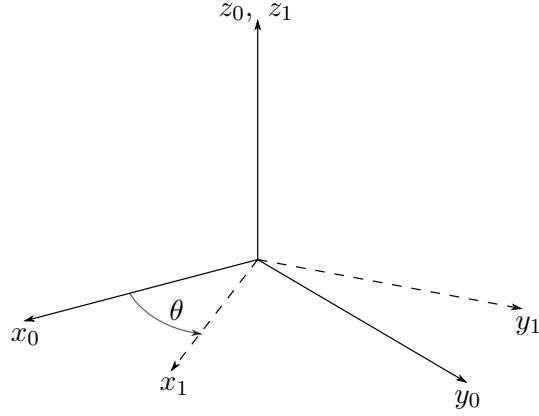
Representation of rotations

A rotation matrix describing a rotational transformation from a frame 1 to a frame 0 is denoted by \mathbf{R}_{01} . To transform a vector \mathbf{v}_1 , expressed in a reference frame 1, into the frame 0, it is premultiplied with the appropriate rotation matrix

$$\mathbf{v}_0 = \mathbf{R}_{01}\mathbf{v}_1 .$$

Basic rotations about a single frame axis x , y , z by the angle θ are furthermore denoted as

$$\mathbf{R}_{i,\theta}, i \in \{x, y, z\}.$$



An example rotation: $\mathbf{R}_{01} = \mathbf{R}_{z,\theta}$.

The notation used for rotation quaternions follows similarly. The quaternion \mathbf{q}_{01} describes the same rotation as the rotation matrix \mathbf{R}_{01} . To transform a vector \mathbf{v}_1 , expressed in a reference frame 1, into the frame 0, the vector is premultiplied with the appropriate rotation quaternion and postmultiplied with the conjugate of the appropriate quaternion, denoted with the superscript $*$, written as

$$\begin{bmatrix} 0 \\ \mathbf{v}_0 \end{bmatrix} = \mathbf{q}_{01} \otimes \begin{bmatrix} 0 \\ \mathbf{v}_1 \end{bmatrix} \otimes \mathbf{q}_{01}^*.$$

The definition of the quaternion product \otimes and the conjugate of a quaternion is given in Appendix A of this work.

Angular velocities are denoted similarly. The vector $\boldsymbol{\omega}_{01}^0$ describes the rotation of frame 1 with respect to the frame 0, expressed in the frame 0.

Throughout this work, all angular velocities are expressed with respect to their left subscript if not stated otherwise. This makes it possible to omit the additional superscript denoting the reference frame and increases the readability. Therefore, the relation

$$\boldsymbol{\omega}_{01}^0 = \boldsymbol{\omega}_{01}$$

holds.

1 Introduction

Satellites have a special image in human society. Not only in movies, books and comics the topic is omnipresent. It is a huge ambition for young researchers to bring their work out in the space and help to explore the big, dark unknown. This is also the very cornerstone of this work. Deriving an attitude control system for a nanosatellite, built by students of the TU Wien in their spare time, is an important part in the realization of the *CubeSat Pegasus* project [1].

The fascination is partly a consequence of the fact that aerospace is still a young research area. Everything started in the 1950's with the so called space race between the USSR and the USA [2]. Three important first missions deserve a short mention:

- *Sputnik 1* was the first successfully launched satellite in general. Launched in 1957 by the USSR, it had a mass of 84 kg, was operating in a Low Earth Orbit, and had a lifetime of 92 days.
- *Explorer 1* was the first successfully launched satellite by the USA in 1958. It had a mass of 14 kg, was operating in a Medium Earth Orbit, and had a lifetime of more than 12 years.
- *Vanguard 1* was the first successfully launched satellite of the nanosatellite class (mass of 1 kg to 10 kg) by the USA in 1958. It had a mass of 1.5 kg, was operating in a Medium Earth Orbit, and its lifetime can not be specified since it is still in the orbit, although not functioning anymore¹.

Unlike today it was not the intention to build small satellites, it was more an unwanted side effect of limited launching hardware. The USSR handled this issue better and also won the second big challenge in the early space race, to accomplish the first human spaceflight in history with Yuri Gagarin and the spacecraft *Costok 3KA*. Rising research activities on both sides were the result of these early challenges between the USA and the USSR. With bigger dimensions, better launching equipment, special aerospace components and high financial effort many significant missions were realized (cf. [2]). Applications like TV-satellites or satellite positioning systems are popular developments of this era and used nowadays without much thought.

The regained interest in nanosatellites since around millennium (cf. [3]) is first of all an effect of the possibility to realize relatively inexpensive missions in a relatively short time, giving young research teams and developing countries the possibilities to explore the space on their own.

Modern applications for nanosatellites vary widely. Due to their small dimensions it is

¹ *Vanguard 1* was also the first solar powered satellite and one of the major mission outcomes was the insight that the assumed atmospheric models were not sufficient.

possible to operate in much lower altitudes than big scale satellites. The so called Low Earth Orbit, defined by altitudes of 200 km to 2000 km is often the area of application for Nanosatellites [3]. Lots of satellite programs focus on observing the Earth's atmosphere² in terms of weather phenomena and air pollution. Other ideas for nanosatellite applications are worldwide internet access [4] or a space science platform to give scientists the chance to perform their experiments in a cheap and uncomplicated way [5]. Many other commercial missions are planned in the coming years, not to mention the military interest.

1.1 Task description

The aim of this work is to develop an attitude determination and control system (ADCS) for the nanosatellite class using only magnetic actuation. The ADCS is developed for the use in a standard double *CubeSat* [6] as part of the *CubeSat QB50* program [7] and is meant to be implemented in the *CubeSat Pegasus* [1] satellite built by the TU Wien *Space Team*.

The considered satellite is presented in Figure 1.1. The dimensions of the satellite body are 227 mm × 100 mm × 100 mm with a total mass of 1.622 kg.

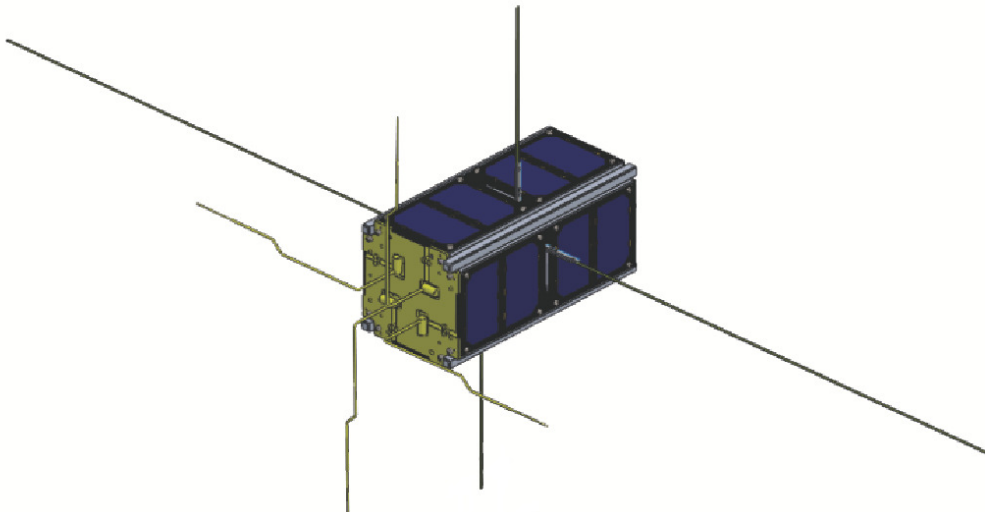


Figure 1.1: *CubeSat Pegasus* with expanded antennas. (Reprinted with the permission of the Author [8])

A control strategy has to be developed that stabilizes the satellite from an arbitrary launch attitude and high angular velocities after the satellite is released from the launching vehicle. The detaching of the satellite from the launching vehicle is referred to as tip-off throughout this thesis. Operating in a Low Earth Orbit the satellite should finally achieve a defined orientation with respect to the Earth.

²The Earth's thermosphere is located around 80 km to 500 km

A pointing accuracy of $\pm 10^\circ$ is demanded after a maximum regulation time of 3 days. These requirements are defined for the *QB50* mission orbit, which is a Sun-synchronous circular orbit with an altitude of 450 km and an inclination of 98° .

To control the satellite in space, magnetic actuators are used to generate a torque by interacting with the local Earth's magnetic field. One further task of this work is to give design suggestions for the magnetic actuators from the control engineer's point of view. The satellite is furthermore equipped with gyroscopes to measure the satellite's angular velocity, magnetometers to measure the Earth's magnetic field and photo-diodes on each surface to determine the direction of the incoming Sunlight.

1.2 Literature review

Magnetic attitude control of spacecrafts was of research interest from the beginning on. One of the first publications about magnetic attitude control was written by White et al. [9] in a feasibility study in 1961, where two-coil and three-coil configurations are investigated. Besides the research interest in magnetic control, inertia wheels were often used and already handled precisely in the early days [10]. Some satellites were also launched without attitude control at all³.

The first applications of magnetic torquers were spinning-stabilized satellites. Shigehara developed a control law where the polarity of a fixed magnetic dipole is switched [11]. Camillo investigated the application of momentum unloading of reaction wheels using magnetic torquers [12]. Magnetic torquers are also used as additional actuators for gravity gradient stabilized satellites to improve their performance and to give the possibility of controlling the yaw angle as well. Martel et al. were one of the first to make use of such a control, achieving enhanced performance of gravity gradient stabilized satellites [13]. Wen and Kreutz-Delgado [14], Cavallo [15], and Egeland and Godhavn [16] published detailed works on the problem of attitude control for fully actuated satellites. Wen and Kreutz-Delgado developed PD-like feedback controllers with optional feedforward terms in singularity-free quaternion formulation. Using Lyapunov methods, global asymptotic stability of the closed-loop system was shown. Cavallo presented a sliding manifold approach and formulated a PD feedback controller. Special attention was given to robustness since their control law was implemented in the CARINA spacecraft using thrusters as actuators. Egeland and Godhavn use passivity-based control laws known from robotic manipulators and adapted them to formulate an adaptive attitude control law for satellite control and show global convergence of the tracking error.

The main disadvantage of magnetic torquers is that the control torque can only be generated perpendicular to the local Earth's magnetic field. This issue leads to local underactuation of the spacecraft. The problem of underactuated satellite systems was investigated by Byrnes and Isidori [17]. For a spacecraft with only two thruster jets (failure case), they used nonlinear feedback to develop a control law that stabilizes the system about an attractor (in this case the principle axis of the failed jet). Krishnan [18] investigated the same problem. His main idea was to switch through a sequence of

³e. g. *Sputnik 1* was launched with no attitude control at all, equipped with antennas with spherical radiation pattern.

maneuvers and use locally stable controllers to construct a nonlinear discontinuous control law to stabilize the satellite. Later, the work of Reyhanoglu et al. [19] gave impact to the topic of underactuated systems and they confirmed Byrnes' and Isidori's statement that the underactuated spacecraft can not be asymptotically stabilized using a time-invariant continuous feedback controller.

In the case of magnetic actuation, the situation is different. Whereas the mentioned works investigate a constant underactuation, in the case of magnetic actuation a time-varying underactuation is given. Bhat [20] studied the controllability of magnetic actuated spacecrafts using nonlinear control theory. Bhat's work shows that the attitude dynamics of a magnetic actuated spacecraft in a dipole approximation of the Earth's magnetic field are controllable if the orbital plane does not coincide with the geomagnetic equatorial plane.

Musser and Ebert [21] were one of the first to develop an attitude control strategy for satellites with magnetic actuation only and without passive stabilization like gravity gradient. The main result of their work is a time-varying LQR law which ensures exponential stability of a simplified, linearized system.

Wang and Shtessel [22] formulated a nonlinear control law for satellites with magnetic actuation only. They use a backstepping concept proposed by Krstic et al. [23] and show local stability using Krasovskii-LaSalle and Floquet's theorem for time-periodic systems. Wisniewski published a nonlinear time-varying control law to globally stabilize a gravity gradient satellite [24]. First, Wisniewski derives a controller that results in four stable equilibria (because of the gravity gradient), using methods for periodic systems and assuming a periodic variation of the magnetic field. A nonlinear control law is given to drive the system to the desired equilibrium. The final control strategy shows global asymptotic closed-loop stability for the assumed time periodic magnetic field.

Lovera and Astolfi investigated the magnetic actuated spacecraft using Lyapunov methods and Khalil's averaging theory [25] in [26]. Based on the averaging theory the controllability on average is proven. Using a PD control law, they show conditions yielding to an attractive set of bounded trajectories. With the proof of local exponential stability for all trajectories starting in this attractive set, almost global asymptotic stability is given.

Recent work of Calloni [27] and Zanchettin [28] use methods of robust design for magnetic actuated spacecrafts. Calloni developed a robust controller using linear time-periodic models and linear parameter-varying models, whereas Zanchettin proposed a H_∞ controller design also using linear time-periodic models.

The work of Wood et al. [29] uses model predictive control to stabilize the magnetic actuated spacecraft. They also use a linear approximation of the satellite dynamics and achieve improved performance compared to PD control. Stability is proven with and without terminal costs in the design and Floquet analysis.

Lizaralde and Wen [30] pursued another approach, assuming no angular velocity measurement is provided. They suggest a nonlinear filter for the quaternion to extract the velocity information. This filter is designed utilizing the passivity of the system. Since they do not assume magnetic actuation and therefore have a fully actuated system, they are able to show global asymptotic stability.

Due to limited project budget, *CubeSat Pegasus* is built using commercial off-the-shelf

microprocessors instead of special aerospace hardware. Therefore, regular software crashes and reboots are expected due to solar radiation. Because of this drawback a control law is chosen that does not depend on information from the past and can be computed in short time rather than e. g. model predictive control. Because of this issue and having almost global stability, the PD control law presented in the work of Lovera and Astolfi [26] is used in this work.

Due to rather high angular velocities after tip-off, a simple control law without need of attitude information is used to detumble the satellite. This control law follows the work presented in [31] and is adapted to perform in a time-optimal manner.

Sensors for a direct measurement of the spacecraft's orientation (e. g. star trackers) are complex and expensive. Therefore, estimating the attitude using simpler vector measurements was and is an ongoing research area.

The survey article of Crassidis and Markley [32] gives insight into the different estimation methods. In practice, two main ideas for estimating the attitude using vector measurements can be pointed out. First, the well known Extended Kalman Filter (EKF) [33] and second, the static quaternion estimator (QUEST) [34, 35]. In [36], these two approaches are compared in detail, using measurements of the magnetic field and the Sun vector. Generally, the EKF shows better performance and the ability to estimate additional slowly varying parameters like the gyroscope bias. On the contrary, the QUEST has advantages concerning computational effort and power consumption.

In this work, an Extended Kalman Filter design is applied, following [37]. The choice for a dynamic estimation method emerges from the better performance under the presence of noise and the ability to give an estimation of the measurement errors.

The task of attitude control of nanosatellites is rarely solved using magnetic actuation only and having only simple measurements to determine the attitude. The proposed strategy of handling the lack of measurements while achieving the required performance represents a cheap and new solution for this task.

1.3 Outline of the thesis

The thesis is structured as follows: In Chapter 2, a detailed mathematical model for the satellite together with the actuator design and sensor models will be given. The environmental models are investigated and an evaluation of disturbance torques is given. The basic concepts of orbital dynamics are explained and the *QB50* orbit is calculated. Chapter 3 covers the main algorithms and methods used for attitude estimation and control. Arguments supporting the choice of the strategy are given for each algorithm and the stability of the control laws is proven.

The resulting statements are verified considering the *QB50* requirements via simulations. The implementation of the algorithms and simulation results are given in Chapter 4.

A summary and outlook chapter with suggestions of improvements and ideas for future work completes the thesis.

In Appendix A, some basic quaternion mathematics are given for a better comprehension of the calculations in Chapter 2 and Chapter 3.

2 Modeling

In this chapter, the required mathematical models are derived. First the attitude kinematics and dynamics of a rigid body are described. In Section 2.2, a general introduction to the Keplerian elements and orbital dynamics is given and applied to a desired orbit. The spacecraft's environment in terms of the Earth's magnetic field, the Sun position and environmental disturbances is described in Section 2.3. In the last section of this chapter, the *CubeSat Pegasus* sensor and actuator hardware is investigated and the used models are given.

Throughout this work, four Cartesian coordinate systems are used (cf. [38], [39]). The Earth Centered Inertial (ECI) frame denoted by the subscript I , the Earth Centered Earth Fixed (ECEF) frame F , the orbital frame O and the body fixed frame B . These reference frames are shown in Figure 2.1.

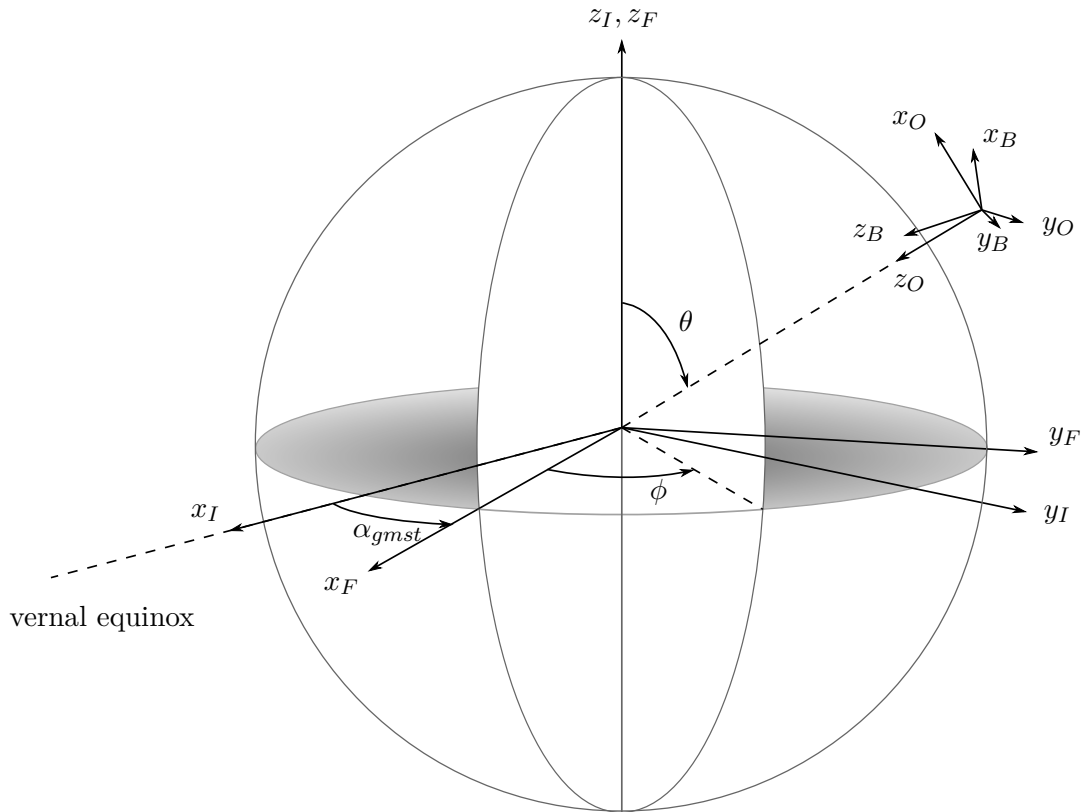


Figure 2.1: Definition of the used reference frames.

The ECI frame has its origin in the Earth's center. The x_I -axis is pointing towards the

vernal equinox direction¹, the z_I -axis coincides with the Earth's rotational axis, pointing northwards and the y_I -axis completes the right-handed Cartesian coordinate system. This frame is assumed to be without rotation or translation and represents an inertial reference frame.

Related to the ECI reference frame the ECEF frame is defined. The origin and the z_F -axis of this frame coincide with the origin and the z_I -axis of the ECI frame, but the x_F -axis of the ECEF frame is pointing from the Earth's center to the prime meridian (Greenwich, UK). The y_F -axis completes the right-handed triad.

A transformation between the ECI and ECEF reference frame is a rotation around the common z_I -axis, about the Greenwich Mean Sidereal Time (gmst). The Greenwich Mean Sidereal Time is defined as the angle of the vernal equinox at the prime meridian at Greenwich, UK. This angle between the x_I -axis and the x_F -axis expressed in the inertial frame is denoted by α_{gmst} in Figure 2.1.

The orbital frame has its origin in the satellite's center of gravity. The x_O -axis is pointing into the desired flight direction, i. e. tangential to the orbit, the z_O -axis is pointing towards the Earth's center. In the spacecraft context, this z_O -direction is referred to as Nadir. The y_O -axis is perpendicular to the orbital plane and completes the right-handed triad. The origin of the body frame is located in the center of gravity of the satellite. The x_B -axis points to the anterior quadratic surface, the z_B -axis points to the rectangular surface which is meant to face the Earth and the y_B -axis completes the right-handed triad. The body frame is visualized in Figure 2.2.

¹The vernal equinox is the intersection of the Earth's equatorial plane with the plane of the Earth's orbit around the Sun, in the direction of the Sun's position relative to the Earth on the first day of spring (cf. [31]).

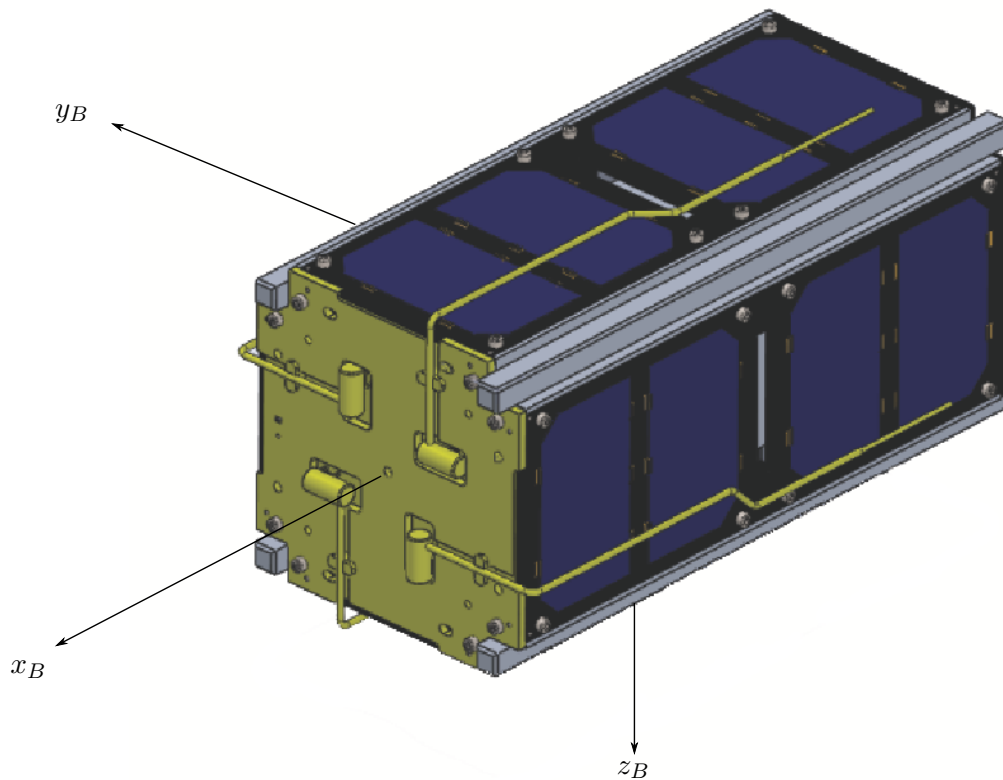


Figure 2.2: The defined body reference frame of *CubeSat Pegasus*.

2.1 Satellite model

The quaternion representation of the attitude is chosen to avoid singularities. Quaternions constitute the minimal representation free from singularities. Furthermore, they have advantages concerning computational effort especially when it comes to re-normalization which is a crucial point for this work, e. g. in the attitude estimation. A comprehensive introduction to the theory behind quaternion algebra is given in [40] and [41], the most important basics are summarized in Appendix A of this work.

2.1.1 Quaternion kinematics

The kinematics of different attitude representations, including the quaternion representation is described in [31]. Every rotation or sequence of rotations can be described by a rotation axis \mathbf{e} and a rotation angle ϑ about this axis, often combined to the axis-angle

vector $\boldsymbol{\vartheta} = \vartheta \mathbf{e}$. With these definitions, the rotation quaternion² is defined as

$$\mathbf{q}(\mathbf{e}, \vartheta) = \begin{bmatrix} q_0 \\ q_1 \\ q_2 \\ q_3 \end{bmatrix} = \begin{bmatrix} \cos \frac{\vartheta}{2} \\ \mathbf{e} \sin \frac{\vartheta}{2} \end{bmatrix} \quad (2.1a)$$

$$\vartheta \mathbf{e} = \boldsymbol{\vartheta}, \quad (2.1b)$$

with $\|\mathbf{e}\| = 1$. The definition of the quaternion (2.1) satisfies the constraint $\|\mathbf{q}\| = 1$ and hence represents a unit quaternion. Rotation quaternions are free of singularities but not unique, since a three-dimensional operation is represented by a four-dimensional quantity. The quaternion $\mathbf{q}(\mathbf{e}, \vartheta)$ describes the same rotation as $\mathbf{q}(-\mathbf{e}, -\vartheta)$.

Defining the quaternion product \otimes as described in (A.3) allows to calculate sequences of rotations in the same order as it is done using rotation matrices (cf. [42]).

With the time derivative of the rotation quaternion, defined as

$$\frac{d\mathbf{q}(t)}{dt} = \lim_{\Delta t \rightarrow 0} \frac{\mathbf{q}(t + \Delta t) - \mathbf{q}(t)}{\Delta t} \quad (2.2)$$

the quaternion kinematic is derived.

The rotation described by $\mathbf{q}(t + \Delta t)$ is rewritten in a sequential representation using the matrix exponential $\exp(\cdot)$ defined in (A.7), giving

$$\mathbf{q}(t + \Delta t) = \Delta \mathbf{q}(\Delta t) \otimes \mathbf{q}(t) = [\Delta \mathbf{q}(\Delta t) \otimes] \mathbf{q}(t) = \exp\left(\left[\begin{bmatrix} 0 \\ \frac{\Delta \boldsymbol{\vartheta}}{2} \end{bmatrix} \otimes\right]\right) \mathbf{q}(t), \quad (2.3a)$$

where $[\otimes]$ is the matrix representation of the quaternion product as defined in (A.3b).

A linear Taylor approximation of the matrix exponential leads to

$$\mathbf{q}(t + \Delta t) \approx \mathbf{q}(t) + \left[\begin{bmatrix} 0 \\ \frac{\Delta \boldsymbol{\vartheta}}{2} \end{bmatrix} \otimes\right] \mathbf{q}(t). \quad (2.3b)$$

Inserting (2.3b) into (2.2) yields

$$\frac{d\mathbf{q}(t)}{dt} = \lim_{\Delta t \rightarrow 0} \frac{\left[\begin{bmatrix} 0 \\ \frac{\Delta \boldsymbol{\vartheta}}{2} \end{bmatrix} \otimes\right] \mathbf{q}(t) + \cancel{\mathbf{q}(t)} - \cancel{\mathbf{q}(t)}}{\Delta t}. \quad (2.3c)$$

Defining the angular velocity $\boldsymbol{\omega}$ as

$$\boldsymbol{\omega}(t) = \lim_{\Delta t \rightarrow 0} \frac{\Delta \boldsymbol{\vartheta}}{\Delta t}, \quad (2.4)$$

and since the quaternion multiplication $[\otimes]$ is associative (cf. [40]), the limit of (2.2) follows as

$$\frac{d\mathbf{q}(t)}{dt} = \lim_{\Delta t \rightarrow 0} \frac{1}{2} \left[\begin{bmatrix} 0 \\ \frac{\Delta \boldsymbol{\vartheta}}{\Delta t} \end{bmatrix} \otimes\right] \mathbf{q}(t) = \frac{1}{2} \left[\begin{bmatrix} 0 \\ \boldsymbol{\omega}(t) \end{bmatrix} \otimes\right] \mathbf{q}(t). \quad (2.5)$$

²Quaternions in general are four-dimensional vectors together with the definition of the quaternion multiplication. In this work, quaternions are solely used as unit quaternions to represent rotations.

Finally, the compact formulation

$$\dot{\mathbf{q}}(t) = \frac{1}{2} \left[\begin{array}{c} 0 \\ \boldsymbol{\omega}(t) \end{array} \right] \otimes \mathbf{q}(t) , \quad (2.6)$$

where $\dot{x} = \frac{dx}{dt}$ holds, describes the evolution of the quaternion with time, the quaternion kinematics.

2.1.2 Body dynamics

Euler's second law of rigid body motion defines the dynamic relation between external torques and change of angular momentum with time and takes the form

$$\frac{d\mathbf{l}_I}{dt} = \boldsymbol{\tau}_I \quad (2.7a)$$

$$\mathbf{l}_I = \mathbf{J}_I \boldsymbol{\omega}_{BI}^I , \quad (2.7b)$$

where \mathbf{l}_I is the angular momentum expressed in some inertial frame, $\boldsymbol{\tau}_I$ is the sum of torques acting on the rigid body, \mathbf{J}_I is the body's moment of inertia about the body's center of mass and $\boldsymbol{\omega}_{BI}^I$ the body's angular velocity expressed in the inertial reference frame. Performing the time derivative of (2.7b) results in

$$\boldsymbol{\tau}_I = \frac{d}{dt} \left(\mathbf{J}_I \boldsymbol{\omega}_{BI}^I \right) = \dot{\mathbf{J}}_I \boldsymbol{\omega}_{BI}^I + \mathbf{J}_I \dot{\boldsymbol{\omega}}_{BI}^I . \quad (2.8)$$

To express the quantities in the body frame, the following relations are used

$$\mathbf{J}_I = \mathbf{R}_{BI}^T \mathbf{J}_B \mathbf{R}_{BI} \quad (2.9a)$$

$$\boldsymbol{\omega}_{BI}^I = \mathbf{R}_{BI}^T \boldsymbol{\omega}_{BI}^B = \mathbf{R}_{BI}^T \boldsymbol{\omega}_{BI} \quad (2.9b)$$

$$\boldsymbol{\tau}_I = \mathbf{R}_{BI}^T \boldsymbol{\tau}_B , \quad (2.9c)$$

where \mathbf{J}_B is constant for a rigid body and represents the body's moment of inertia about the center of mass, expressed in the body frame. As introduced in the nomenclature, $\boldsymbol{\omega}_{BI}^B$ is written in the simplified notation $\boldsymbol{\omega}_{BI}$ and the rotation matrix \mathbf{R}_{BI} in (2.9) represents the rotational transformation from the inertial frame I to the body frame B .

The derivatives $\dot{\mathbf{J}}_I$ and $\dot{\boldsymbol{\omega}}_{BI}^I$ follow with (2.9) to

$$\dot{\mathbf{J}}_I = \dot{\mathbf{R}}_{BI}^T \mathbf{J}_B \mathbf{R}_{BI} + \mathbf{R}_{BI}^T \mathbf{J}_B \dot{\mathbf{R}}_{BI} \quad (2.10a)$$

$$\dot{\boldsymbol{\omega}}_{BI}^I = \dot{\mathbf{R}}_{BI}^T \boldsymbol{\omega}_{BI} + \mathbf{R}_{BI}^T \dot{\boldsymbol{\omega}}_{BI} . \quad (2.10b)$$

Using (2.9) and the properties

$$\dot{\mathbf{R}}_{BI} \mathbf{R}_{BI}^T = - [\boldsymbol{\omega}_{BI} \times] \quad (2.11a)$$

$$[\boldsymbol{\omega}_{BI} \times] \boldsymbol{\omega}_{BI} = \mathbf{0} , \quad (2.11b)$$

where $[\times]$ is the matrix representation of the cross product and substituting (2.10) into (2.8) gives

$$\boldsymbol{\tau}_B = [\boldsymbol{\omega}_{BI} \times] \mathbf{J}_B \boldsymbol{\omega}_{BI} + \mathbf{J}_B \dot{\boldsymbol{\omega}}_{BI} . \quad (2.12)$$

Reformulating terms of (2.12) yields the dynamics of a rigid body

$$\dot{\boldsymbol{\omega}}_{BI} = \mathbf{J}_B^{-1} (\boldsymbol{\tau}_B - [\boldsymbol{\omega}_{BI} \times] \mathbf{J}_B \boldsymbol{\omega}_{BI}) , \quad (2.13a)$$

also known as Euler's rotation equations.

The external torques $\boldsymbol{\tau}_B$ can be defined as the sum of intended control torques $\boldsymbol{\tau}_{B,c}$ and unintended disturbance torques $\boldsymbol{\tau}_{B,d}$. The dynamic model (2.13a) with the distinct torques reads as

$$\dot{\boldsymbol{\omega}}_{BI} = \mathbf{J}_B^{-1} (\boldsymbol{\tau}_{B,c} + \boldsymbol{\tau}_{B,d} - [\boldsymbol{\omega}_{BI} \times] \mathbf{J}_B \boldsymbol{\omega}_{BI}) . \quad (2.13b)$$

Using the attitude kinematics in the global quaternion formulation (2.6) together with the dynamics of a rigid body (2.13b) forms a 7-dimensional set of differential equations describing the rotational motion of a rigid body. Defining the 7-dimensional state vector

$\mathbf{x} = \begin{bmatrix} \mathbf{q}_{BI} \\ \boldsymbol{\omega}_{BI} \end{bmatrix}$ gives the combined dynamic system of (2.6) and (2.13b)

$$\dot{\mathbf{x}} = \mathbf{f}(\mathbf{x}) = \begin{bmatrix} \frac{1}{2} \left[\begin{bmatrix} 0 \\ \boldsymbol{\omega}_{BI} \end{bmatrix} \otimes \mathbf{q}_{BI} \right] \\ \mathbf{J}_B^{-1} (\boldsymbol{\tau}_{B,c} + \boldsymbol{\tau}_{B,d} - [\boldsymbol{\omega}_{BI} \times] \mathbf{J}_B \boldsymbol{\omega}_{BI}) \end{bmatrix} . \quad (2.14)$$

2.2 Orbital dynamics

Johannes Kepler's laws of planetary motion (cf. [38]), stating

1. The orbit of each planet is an ellipse, with the Sun at one focus.
2. The line joining the planet and the Sun sweeps out equal areas in equal times.
3. The square of the period of a planet is proportional to the cube of its mean distance from the Sun.

can be used to describe the motion of satellites orbiting the Earth. The common parameterization of a planetary respectively satellite orbit is given by the six classical Keplerian orbital elements:

a'	semimajor axis	i	inclination
e	eccentricity	Ω	right ascension of the ascending node
ν_0	mean anomaly	ω	argument of perigee

The difference between the mean and true anomaly is presented in Figure 2.3. The ellipse in Figure 2.3 represents the actual orbit of the spacecraft while the circle serves as an imaginary circular orbit. The true anomaly ν is defined as the angle between the perigee of the elliptical orbit and the position vector of the spacecraft. The mean anomaly ν_0 is the angular of an imaginary body moving in the circular orbit with the same orbital period as the actual body in the elliptical orbit. A visualization of the Keplerian elements is given in Figure 2.4.

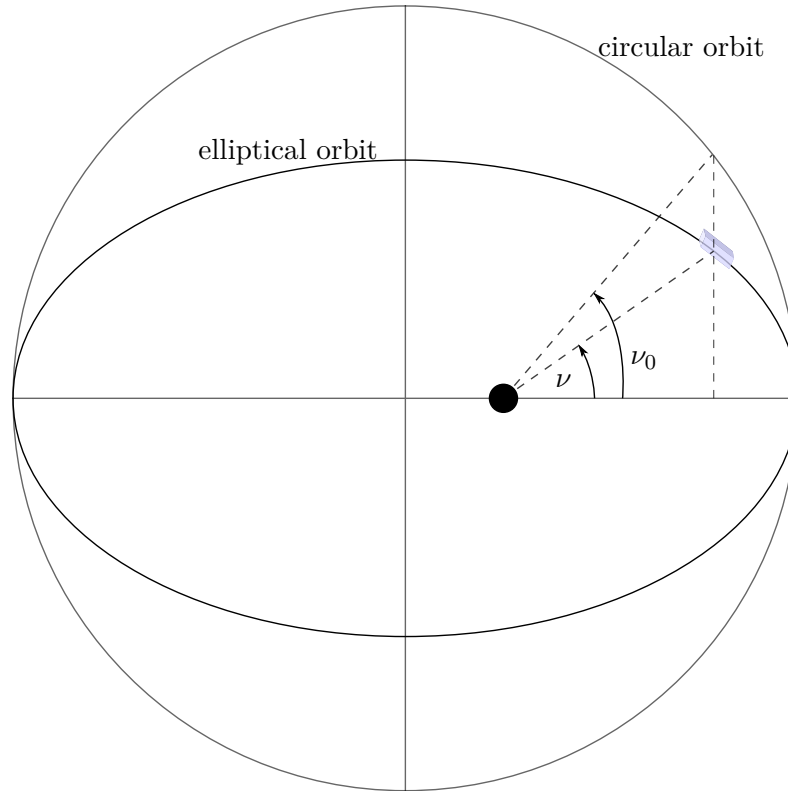


Figure 2.3: About the difference between the true and mean anomaly.

The six Keplerian elements are combined to the parameter vector

$$\mathbf{k}^T = [a' \quad e \quad \nu_0 \quad i \quad \Omega \quad \omega] .$$

For given Keplerian elements \mathbf{k} , the position of the satellite in inertial coordinates can be expressed using a series of rotational matrices as shown in Figure 2.4 (cf. [42]). By predicting the orbital elements over time using Kepler's Equations, a predicted attitude is described. In this way, a time-series of the desired attitude (trajectory) is calculated (cf. [31]).

2.2.1 Orbit of the QB50 mission

The orbit for the *QB50* mission is planned to be a Sun-synchronous circular orbit with an altitude of 450km, eccentricity $e < 0.05$, and inclination $i \approx 98^\circ$. A Sun-synchronous orbit is defined to have a fixed angle between the orbital plane and the direction of the Sun as shown in Figure 2.5.

For the prediction of the orbit, the very small eccentricity, which has only little impact, is neglected to reduce computational effort. This simplification results in a circular orbit with radius r_O instead of an ellipse. The mean anomaly ν_0 and the true anomaly ν are equal for a circular orbit, the argument of perigee ω is arbitrary for a circular orbit. Thus, the argument of perigee ω is set to zero.

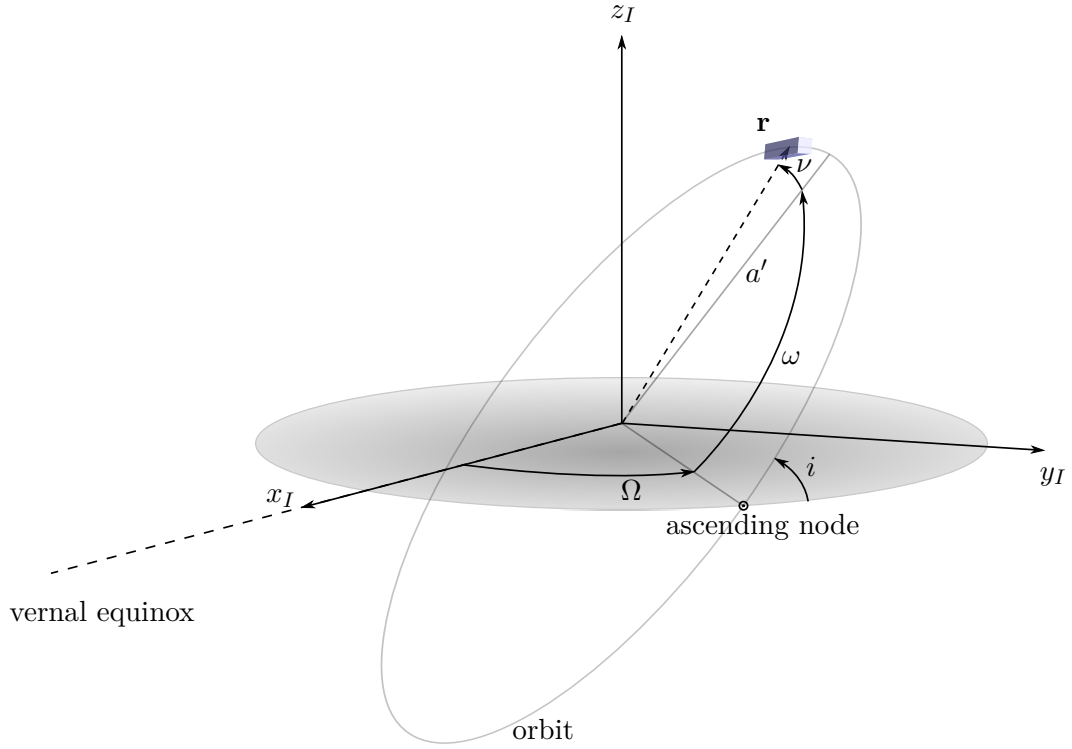


Figure 2.4: Visualization of the defined orbital elements.

Due to the rather thin atmosphere in the orbit's altitude, a constant velocity of the spacecraft is assumed for the time of predicting the orbital elements.

By applying these simplifications the time dependent desired Keplerian elements $\bar{\mathbf{k}}(t) = [r_O \ 0 \ \nu(t) \ i \ \Omega(t) \ 0]$ are defined, where r_O and i are constant parameters and the time dependent angles are calculated as

$$\nu(t) = \nu_0 + \frac{2\pi t}{T_O} \quad (2.15a)$$

$$\Omega(t) = \Omega_0 + \frac{2\pi t}{T_{trop}}, \quad (2.15b)$$

with the orbital period T_O and the period of a tropical year T_{trop} . According to [38] the orbital period is calculated as

$$T_O = 2\pi \sqrt{\frac{r_O}{\mu}}, \quad (2.16)$$

where r_O is the orbital radius (Earth's radius r_E + satellite's altitude a) and μ is the Earth's gravitational parameter $\mu = GM$ with the gravitational constant G and the Earth's mass M .

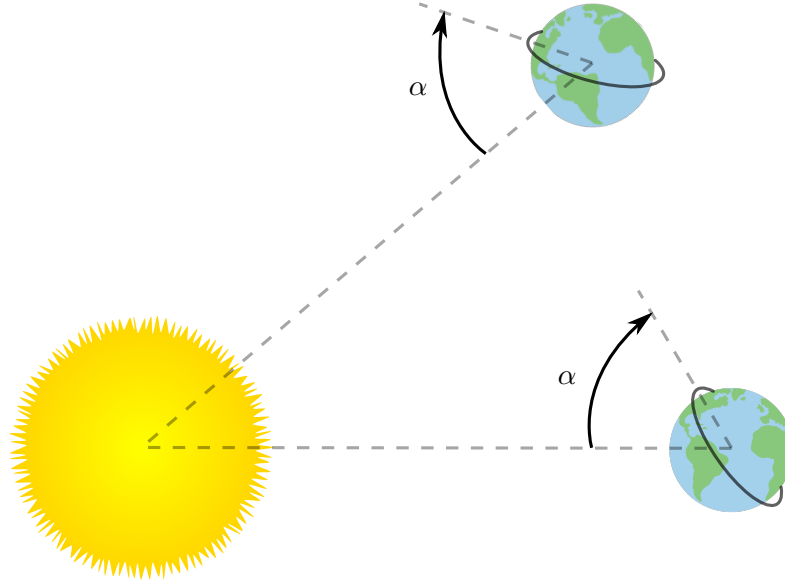


Figure 2.5: The definition of a Sun-synchronous orbit $\alpha = \text{const.}$ (not to scale).

A tropical year is the time period in which the Earth encircles the Sun once, respectively the time between two vernal equinoxes.

The constant parameters a , i and Ω_0 define the size and initial position of the circular orbit with respect to the ECI frame. The initial anomaly ν_0 defines the initial position of the satellite on the orbit. The time dependent variable $\nu(t)$ likewise represents the position of the satellite on the orbit at the time t . The time dependency of the right ascension $\Omega(t)$ is used to achieve Sun-synchronization. In Figure 2.6, the initial *QB50* orbit is shown.

The rotation matrix $\mathbf{R}_{OI}(t)$ as a function of time, representing the desired attitude of the satellite, follows as

$$\mathbf{R}_{OI}(t) = \left(\mathbf{R}_{z,\Omega(t)} \mathbf{R}_{x,i} \mathbf{R}_{z,\nu(t)} \mathbf{R}_B \right)^T, \quad (2.17a)$$

with the notation of basic rotations as introduced. The additional rotation matrix \mathbf{R}_B is used to align the orbital frame with the chosen body frame and is given as

$$\mathbf{R}_B = \begin{bmatrix} 0 & 0 & -1 \\ 1 & 0 & 0 \\ 0 & -1 & 0 \end{bmatrix}. \quad (2.17b)$$

The skew-symmetric matrix of the desired angular velocity of the satellite $\boldsymbol{\omega}_{OI}$ is obtained by taking the time derivative of (2.17a), i. e.

$$[\boldsymbol{\omega}_{OI \times}] = -\dot{\mathbf{R}}_{OI} \mathbf{R}_{OI}^T. \quad (2.17c)$$

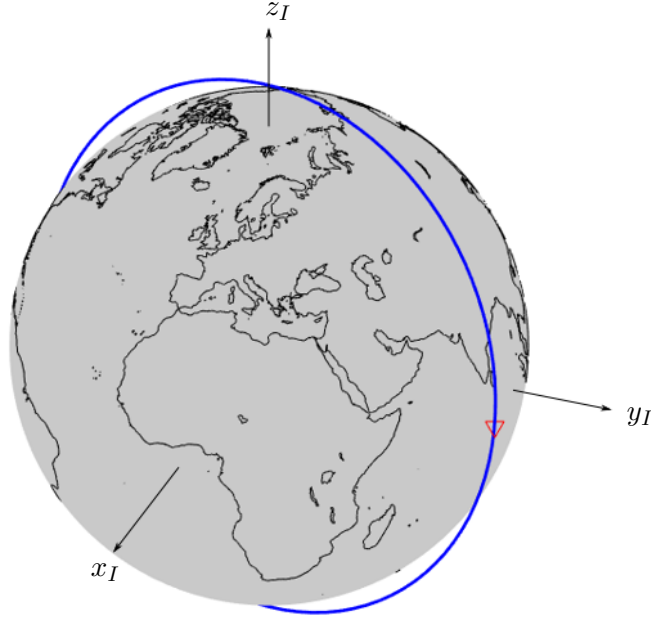


Figure 2.6: *QB50* orbit, expressed in the inertial coordinate system. The red triangle denotes the satellite's initial position and flight direction.

With the quaternion representation \mathbf{q}_{OI} (\mathbf{R}_{OI}) of the rotation matrix and the angular velocity $\boldsymbol{\omega}_{OI}$ the desired trajectory of the system is calculated as

$$\mathbf{x}_{OI} = \begin{bmatrix} \mathbf{q}_{OI} \\ \boldsymbol{\omega}_{OI} \end{bmatrix}. \quad (2.18)$$

The aim of the control system is to align the states \mathbf{x} of the dynamic system (2.14) with the desired trajectory \mathbf{x}_{OI} and to stabilize the system along the trajectory.

2.3 Environment model

The attitude can be determined using at least two vector measurements and two appropriate reference vectors as long as they are not parallel. For this purpose, mathematical models of the Earth's magnetic field and the Sun's position are derived.

Known disturbance torques acting on the satellite are discussed and mathematical models of the disturbances are given.

2.3.1 Earth's magnetic field

Utilizing the Earth's magnetic field for control and estimation has many advantages. Magnetic actuators - called magnetorquers - are free of moving parts, cheap and robust.

Magnetic field sensors - Magnetometers - are inexpensive as well, easy to implement and if realized redundantly good accuracy is achieved. In order to reach high accuracy in estimating the attitude, a detailed model of the Earth's magnetic field is crucial. In this work, the widely used and accepted International Geomagnetic Reference Field (IGRF) model is used. The IGRF model is a spherical harmonic model of the magnetic scalar potential of a given point in space $\Psi(r_O, \theta, \phi)$ expressed in the ECEF reference frame, where r_O represents the distance and (θ, ϕ) are the geocentric coordinates of the point as shown in Figure 2.1. The IGRF-model is updated regularly by means of parameter identification of various measurements (cf. [43]). The magnetic field $\bar{\mathbf{b}}_F(r_O, \theta, \phi)$ follows as the negative gradient of the magnetic scalar potential

$$\bar{\mathbf{b}}_F(r_O, \theta, \phi) = -\nabla\Psi(r_O, \theta, \phi) , \quad (2.19a)$$

with $(\nabla f)(\mathbf{x}) = \left(\frac{\partial f}{\partial \mathbf{x}}\right)^T$ (cf. [44]).

The model of the magnetic scalar potential Ψ used in the IGRF model is given as

$$\Psi(r_O, \theta, \phi) = r_E \sum_{n=1}^k \left(\frac{r_E}{r_O}\right)^{n+1} \sum_{m=0}^n (g_n^m \cos(m\phi) + h_n^m \sin(m\phi)) P_n^m(\theta) , \quad (2.19b)$$

with r_E being the Earth's radius, r_O the radius of the orbit (Earth's radius r_E + satellite's altitude a), θ the geocentric co-latitude³ and ϕ the geocentric longitude (cf. Figure 2.1). The scalar k defines the order of the model, the current IGRF-model⁴ uses the scalar potential (2.19b) with an order of $k = 13$. The coefficients g_n^m , h_n^m are Gaussian coefficients and the scalar functions $P_n^m(\theta)$ are the Schmidt quasi-normalized associated Legendre functions (cf. [31, 43]).

To calculate the geocentric coordinates θ and ϕ , the satellite's position is expressed in the ECI reference frame using the Keplerian elements of the orbit. With the Greenwich Mean Sideral Time the position is expressed in the ECEF frame. The geocentric coordinates θ , ϕ are calculated using a coordinate transformation (cf. [31]). With the geocentric coordinates the magnetic field $\bar{\mathbf{b}}_F(r_O, \theta, \phi)$, expressed in the ECEF frame, is calculated and rotated back to the inertial frame again using the Greenwich Mean Sideral Time, i. e.

$$\bar{\mathbf{b}}_I(r_O, \theta, \phi) = \mathbf{R}_{z, \alpha_{gms}} \bar{\mathbf{b}}_F(r_O, \theta, \phi) . \quad (2.19c)$$

2.3.2 Position of the Sun

The light beams radiated by the Sun are assumed to appear parallel for the whole orbit from the satellite's point of view, which is reasonable thanks to the long distance in between the Sun and the Earth and the low altitude of the satellite. Therefore, the position of the Sun can be modeled as a single vector pointing from the Sun to the Earth's center, denoted as the Sun vector \mathbf{s} in this work. To express this vector in the inertial reference frame, the period of a tropical year T_{trop} is needed. The Sun vector follows as

³90° minus geocentric latitude

⁴version 12, December 2014

$$\bar{\mathbf{s}}_I(t) = \begin{bmatrix} \cos\left(\frac{2\pi(t-t_0)}{T_{trop}}\right) \\ \cos(\epsilon_O) \sin\left(\frac{2\pi(t-t_0)}{T_{trop}}\right) \\ \sin(\epsilon_O) \sin\left(\frac{2\pi(t-t_0)}{T_{trop}}\right) \end{bmatrix}, \quad (2.20)$$

where ϵ_O is the axial tilt between the Earth's rotational axis and the rotational axis of the Earth's orbit around the Sun, denoted as obliquity. For this work, the obliquity is treated as a constant with $\epsilon_O = 23.5^\circ$ (cf. [39]).

In Figure 2.7, the obliquity and the visualization of a tropical year is shown. The initial time t_0 is the instant of time when the Sun vector equals the vernal equinox direction.

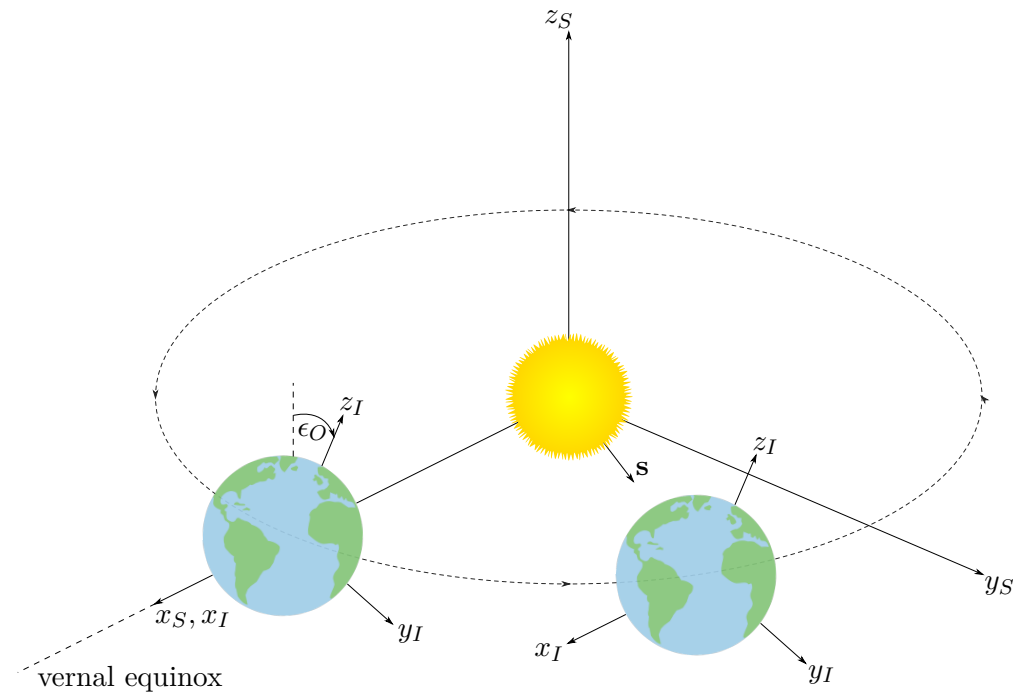


Figure 2.7: Visualization of the Earth orbiting the Sun (not to scale).

2.3.3 Disturbance torques

To describe the satellite's environment in detail, the expected disturbances acting on a satellite in low altitudes are investigated. At low altitudes there is still a considerable amount of the Earth's atmosphere left, which has two effects.

First, thanks to the atmosphere the solar wind is small enough to be neglected. Secondly, the aerodynamic torque is definitely a source of errors if not taken into account (cf. [31]). Another known external torque is the so called gravity gradient torque τ_{gg} arising from the decaying gravitational field and uneven mass distribution (cf. [38]).

Gravity gradient torque

The gravity gradient can be used as a passive stabilization (cf. [24]), e.g. for so called tethered satellites or satellites with an attached gravity gradient boom. The reason of gravity gradient forces is the reduction of the gravitational forces by the square of the distance to the Earth's center.

Designing the satellite in a way that one axis has a relatively high moment of inertia compared to the others makes the gravity gradient effect usable. Parts of the satellite which are closer to the Earth's center are gravitated stronger than parts further away. As a result of the gravity gradient stabilization the satellite will tend to align the axis with the maximum moment of inertia vertically.

In the case of a nanosatellite, characterized by small dimensions and even mass distribution favored, the gravity gradient torque is treated as an undesired disturbance torque.

Following the arguments in [31], thinking of a particle of mass m_i at the position \mathbf{r}_i with respect to the Earth's center of mass, the gravitational force acting on this particle calculates as

$$\mathbf{f}_{i,g} = m_i \mathbf{g}(\mathbf{r}_i) , \quad (2.21)$$

where $\mathbf{g}(\mathbf{r})$ is the local gravitational field at the position \mathbf{r} . For the gravitational field $\mathbf{g}(\mathbf{r})$ the assumption of a spherically symmetric vector field

$$\mathbf{g}(\mathbf{r}) = -\frac{\mu \mathbf{r}}{\|\mathbf{r}\|^3} \quad (2.22)$$

is used, where μ is the gravitational parameter calculated as $\mu = GM$ with the gravitational constant G and the mass of the gravitating body M , in this case the Earth's mass. Taking into account only variations of (2.22) up to the second order and summing up the associated torques around the satellite's center of mass the model of the gravity gradient torque results in (cf. [31])

$$\boldsymbol{\tau}_{gg} = 3 \frac{\mu}{r_O^3} (\mathbf{n}_B \times (\mathbf{J}_B \mathbf{n}_B)) \quad (2.23a)$$

$$\text{with } \mathbf{n}_B = \mathbf{R}_{BO} \begin{bmatrix} 0 \\ 0 \\ 1 \end{bmatrix} . \quad (2.23b)$$

The Nadir unit vector \mathbf{n}_B is pointing towards the center of the gravitating body, expressed in the body frame. As before, r_O denotes the orbit's radius and \mathbf{J}_B represents the satellite's inertia matrix, expressed in the body frame.

Aerodynamic torque

To derive a model of the aerodynamic torques acting on the satellite, the aerodynamic normal forces onto each face of the satellite are calculated (cf. [31]). Summing up the resulting torques around the satellite's center of gravity gives the total aerodynamic torque. Due to the high velocity of the satellite in a Low Earth Orbit, the velocity of the

atmosphere itself can be neglected and the airflow is assumed acting straight from the direction of flight with the speed of the satellite \mathbf{v}_B . With A_i the area of the i -th face and the angle between the surface normal and the wind direction $\theta_{a,i}$ the aerodynamic normal force acting on this face follows as

$$\mathbf{f}_{ad,i} = -\frac{1}{2}\rho C_d \|\mathbf{v}_B\| \mathbf{v}_B A_i \max(\cos(\theta_{a,i}), 0) , \quad (2.24)$$

where C_d is the aerodynamic drag coefficient and ρ the atmospheric density.

The term $\max(\cos(\theta_{a,i}), 0)$ is needed because only surfaces that face the wind directly are taken into account, flow effects are neglected.

The add-up torque $\boldsymbol{\tau}_{ad}$, generated from the forces acting on each surface of the satellite, is then given by

$$\boldsymbol{\tau}_{ad} = \sum_{i=1}^6 \mathbf{r}_{B,i} \times \mathbf{f}_{ad,i} \quad (2.25)$$

with $\mathbf{r}_{B,i}$ being the vector pointing from the satellites center of gravity to the geometric center of the i th surface.

2.4 Actuators and sensors

In the last section of this chapter, the actuators and sensors of the *CubeSat Pegasus* are presented.

CubeSat Pegasus is equipped with a set of five magnetic actuators, so called magnetorquers, giving the ability to generate any three-dimensional dipole moment \mathbf{m} . The magnetorquers are mounted on each rectangular surface ($y, -y, z, -z$) and on the anterior quadratic surface (x), the rear quadratic surface has no magnetorquer. As stated, magnetorquers have advantages in price and robustness but are also source of a general control problem, namely underactuation. The applicable torque $\boldsymbol{\tau}_B$ arises from the interaction between the local Earth's magnetic field \mathbf{b}_B and the generated dipole moment \mathbf{m}_B . Thus, it is constrained to the plane perpendicular to the magnetic field \mathbf{b}_B . The calculation of the resulting torques

$$\boldsymbol{\tau}_B = \mathbf{m}_B \times \mathbf{b}_B , \quad (2.26)$$

with \times being the cross product, illustrates this fact.

The considered sensing hardware contains a 3-axis magnetometer, a 3-axis gyroscope and solar sensors on each surface of the satellite. Using two independent vector measurements (magnetic field $\tilde{\mathbf{b}}_B$ and Sun vector $\tilde{\mathbf{s}}_B$) gives the general ability to estimate the satellite's attitude. The gyroscope information gives the further ability to derive dynamic filters rather than using static methods.

The first section focuses on a general design approach for magnetorquers using static optimization and in the second section, some widely used models for the different sensors are presented.

2.4.1 Magnetorquer design

For the given geometry of a rectangular magnetorquer shown in Figure 2.8, an approach for an optimal design is derived. The magnetorquer consists of a thin copper coil manufactured directly on a printed circuit board without any ferromagnetic core. Since the height of the coil compared to the overall dimensions is very small, the dipole moment of the solenoid is given as (cf. [45])

$$\mathbf{m} = nA_{avg}i\mathbf{e}_m, \quad (2.27)$$

where n is the number of turns, A_{avg} is the average area covered by the coil, and i is the current through the coil. The direction \mathbf{e}_m of the magnetic dipole moment follows from the right hand grip rule. The optimal values for the number of turns n and the width of

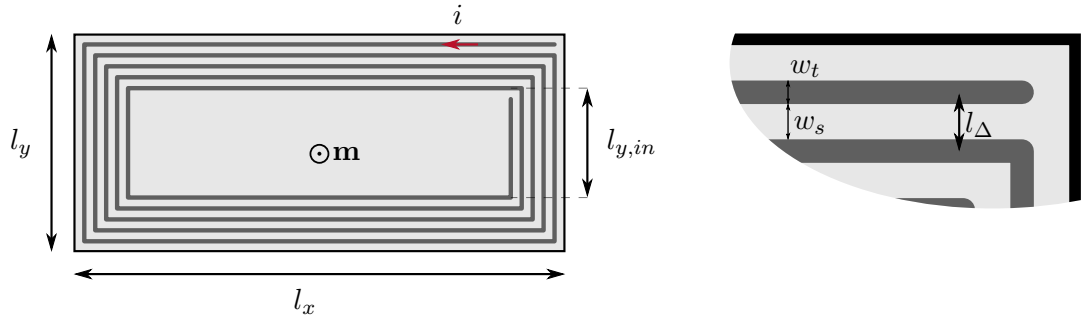


Figure 2.8: Definition of the magnetorquer dimensions.

the trace w_t are asked in order to maximize the absolute value of the dipole moment \mathbf{m} . The dimensions l_x , l_y , the constant supply voltage U_s , and the thickness of the circuit board h_t are known and given.

A higher number of turns n increases the total resistance R_t of the trace and therefore decreases the maximum current i , but also increases the absolute value of the dipole moment \mathbf{m} . On the other hand, a wider trace w_t decreases the total resistance R_t and therefore increases the maximum current i , but limits the number of turns n due to limited space on the circuit board.

The width of the trace w_t and the space in between two traces w_s are added up to $l_\Delta = w_t + w_s$ with w_s being constant.

In order to find the optimal values (n^*, w_t^*) in terms of the maximal magnetic dipole moment, a static optimization problem is formulated. First a formula for the total length of a trace l_t is needed to calculate the total resistance R_t .

By systematically reducing the dimensions by l_Δ with each turn, a series formulation is found by

$$l_t = \underbrace{2l_x + l_y + (l_y - l_\Delta)}_{2(l_x+l_y)-l_\Delta} + \sum_{j=1}^{n-1} \underbrace{(l_x - (2j-1)l_\Delta) + (l_y - 2jl_\Delta) + (l_x - 2jl_\Delta) + (l_y - (2j+1)l_\Delta)}_{2(l_x+l_y)-8jl_\Delta} \quad (2.28a)$$

and simplified using Gauss summation formula

$$l_t = 2n(l_x + l_y) - (4n(n - 1) + 1)(w_t + w_s) , \quad (2.28b)$$

where $l_\Delta = w_t + w_s$ is substituted. With the electrical resistivity of copper ρ_{Cu} and the dimensions of the copper trace the total electrical resistance follows as

$$R_t = \rho_{Cu} \frac{l_t}{w_t h_t} , \quad (2.29)$$

where h_t is the height of the trace.

For the given supply voltage U_s and (2.29), the current through the coil is calculated as (cf. [46])

$$i = \frac{U_s}{R_t} . \quad (2.30)$$

Using the arithmetic mean in the form

$$\begin{aligned} A_{avg} &= (l_x l_y + (l_x - 2l_\Delta)(l_y - 2l_\Delta) + \dots) \frac{1}{n} \\ &= l_x l_y + \frac{1}{6}(2n^2 + 3n + 1)(w_t + w_s) - \frac{1}{2}(l_x + l_y)(n + 1)(w_t + w_s) , \end{aligned} \quad (2.31)$$

the average area covered by the rectangular coil is calculated.

Substituting (2.28b) into (2.29) and (2.30) and using the averaged area given by (2.31) leads to the formulation of the magnetic dipole moment with n and w_t as degrees of freedom, given by

$$\mathbf{m}(n, w_t) = n A_{avg} i \mathbf{e}_m . \quad (2.32)$$

The magnetic dipole moment \mathbf{m} together with the surrounding magnetic field \mathbf{b} is generating a torque $\boldsymbol{\tau} = \mathbf{m} \times \mathbf{b}$. To achieve maximum control torque, thus best control performance, an optimization problem with constraints

$$(n^*, w_t^*) = \arg \max_{(n, w_t)} m(n, w_t) \quad (2.33a)$$

$$\text{s.t. } 0 \leq i_{max} - i(n, w_t) \quad (2.33b)$$

$$0 \leq (l_y - l_{y,in}) - 2nl_\Delta \quad (2.33c)$$

is formulated where the Euclidean norm $m(n, w_t) = \|\mathbf{m}(n, w_t)\|$ of the dipole moment $\mathbf{m}(n, w_t)$ is maximized.

The constraint $0 \leq i(n, w_t) - i_{max}$ guarantees that the current through the coil $i(n, w_t) = \frac{U_s}{R_t(n, w_t)}$ is limited to the maximum current i_{max} . The second constraint $0 \leq (l_y - l_{y,in}) - 2nl_\Delta$ ensures that the coil's area is limited. Choosing $l_{y,in} = 0$ limits the area of the coil to the overall dimensions of the circuit board (l_x, l_y) .

2.4.2 Sensor models

Considering that the measurements are subject to various measurement errors, e. g. bias, nonlinearity, scaling etc. (cf. [38, 47]), appropriate sensor models are important.

The measurements of the local magnetic field and the Sun vector are assumed to be corrupted by additive, zero-mean Gaussian white noise. As generally known, gyroscope measurements usually suffer from a slowly varying, additional bias with large amplitudes arising, e. g., from temperature variations (cf. [48]). Denoting η_x as the additive Gaussian white noise of the measured variable \tilde{x} where x is the true value, the sensor models of the three vector measurements follow as

$$\tilde{\mathbf{b}}_B = \mathbf{b}_B + \boldsymbol{\eta}_b \quad (2.34)$$

$$\tilde{\mathbf{s}}_B = \mathbf{s}_B + \boldsymbol{\eta}_s \quad (2.35)$$

$$\tilde{\boldsymbol{\omega}}_{BI} = \boldsymbol{\omega}_{BI} + \boldsymbol{\beta} + \boldsymbol{\eta}_\omega, \quad (2.36)$$

with the gyroscope bias $\boldsymbol{\beta}$.

The Sun vector \mathbf{s} is calculated using the measurements of the six photo diodes equipped on each face of the satellite.

The measured intensity I of one photo diode is proportional to the cosine of the angle between the light beam and the photo diode's surface normal vector. According to [31], the Sun vector \mathbf{s} is calculated as

$$\mathbf{s} = \frac{1}{I_{max}} \begin{bmatrix} I_x - I_{-x} \\ I_y - I_{-y} \\ I_z - I_{-z} \end{bmatrix} \quad (2.37)$$

where I_x denotes the intensity measured by the photo diode which is mounted on the front surface of the satellite, the positive x_B -direction. The other intensities are denoted likewise and I_{max} is the maximum intensity, used to normalize \mathbf{s} .

The light reflected from the Earth and the Moon, known as Albedo, is less intense than the light coming direct from the Sun (cf. [49]). By taking into account only the maximum intensity of each direction (x_B, y_B, z_B), disturbances arising from reflections are reduced. Using this method, (2.37) follows as

$$\mathbf{s} = \frac{1}{I_{max}} \begin{bmatrix} s_x \\ s_y \\ s_z \end{bmatrix} \quad (2.38)$$

with $s_j = \begin{cases} I_j, & I_j \geq I_{-j} \\ -I_{-j}, & I_j < I_{-j} \end{cases}$ for $j \in \{x, y, z\}$.

2.5 Chapter conclusion

In this section, the mathematical models of the satellite were presented. The derived model of the satellite dynamics is of general nature and can be used for various types of rigid bodies where the attitude is of interest. The orbital dynamics with the assumption of

a perfect circular orbit constitutes a thoughtful compromise between the error in the result and the computational effort. The presented environmental models are widely accepted and used throughout the literature. The considered disturbance torques are known as the main disturbance torques in low altitudes. The framework for an optimal design of the magnetic actuators gave early impact on the design of the *CubeSat Pegasus* and is believed to be used in future projects as well. The presented sensor models are standard formulations taken from the literature, meaningful choices of the noise powers and bias range are important to support their validity.

3 Attitude determination and control system

In this chapter, an attitude determination and control system (ADCS) for the investigated class of satellites is derived based on the models of Chapter 2. High angular velocities and arbitrary orientation after detaching from the launch vehicle, limited computing capacity, and limitations in the sensing hardware justify the chosen strategy.

At tip-off from the launch vehicle, the satellite can have rather high angular velocities. Therefore, a detumbling controller is used to reduce the angular velocities and to stabilize the satellite at a random attitude. Once the angular velocities are small enough and the estimation error falls below a certain limit, a PD controller is used to stabilize the desired attitude (2.18). The whole procedure, starting at tip-off, is displayed in the flowchart in Figure 3.1.

The considered spacecraft uses magnetic actuators for control. As stated, the realizable control torque generated by the magnetorquers is restricted to the plane perpendicular to the local magnetic field. Therefore, the desired control torque \mathbf{u} is projected onto the plane perpendicular to the local magnetic field \mathbf{b} .

The projection is done in order to remove ineffective components of the control torque and save electric power. The effective torque generated by the magnetorquers is restricted by nature. With the projection, the minimal magnetic dipole moment \mathbf{m} and subsequently the minimal control current \mathbf{i} to generate the desired control action is obtained.

The control torque, applied to the satellite, follows as (cf. [31])

$$\boldsymbol{\tau}_{B,c} = \left(\mathbf{I}_3 - \mathbf{e}_{\tilde{\mathbf{b}}_B} \mathbf{e}_{\tilde{\mathbf{b}}_B}^T \right) \mathbf{u} , \quad (3.1)$$

where $\mathbf{e}_{\tilde{\mathbf{b}}_B}$ is the unit vector of the measured local magnetic field and \mathbf{I}_3 the identity matrix of dimension three. The matrix $\mathbf{e}_{\tilde{\mathbf{b}}_B} \mathbf{e}_{\tilde{\mathbf{b}}_B}^T$ represents a projection onto the direction of the measured magnetic field $\tilde{\mathbf{b}}$. Taking in mind that the true local magnetic field \mathbf{b}_B is unknown the measured value $\tilde{\mathbf{b}}_B$ is used. Substituting the control torque (3.1) into the dynamic model of the satellite (2.13b) and not taking disturbance torques into account yields

$$\mathbf{J}_B \dot{\boldsymbol{\omega}}_{BI} = - [\boldsymbol{\omega}_{BI} \times] \mathbf{J}_B \boldsymbol{\omega}_{BI} + \left(\mathbf{I}_3 - \mathbf{e}_{\tilde{\mathbf{b}}_B} \mathbf{e}_{\tilde{\mathbf{b}}_B}^T \right) \mathbf{u} . \quad (3.2)$$

The input matrix $(\mathbf{I}_3 - \mathbf{e}_{\tilde{\mathbf{b}}_B} \mathbf{e}_{\tilde{\mathbf{b}}_B}^T)$ is denoted by $\boldsymbol{\Gamma}(t)$ with the explicit mention of the time variance arising from the time varying magnetic field $\tilde{\mathbf{b}}_B(t)$. The matrix $\boldsymbol{\Gamma}(t)$ is positive semi-definite for all times t , denoted by $\boldsymbol{\Gamma}(t) \geq \mathbf{0}$, with eigenvalues $(1, 1, 0)$ at every instance of time (cf. [26]). This loss of rank of the input matrix shows the described underactuation in a mathematical representation.

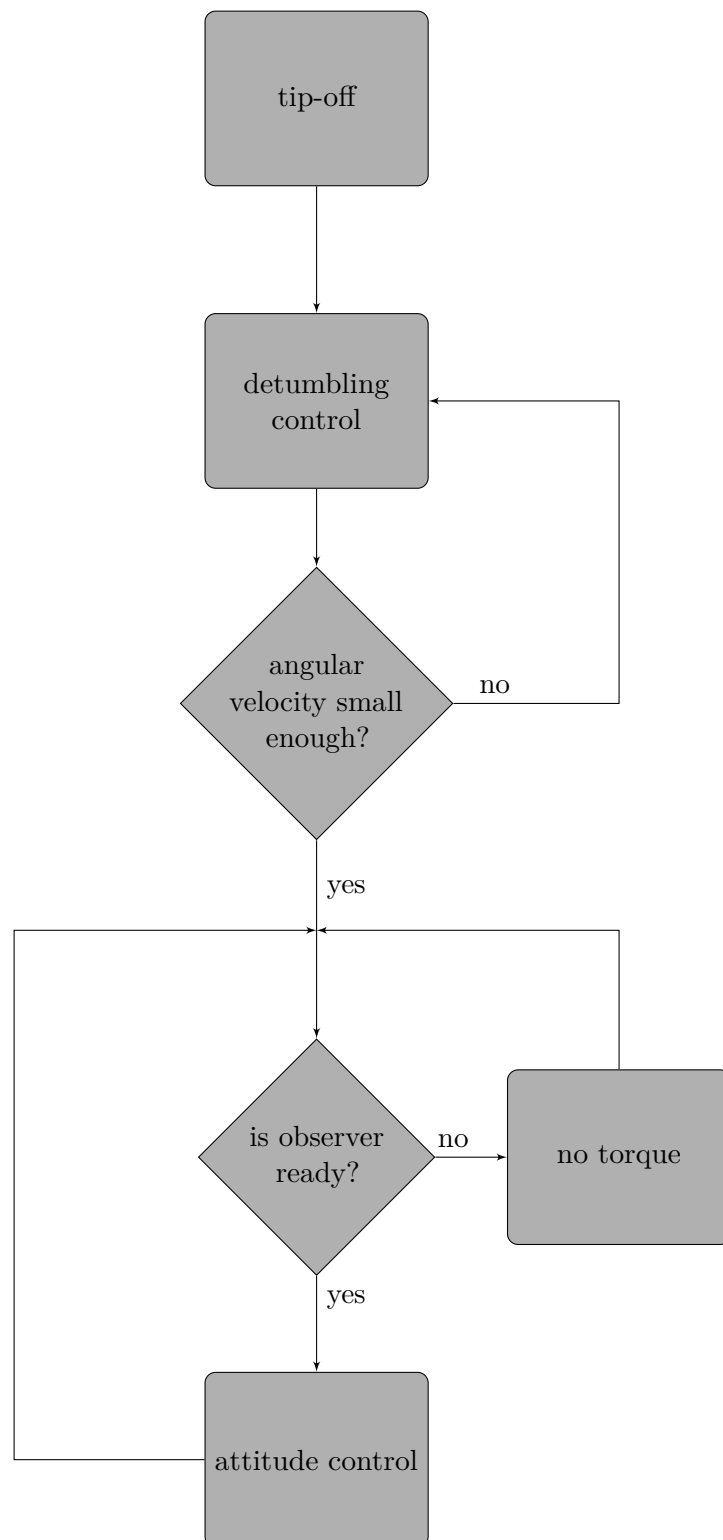


Figure 3.1: Flowchart of the proposed control strategy.

3.1 Detumbling control

The first task for the ADCS is slowing down the satellite from the high tip-off rates after detaching from the launch vehicle. Utilizing the gyroscope measurement $\tilde{\omega}_{BI}$ allows to formulate the control law (cf. [50])

$$\mathbf{u} = -k_{\mathbf{b}}\tilde{\omega}_{BI} , \quad (3.3)$$

where $k_{\mathbf{b}}$ is a positive scalar.

The effective control torque $\tau_{B,c}$ from (3.1) for the detumbling control law (3.3) follows as

$$\tau_{B,c} = -k_{\mathbf{b}} \left(\mathbf{I}_3 - \mathbf{e}_{\tilde{\mathbf{b}}_B} \mathbf{e}_{\tilde{\mathbf{b}}_B}^T \right) \tilde{\omega}_{BI} . \quad (3.4)$$

The intention of the control law (3.4) is to null the measured angular velocities $\tilde{\omega}_{BI}$. This procedure is referred to as detumbling control in this context.

The block diagram of the detumbling controller in closed-loop, as it is used in the simulation, is presented in Figure 3.2. The initial parameters t_0 and \mathbf{k}_0 are used to predict the IGRF reference magnetic field $\bar{\mathbf{b}}_I$ as described in Section 2.3.1. The sensor models add the Gaussian noises $\boldsymbol{\eta}$ and the bias $\boldsymbol{\beta}$ to the reference values according to Section 2.4.2 and transforms the quantities to the body frame using the satellite's attitude \mathbf{q}_{BI} . The model of the satellite's dynamics is affected by the disturbance torques $\tau_{gg}, \tau_{ad}, \tau_{\eta}$, where τ_{gg} is the gravity gradient torque and τ_{ad} is the aerodynamic torque derived in Section 2.3.3. The additional disturbance torque τ_{η} is assumed to be Gaussian white noise, representing neglected sources of error.

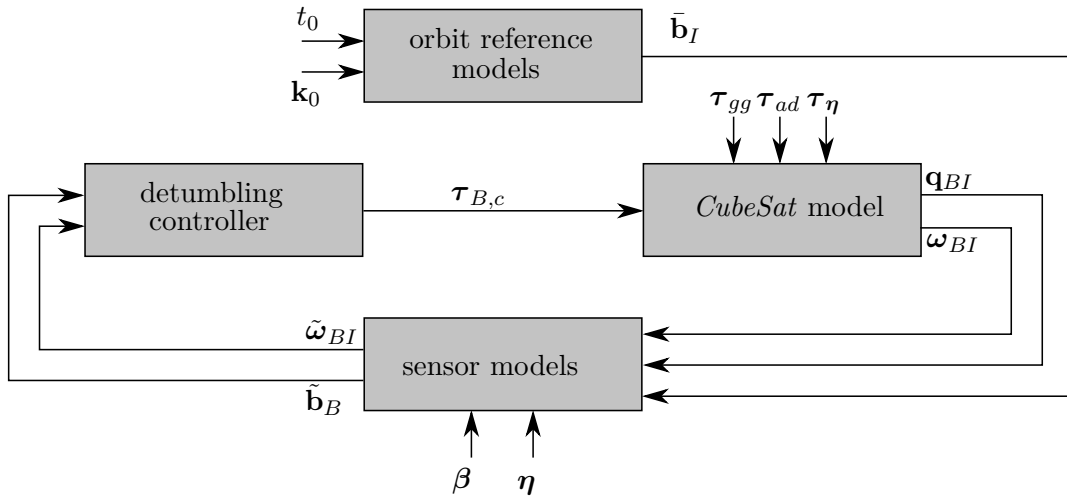


Figure 3.2: Block diagram of the detumbling controller in closed-loop, as used in the simulation.

The scalar $k_{\mathbf{b}}$ of (3.4) is chosen in a way to achieve a bang-bang characteristic and ensure time-optimal detumbling. The maximum control torque is not a constant value, but depending on the local magnetic field. To calculate the required gain $k_{\mathbf{b}}$ for maximum

torque, a detour via the maximum current is used. The required current as a function of the control torque is calculated as

$$\mathbf{i}_{B,c} = \mathbf{S}^{-1} \frac{\tilde{\mathbf{b}}_B \times \boldsymbol{\tau}_{B,c}}{\|\tilde{\mathbf{b}}_B\|} = -\mathbf{S}^{-1} \frac{\tilde{\mathbf{b}}_B \times \boldsymbol{\Gamma}(t) \tilde{\boldsymbol{\omega}}_{BI}}{\|\tilde{\mathbf{b}}_B\|} \quad (3.5)$$

where $\mathbf{S} = \text{diag}(n_j A_{avg,j})$, $j \in \{x, y, -y, z, -z\}$ is a constant scaling matrix containing the factors $n_j A_{avg,j}$ from (2.27) for each magnetorquer. The optimal gain factor is then calculated as

$$k_{\mathbf{b}}^* = \frac{|i_{max}|}{\max(|i_{B,c,j}|)}, \quad j \in \{x, y, -y, z, -z\}, \quad (3.6)$$

with the superscript $*$ denoting the optimality.

Proof of stability

To prove the stability of the control law (3.4), the kinetic energy of the system

$$V(\boldsymbol{\omega}_{BI}) = \frac{1}{2} \boldsymbol{\omega}_{BI}^T \mathbf{J}_B \boldsymbol{\omega}_{BI} \quad (3.7)$$

is used as a Lyapunov function. Following Lyapunov's direct method, the time derivative of (3.7) with (3.2) and (3.3) results in

$$\dot{V}(\boldsymbol{\omega}_{BI}) = \boldsymbol{\omega}_{BI}^T \mathbf{J}_B \dot{\boldsymbol{\omega}}_{BI} = -\boldsymbol{\omega}_{BI}^T ([\boldsymbol{\omega}_{BI} \times] (\mathbf{J}_B \boldsymbol{\omega}_{BI}) + k_{\mathbf{b}} (\mathbf{I}_3 - \mathbf{e}_{\tilde{\mathbf{b}}_B} \mathbf{e}_{\tilde{\mathbf{b}}_B}^T)) \boldsymbol{\omega}_{BI}. \quad (3.8a)$$

With the help of the triple product

$$\boldsymbol{\omega}_{BI}^T (\boldsymbol{\omega}_{BI} \times (\mathbf{J}_B \boldsymbol{\omega}_{BI})) = (\mathbf{J}_B \boldsymbol{\omega}_{BI})^T \underbrace{(\boldsymbol{\omega}_{BI} \times \boldsymbol{\omega}_{BI})}_{=0}, \quad (3.8b)$$

a compact solution is given by

$$\dot{V}(\boldsymbol{\omega}_{BI}) = -k_{\mathbf{b}} \boldsymbol{\omega}_{BI}^T (\mathbf{I}_3 - \mathbf{e}_{\tilde{\mathbf{b}}_B} \mathbf{e}_{\tilde{\mathbf{b}}_B}^T) \boldsymbol{\omega}_{BI} \leq 0, \quad (3.8c)$$

where the matrix $\boldsymbol{\Gamma}(t) = (\mathbf{I}_3 - \mathbf{e}_{\tilde{\mathbf{b}}_B} \mathbf{e}_{\tilde{\mathbf{b}}_B}^T)$ is positive semi-definite. Therefore, $\dot{V}(\boldsymbol{\omega}_{BI}) \leq 0$ holds for $k_{\mathbf{b}} > 0$ which proves the stability of the equilibrium $\tilde{\boldsymbol{\omega}}_{BI} = \mathbf{0}$. Only in the particular case where the measured magnetic field and the vector of the angular velocities are parallel, no control torque can be generated

$$\boldsymbol{\omega}_{BI} \parallel \tilde{\mathbf{b}}_B \Rightarrow \boldsymbol{\tau}_{B,c} = \mathbf{0}, \dot{V} = 0. \quad (3.9)$$

Although theoretically problematic, this detail can be disregarded in practical use because of the variation of the magnetic field along the orbit (cf. [50] and [51]).

3.2 Extended Kalman Filter

By measuring two independent vectorial values, e. g., the Earth's magnetic field and the Sun vector the attitude can be determined (cf. [52]). Static approaches like the quaternion estimator (QUEST) just use the measurement information to calculate the attitude and therefore, suffer from high noise or bad dynamic behavior. To minimize the noise an Extended Kalman Filter based on the quaternion kinematics is used to estimate the attitude.

Using an EKF, it is easy to extend the design to estimate various additional quantities (cf. [36]). In this section, an EKF design is derived with the purpose of estimating the satellite's attitude \mathbf{q}_{BI} and the gyroscope bias $\boldsymbol{\beta}$ introduced in Section 2.4.2.

Throughout this section the states \mathbf{q}_{BI} , $\boldsymbol{\omega}_{BI}$ are solely expressed in the body reference frame and describe the attitude respectively angular velocity of the inertial reference frame with respect to the body reference frame. The subscripts $_{BI}$ are dropped due to better readability. The superscripts $^-$ and $^+$ used in the description of the EKF algorithm are used to distinguish between a priori ($^-$) and a posteriori information ($^+$).

Estimator model for the attitude

The quaternion, which is the minimal attitude representation free from singularities, is the choice for most EKF designs (cf. [32]). As discussed in detail in [37], there are two widely used formulations for attitude filtering using quaternions - the additive and multiplicative representation. In this work, the multiplicative representation

$$\mathbf{q} = \delta\mathbf{q}(\delta\boldsymbol{\vartheta}) \otimes \hat{\mathbf{q}}, \quad (3.10)$$

introduced in [53] is used. The idea is to express the true attitude \mathbf{q} as the product of an error quaternion $\delta\mathbf{q}$ and the estimated attitude $\hat{\mathbf{q}}$. Stating that the error quaternion respectively the related axis-angle vector $\delta\boldsymbol{\vartheta}$ is small enough, it is possible to use the four-dimensional quaternion $\hat{\mathbf{q}}$ as the global estimator variable and the three-dimensional axis-angle vector $\delta\hat{\boldsymbol{\vartheta}}$ as a local representation. This approach reduces the dimension of the EKF design by one and therefore decreases computational effort.

Taking the time derivative of (3.10) yields

$$\dot{\mathbf{q}} = \delta\dot{\mathbf{q}} \otimes \hat{\mathbf{q}} + \delta\mathbf{q} \otimes \dot{\hat{\mathbf{q}}}, \quad (3.11)$$

where the true attitude \mathbf{q} and the estimated attitude $\hat{\mathbf{q}}$ both satisfy the attitude dynamics (2.6) given by

$$\dot{\mathbf{q}} = \frac{1}{2} \left[\begin{array}{c} 0 \\ \boldsymbol{\omega} \end{array} \right] \otimes \mathbf{q} \quad (3.12a)$$

$$\dot{\hat{\mathbf{q}}} = \frac{1}{2} \left[\begin{array}{c} 0 \\ \hat{\boldsymbol{\omega}} \end{array} \right] \otimes \hat{\mathbf{q}}. \quad (3.12b)$$

Substituting (3.12) and (3.10) into (3.11) gives

$$\frac{1}{2} \left[\begin{array}{c} 0 \\ \boldsymbol{\omega} \end{array} \right] \otimes \delta\mathbf{q} \otimes \hat{\mathbf{q}} = \delta\dot{\mathbf{q}} \otimes \hat{\mathbf{q}} + \frac{1}{2} \delta\mathbf{q} \otimes \left[\begin{array}{c} 0 \\ \hat{\boldsymbol{\omega}} \end{array} \right] \otimes \hat{\mathbf{q}} \quad (3.13)$$

and resorting terms results in

$$\delta\dot{\mathbf{q}} = \frac{1}{2} \begin{bmatrix} 0 \\ \boldsymbol{\omega} \end{bmatrix} \otimes \delta\mathbf{q} - \frac{1}{2} \delta\mathbf{q} \begin{bmatrix} 0 \\ \hat{\boldsymbol{\omega}} \end{bmatrix} \otimes . \quad (3.14a)$$

Defining the true angular velocity as the sum of the estimated angular velocity $\hat{\boldsymbol{\omega}}$ and some estimation error $\delta\boldsymbol{\omega}$

$$\boldsymbol{\omega} = \hat{\boldsymbol{\omega}} + \delta\boldsymbol{\omega} , \quad (3.14b)$$

results in

$$\delta\dot{\mathbf{q}} = \underbrace{\frac{1}{2} \begin{bmatrix} 0 \\ \hat{\boldsymbol{\omega}} \end{bmatrix} \otimes \delta\mathbf{q} - \frac{1}{2} \delta\mathbf{q} \otimes \begin{bmatrix} 0 \\ \hat{\boldsymbol{\omega}} \end{bmatrix}}_{\begin{bmatrix} 0 \\ \delta\mathbf{q}_{1:3} \times \hat{\boldsymbol{\omega}} \end{bmatrix}} + \frac{1}{2} \begin{bmatrix} 0 \\ \delta\boldsymbol{\omega} \end{bmatrix} \otimes \delta\mathbf{q} \quad . \quad (3.14c)$$

$(\delta\mathbf{q} - \mathbf{q}_I + \mathbf{q}_I)$

Adding the term $-\mathbf{q}_I + \mathbf{q}_I$, with the unit quaternion $\mathbf{q}_I = [1 \ 0 \ 0 \ 0]^T$, to the last multiplicand leaves the result unchanged but since $\begin{bmatrix} 0 \\ \delta\boldsymbol{\omega} \end{bmatrix}$ and $(\delta\mathbf{q} - \mathbf{q}_I)$ are both small, their product can be neglected concerning the linearization of the Extended Kalman Filter. The linear approximation of (3.14a) is therefore given by

$$\delta\dot{\mathbf{q}} \approx \begin{bmatrix} 0 \\ \delta\mathbf{q}_{1:3} \times \hat{\boldsymbol{\omega}} \end{bmatrix} + \frac{1}{2} \begin{bmatrix} 0 \\ \delta\boldsymbol{\omega} \end{bmatrix} . \quad (3.15)$$

Using the small angle approximation of the quaternion as defined in (A.8)

$$\delta\mathbf{q} \approx \begin{bmatrix} 1 \\ \frac{\delta\boldsymbol{\vartheta}}{2} \end{bmatrix} , \quad \delta\mathbf{q}_{1:3} \approx \frac{1}{2} \delta\boldsymbol{\vartheta} , \quad (3.16)$$

allows the dynamic model for the local error angles $\delta\boldsymbol{\vartheta}$ to be formulated as

$$\delta\dot{\boldsymbol{\vartheta}} = \delta\boldsymbol{\vartheta} \times \hat{\boldsymbol{\omega}} + \delta\boldsymbol{\omega} . \quad (3.17)$$

Estimator model for the gyroscope bias

Gyroscopes suffer from high bias, varying with temperature and over time. Since attitude estimation is sensitive to an offset in the measured angular velocity, the state of the Extended Kalman Filter is extended by an additive bias introduced in (2.36). In view of (3.14b), the estimation of the gyroscope bias $\boldsymbol{\beta}$ is defined as

$$\boldsymbol{\beta} = \hat{\boldsymbol{\beta}} + \delta\boldsymbol{\beta} . \quad (3.18)$$

The dynamics of the true bias $\boldsymbol{\beta}$ is given by

$$\dot{\boldsymbol{\beta}} = \boldsymbol{\eta}_\beta \quad (3.19)$$

with the Gaussian white noise $\boldsymbol{\eta}_\beta$. The estimated bias $\hat{\boldsymbol{\beta}}$ is defined as a constant vector without dynamics, therefore

$$\delta\dot{\boldsymbol{\beta}} = \boldsymbol{\eta}_\beta \quad (3.20)$$

describes the dynamics of the estimation error.

Gyroscope model

With the definition of the gyroscope model from Section 2.4.2 and since the additive noise $\boldsymbol{\eta}_\omega$ is naturally unknown, the true and estimated angular velocity follow as

$$\boldsymbol{\omega} = \tilde{\boldsymbol{\omega}} - \boldsymbol{\beta} - \boldsymbol{\eta}_\omega \quad (3.21a)$$

$$\hat{\boldsymbol{\omega}} = \tilde{\boldsymbol{\omega}} - \hat{\boldsymbol{\beta}}. \quad (3.21b)$$

The estimation error $\delta\boldsymbol{\omega} = \boldsymbol{\omega} - \hat{\boldsymbol{\omega}}$ is therefore calculated as

$$\delta\boldsymbol{\omega} = \underbrace{\hat{\boldsymbol{\beta}} - \boldsymbol{\beta}}_{\delta\boldsymbol{\beta}} - \boldsymbol{\eta}_\omega. \quad (3.22)$$

Substituting (3.22) into (3.17) leads to the final observer model for the attitude error

$$\delta\dot{\boldsymbol{\vartheta}} = \delta\boldsymbol{\vartheta} \times \hat{\boldsymbol{\omega}} + \delta\boldsymbol{\beta} - \boldsymbol{\eta}_\omega. \quad (3.23)$$

Dynamical model of observed variables

Defining the observer state vector as $\boldsymbol{\chi}^\text{T} = [\delta\boldsymbol{\vartheta}^\text{T} \quad \delta\boldsymbol{\beta}^\text{T}]$ and the vector of disturbances as $\mathbf{w}^\text{T} = [\boldsymbol{\eta}_\omega^\text{T} \quad \boldsymbol{\eta}_\beta^\text{T}]$ allows the observer model to be defined as the time-variant linear dynamic system

$$\dot{\boldsymbol{\chi}} = \mathbf{f}(\boldsymbol{\chi}, t) = \begin{bmatrix} -\hat{\boldsymbol{\omega}}(t) \times \delta\boldsymbol{\vartheta} + \delta\boldsymbol{\beta} - \boldsymbol{\eta}_\omega \\ \boldsymbol{\eta}_\beta \end{bmatrix} = \underbrace{\begin{bmatrix} [-\hat{\boldsymbol{\omega}}(t) \times] & \mathbf{I}_3 \\ \mathbf{0}_3 & \mathbf{0}_3 \end{bmatrix}}_{\mathbf{A}(t)} \boldsymbol{\chi} + \underbrace{\begin{bmatrix} -\mathbf{I}_3 & \mathbf{0}_3 \\ \mathbf{0}_3 & \mathbf{I}_3 \end{bmatrix}}_{\mathbf{B}} \mathbf{w}. \quad (3.24)$$

In order to digitally implement the EKF, the time-continuous system (3.24) is transformed to the discrete formulation (e. g. [31])

$$\boldsymbol{\chi}_{k+1} = \boldsymbol{\Phi}_k \boldsymbol{\chi}_k + \boldsymbol{\Lambda}_k \mathbf{w}_k, \quad (3.25)$$

where $\boldsymbol{\Phi}_k$ and $\boldsymbol{\Lambda}_k$ are calculated using the matrix exponential (cf. [54]) and $\boldsymbol{\chi}_k = \boldsymbol{\chi}(kT_s)$ with the sampling time T_s .

Measurement and measurement sensitivity

According to the chosen sensor models defined in Section 2.4.2, the time-discrete measurement function is defined as

$$\mathbf{y}_k = \mathbf{h}_k(\mathbf{q}_k) + \boldsymbol{\eta}_k = \begin{bmatrix} \mathbf{R}(\mathbf{q}_k) \mathbf{b}_{I,k} \\ \mathbf{R}(\mathbf{q}_k) \mathbf{s}_{I,k} \end{bmatrix} + \begin{bmatrix} \boldsymbol{\eta}_{\mathbf{b},k} \\ \boldsymbol{\eta}_{\mathbf{s},k} \end{bmatrix} = \begin{bmatrix} \mathbf{b}_{B,k} \\ \mathbf{s}_{B,k} \end{bmatrix} + \begin{bmatrix} \boldsymbol{\eta}_{\mathbf{b},k} \\ \boldsymbol{\eta}_{\mathbf{s},k} \end{bmatrix} = \begin{bmatrix} \tilde{\mathbf{b}}_{B,k} \\ \tilde{\mathbf{s}}_{B,k} \end{bmatrix}, \quad (3.26)$$

with the true attitude \mathbf{q} and the true values of the magnetic field \mathbf{b} and the Sun vector \mathbf{s} . The matrix $\mathbf{R}(\mathbf{q})$ is the rotation matrix representation of the quaternion \mathbf{q} as defined in (A.5) and transforms the vector \mathbf{b}_I into the body reference frame \mathbf{b}_B .

Defining a general estimation error as the difference between some measured value and some a priori estimation $\zeta = y(\chi) - h(\hat{\chi}^-)$, the full estimation error follows as

$$\zeta_{\mathbf{h},k} = \mathbf{y}_k - \mathbf{h}_k(\hat{\chi}_k^-) . \quad (3.27)$$

The measurement sensitivity matrix is given by

$$\mathbf{H}_k(\chi_k) = \frac{\partial \mathbf{h}_k}{\partial \chi_k} = \begin{bmatrix} \frac{\partial \mathbf{h}_k}{\partial (\delta \vartheta_k)} & \frac{\partial \mathbf{h}_k}{\partial (\delta \beta_k)} \end{bmatrix} . \quad (3.28)$$

The derivative of $\frac{\partial \mathbf{h}}{\partial (\delta \vartheta)}$ is presented for a single vector measurement for simplicity. The simplified measurement function

$$\mathbf{h}^\dagger(\mathbf{q}) = \mathbf{R}(\mathbf{q}) \bar{\mathbf{v}}_I , \quad \bar{\mathbf{v}} \in \{\bar{\mathbf{b}}, \bar{\mathbf{s}}\} , \quad (3.29a)$$

where the reference value $\bar{\mathbf{v}}_I$ is used instead of the unknown true value \mathbf{v}_I represents (3.26) for a single vector measurement. Using the multiplicative quaternion representation (3.10) leads to

$$\mathbf{h}^\dagger(\mathbf{q}) = \mathbf{R}(\delta \mathbf{q}) \mathbf{R}(\hat{\mathbf{q}}) \bar{\mathbf{v}}_I . \quad (3.29b)$$

With the rotation matrix formulation (A.5) and the small angle approximation (A.8) $\mathbf{R}(\delta \mathbf{q})$ is approximated as

$$\mathbf{R}(\delta \mathbf{q}) \approx \mathbf{I}_3 - [\delta \vartheta \times] . \quad (3.29c)$$

This approximation means a linearization, which is characteristic for an EKF design.

Therefore, the linear approximation of (3.29a) is given by

$$\mathbf{h}^\dagger(\mathbf{q}) \approx \mathbf{R}(\hat{\mathbf{q}}) \bar{\mathbf{v}}_I - [\delta \vartheta \times] \mathbf{R}(\hat{\mathbf{q}}) \bar{\mathbf{v}}_I = \mathbf{R}(\hat{\mathbf{q}}) \bar{\mathbf{v}}_I + [\mathbf{R}(\hat{\mathbf{q}}) \bar{\mathbf{v}}_I \times] \delta \vartheta . \quad (3.29d)$$

From (3.29d) the measurement sensitivity $\frac{\partial \mathbf{h}^\dagger}{\partial (\delta \vartheta)}$ follows as

$$\frac{\partial \mathbf{h}^\dagger}{\partial (\delta \vartheta)} = [\mathbf{R}(\hat{\mathbf{q}}) \bar{\mathbf{v}}_I \times] . \quad (3.30a)$$

The gyroscope bias does not affect the measurement function, since only the attitude of the satellite is affecting the direction of the measured vectors, therefore

$$\frac{\partial \mathbf{h}^\dagger}{\partial (\delta \beta)} = \mathbf{0} . \quad (3.30b)$$

Using the measurement sensitivity (3.30a) for the vector measurements $\mathbf{v} \in \{\mathbf{b}, \mathbf{s}\}$ gives the full measurement sensitivity matrix (3.28) as

$$\mathbf{H}_k(\hat{\chi}_k^-) = \begin{bmatrix} [\mathbf{R}(\hat{\mathbf{q}}_k) \bar{\mathbf{b}}_{I,k} \times] & \mathbf{0} \\ [\mathbf{R}(\hat{\mathbf{q}}_k) \bar{\mathbf{s}}_{I,k} \times] & \mathbf{0} \end{bmatrix} . \quad (3.31)$$

The Kalman gain matrix \mathbf{L}_k is calculated in the well known form (cf. [33])

$$\mathbf{L}_k = \mathbf{P}_k^- \mathbf{H}_k^T \left(\mathbf{H}_k \mathbf{P}_k^- \mathbf{H}_k^T + \boldsymbol{\Sigma}_k \right)^{-1}, \quad (3.32)$$

with the error covariance matrix \mathbf{P}_k^- and the covariance matrix of the measurement noise $\boldsymbol{\Sigma}_k$.

Using the gain matrix \mathbf{L}_k , the update of the observer states is calculated as

$$\boldsymbol{\chi}_k^+ = \begin{bmatrix} \delta \hat{\boldsymbol{\vartheta}}_k^+ \\ \delta \hat{\boldsymbol{\beta}}_k^+ \end{bmatrix} = \mathbf{L}_k \left(\mathbf{y}_k - \mathbf{h}_k \left(\hat{\boldsymbol{\chi}}_k^- \right) \right). \quad (3.33)$$

With the small angle approximation $\delta \mathbf{q}(\delta \boldsymbol{\vartheta}) = \mathbf{q}_I + \frac{1}{2} \begin{bmatrix} 0 \\ \delta \boldsymbol{\vartheta} \end{bmatrix}$, the estimated quaternion $\hat{\mathbf{q}}$ is updated as

$$\begin{aligned} \hat{\mathbf{q}}_k^\dagger &= \delta \mathbf{q} \left(\delta \hat{\boldsymbol{\vartheta}}_k^+ \right) \otimes \hat{\mathbf{q}}_k^- \approx \hat{\mathbf{q}}_k^- + \frac{1}{2} \begin{bmatrix} 0 \\ \delta \hat{\boldsymbol{\vartheta}}_k^+ \end{bmatrix} \otimes \hat{\mathbf{q}}_k^- \\ \hat{\mathbf{q}}_k^+ &= \frac{\hat{\mathbf{q}}_k^\dagger}{\left\| \hat{\mathbf{q}}_k^\dagger \right\|}, \end{aligned} \quad (3.34)$$

where the renormalization is crucial since the addition of two normalized quaternions can not be a normalized quaternion anymore. Equation (3.34) updates the global representation $\hat{\mathbf{q}}_k$ with the a posteriori information of the local representation $\delta \hat{\boldsymbol{\vartheta}}_k$.

The estimated gyroscope bias is updated using

$$\hat{\boldsymbol{\beta}}_k^+ = \hat{\boldsymbol{\beta}}_k^- + \delta \hat{\boldsymbol{\beta}}_k^+, \quad (3.35a)$$

which gives the estimated angular velocity as

$$\hat{\boldsymbol{\omega}}_k = \tilde{\boldsymbol{\omega}}_k - \hat{\boldsymbol{\beta}}_k^+ \quad (3.35b)$$

according to (3.21b).

The error covariance matrix \mathbf{P} is updated as (cf. [33])

$$\mathbf{P}_k^+ = (\mathbf{I}_6 - \mathbf{L}_k \mathbf{H}_k) \mathbf{P}_k^-. \quad (3.36)$$

The propagation of the quaternion is achieved using the exact discretization (cf. [54]) of the attitude kinematics (2.6)

$$\hat{\mathbf{q}}_{k+1}^- = \exp \left(\frac{1}{2} \left[\begin{bmatrix} 0 \\ \hat{\boldsymbol{\omega}}_k \end{bmatrix} \otimes \right] T_s \right) \hat{\mathbf{q}}_k^+, \quad (3.37)$$

where \exp is the matrix exponential and T_s the sampling time.

As stated before the estimated bias does not result from a dynamic equation. Therefore, the update follows a simple summation of the a priori information and the updated

difference bias $\delta\boldsymbol{\beta}$ and the propagation gives the a priori information for the next time-step by using the actual a posteriori information

$$\hat{\boldsymbol{\beta}}_{k+1}^- = \hat{\boldsymbol{\beta}}_k^+ . \quad (3.38)$$

The propagation of the error covariance matrix \mathbf{P} is formulated using the time-discrete dynamic model of the observed variables (3.25) (cf. [31]) and calculates as

$$\mathbf{P}_{k+1}^- = \boldsymbol{\Phi}_k \mathbf{P}_k^+ \boldsymbol{\Phi}_k^T + \boldsymbol{\Lambda}_k \mathbf{Q}_k \boldsymbol{\Lambda}_k^T . \quad (3.39)$$

Earth's shadow

As pointed out before, two independent vectors are necessary to calculate the attitude. When the Earth is located in between the Sun and the satellite, the vector to the Sun can not be determined due to the Earth's shadow. Without the Sun measurement the attitude can not be determined and the attitude information can not be used to estimate the gyroscope bias. This underdetermined problem can not be solved without additional measurements and it was chosen to turn off the EKF during periods of being in the Earth's shadow.

Summarized algorithm

The covariance matrices of model errors \mathbf{Q}_k and measurement errors $\boldsymbol{\Sigma}_k$ are defined as (cf. [55])

$$\mathbf{Q}_k = k_{\mathbf{Q}} \begin{bmatrix} \sigma_{\boldsymbol{\omega}}^2 & \mathbf{0} \\ \mathbf{0} & \sigma_{\boldsymbol{\beta}}^2 \end{bmatrix} \quad (3.40a)$$

$$\boldsymbol{\Sigma}_k = k_{\boldsymbol{\Sigma}} \begin{bmatrix} \sigma_{\mathbf{b}}^2 & \mathbf{0} \\ \mathbf{0} & \sigma_{\mathbf{s}}^2 \end{bmatrix} , \quad (3.40b)$$

where σ_i^2 describes the variance of the related noise vectors $\boldsymbol{\eta}_i$ for $i \in \{\mathbf{b}, \mathbf{s}, \boldsymbol{\omega}\}$ and $\sigma_{\boldsymbol{\beta}}^2$ describes the variance of the expected bias. The positive scalar factors $k_{\boldsymbol{\Sigma}}$ and $k_{\mathbf{Q}}$ are used to tune the filter. The variances σ_i^2 , $i \in \{\mathbf{b}, \mathbf{s}, \boldsymbol{\omega}, \boldsymbol{\beta}\}$ are obtained from the sensor datasheets.

The initial error covariance matrix \mathbf{P}_0 weights the estimation error at the moment of initializing the Extended Kalman Filter and is chosen as a diagonal matrix.

The Extended Kalman Filter algorithm is implemented as following

initialization

$$\hat{\mathbf{q}}_0^- = \mathbf{q}_{OI,0}, \quad \hat{\boldsymbol{\beta}}_0^- = \mathbf{0}, \quad \mathbf{P}_0^- = \mathbf{P}_0$$

loop

if $\|\tilde{\mathbf{s}}\| \leq \tilde{\mathbf{s}}_{min}$ **then**

$$\hat{\mathbf{q}}_{k+1}^- = \mathbf{q}_{OI,k+1}$$

$$\hat{\boldsymbol{\beta}}_{k+1}^- = \hat{\boldsymbol{\beta}}_k^-$$

$$\mathbf{P}_{k+1}^- = \mathbf{P}_k^-$$

else

measurement

$$\zeta_{\mathbf{h}_k} = \mathbf{y}_k - \mathbf{h}_k(\hat{\boldsymbol{\chi}}_{,k}^-)$$

$$\mathbf{H}_k = \begin{bmatrix} \mathbf{R}(\hat{\mathbf{q}}_k^-) \bar{\mathbf{b}}_{I,k} \times & \mathbf{0} \\ \mathbf{R}(\hat{\mathbf{q}}_k^-) \bar{\mathbf{s}}_{I,k} \times & \mathbf{0} \end{bmatrix}$$

gain

$$\mathbf{L}_k = \mathbf{P}_k^- \mathbf{H}_k (\mathbf{H}_k \mathbf{P}_k^- \mathbf{H}_k^T + \boldsymbol{\Sigma}_k)$$

update

$$\hat{\boldsymbol{\chi}}_k^+ = \mathbf{L}_k \zeta_{\mathbf{h}_k}$$

$$\hat{\mathbf{q}}_k^\dagger = \hat{\mathbf{q}}_k^- + \frac{1}{2} \begin{bmatrix} 0 \\ \delta \hat{\boldsymbol{\vartheta}}_k^+ \end{bmatrix} \otimes \hat{\mathbf{q}}_k^-$$

$$\hat{\mathbf{q}}_k^+ = \frac{\hat{\mathbf{q}}_k^\dagger}{\|\hat{\mathbf{q}}_k^\dagger\|}$$

$$\hat{\boldsymbol{\beta}}_k^+ = \hat{\boldsymbol{\beta}}_k^- + \delta \hat{\boldsymbol{\beta}}_k^+$$

$$\hat{\boldsymbol{\omega}}_k = \tilde{\boldsymbol{\omega}}_k - \hat{\boldsymbol{\beta}}_k^+$$

$$\mathbf{P}_k^+ = (\mathbf{I}_6 - \mathbf{L}_k \mathbf{H}_k) \mathbf{P}_k^-$$

propagation

$$\hat{\mathbf{q}}_{k+1}^- = \exp\left(\frac{1}{2} \begin{bmatrix} 0 \\ \hat{\boldsymbol{\omega}}_k \end{bmatrix} \otimes T_s\right) \hat{\mathbf{q}}_k^+$$

$$\hat{\boldsymbol{\beta}}_{k+1}^- = \hat{\boldsymbol{\beta}}_k^+$$

$$\mathbf{P}_{k+1}^- = \boldsymbol{\Phi}_k \mathbf{P}_k^+ \boldsymbol{\Phi}_k^T + \boldsymbol{\Lambda}_k \mathbf{Q}_k \boldsymbol{\Lambda}_k^T$$

end if

end loop

3.3 Attitude control

As mentioned in Section 1.2, a PD control law is chosen to stabilize the attitude of the satellite. In [26] the control law

$$\mathbf{u} = -(\epsilon^2 k_{\mathbf{q}} \mathbf{q}_{BO,1:3} + \epsilon k_{\boldsymbol{\omega}} \mathbf{J}_B \boldsymbol{\omega}_{BO}) \quad (3.41)$$

with $\epsilon > 0$, $k_{\mathbf{q}} > 0$, $k_{\boldsymbol{\omega}} > 0$ being scalar gains and \mathbf{J}_B being the inertia matrix of the satellite expressed in the body frame, is used to stabilize the attitude of a magnetic actuated satellite.

The effective control torque $\boldsymbol{\tau}_{B,c}$ from (3.1) for the PD control law (3.41) follows as

$$\boldsymbol{\tau}_{B,c} = \boldsymbol{\Gamma}(t) \mathbf{u} = -(\mathbf{I}_3 - \mathbf{e}_{\mathbf{b}_B} \mathbf{e}_{\mathbf{b}_B}^T)(\epsilon^2 k_{\mathbf{q}} \mathbf{q}_{BO,1:3} + \epsilon k_{\boldsymbol{\omega}} \mathbf{J}_B \boldsymbol{\omega}_{BO}) . \quad (3.42)$$

The quaternion error \mathbf{q}_{BO} represents the rotational transformation from the desired orbit frame O to the body frame B and is calculated as

$$\mathbf{q}_{BO} = \mathbf{q}_{BI} \otimes \mathbf{q}_{OI}^{-1} , \quad (3.43a)$$

with the true attitude \mathbf{q}_{BI} and the desired attitude \mathbf{q}_{BO} , derived in Section 2.2.1. The quaternion product \otimes and the inverse of the quaternion are defined in Appendix A.

In a similar way, the angular velocity error $\boldsymbol{\omega}_{BO}$ represents the angular velocity of the orbital frame O with respect to the body frame B and is calculated as

$$\boldsymbol{\omega}_{BO} = \boldsymbol{\omega}_{BI} - \mathbf{R}(\mathbf{q}_{BO}) \boldsymbol{\omega}_{OI} , \quad (3.43b)$$

where the rotational matrix $\mathbf{R}(\mathbf{q}_{BO})$ is used to express the desired angular velocity $\boldsymbol{\omega}_{OI}$ in the body frame B .

The block diagram of the PD controller in closed-loop, as it is used in the simulation, is presented in Figure 3.3. The initial parameters t_0 and \mathbf{k}_0 are used to predict the IGRF reference magnetic field $\bar{\mathbf{b}}_I$ and the Sun vector $\bar{\mathbf{s}}_I$ as described in Section 2.3. The sensor models add the Gaussian noises $\boldsymbol{\eta}$ and the bias $\boldsymbol{\beta}$ to the reference values according to Section 2.4.2 and transforms the quantities to the body frame using the satellite's attitude \mathbf{q}_{BI} . The trajectory planning provides the desired attitude \mathbf{q}_{OI} and desired angular velocity $\boldsymbol{\omega}_{OI}$ of the satellite, as derived in Section 2.2.1. The Extended Kalman Filter uses the measured quantities, together with the reference values to estimate the satellite's attitude $\hat{\mathbf{q}}_{BI}$ and angular velocity $\hat{\boldsymbol{\omega}}_{BI}$. The model of the satellite's dynamics is affected by the disturbance torques $\boldsymbol{\tau}_{gg}, \boldsymbol{\tau}_{ad}, \boldsymbol{\tau}_{\eta}$, where $\boldsymbol{\tau}_{gg}$ is the gravity gradient torque and $\boldsymbol{\tau}_{ad}$ is the aerodynamic torque derived in Section 2.3.3. The additional disturbance torque $\boldsymbol{\tau}_{\eta}$ is assumed to be Gaussian white noise, representing neglected sources of error.

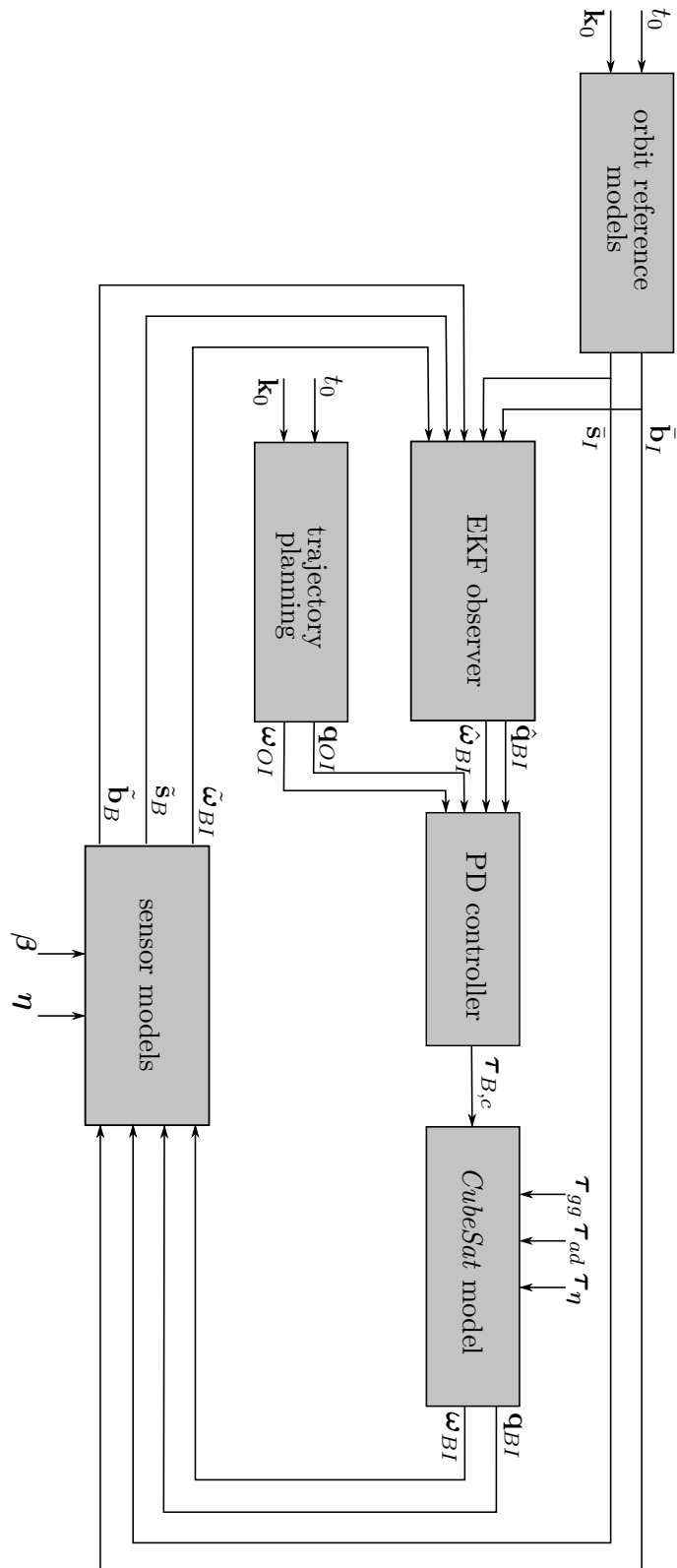


Figure 3.3: Block diagram of the PD controller in closed-loop, as used in the simulation.

Proof of stability

The stability of the state feedback control law (3.42) is proven in [26] and will be summarized here. The proof of stability consists of two steps. First, the controllability on average is shown and second, using Lyapunov methods and introducing an averaged approximation of the system (2.14), the almost global stability of the system (2.14) is shown.

Controllability on average

As pointed out earlier, the input matrix $\mathbf{\Gamma}(t)$ is singular at every instance of time, representing the underactuation of the magnetic actuated satellite. Due to the variation of the magnetic field along the orbit, this underactuation is not constant but varying with time. Using Khalil's averaging theory [25] the controllability on average is shown.

For that, the matrix $\mathbf{\Gamma}_I(t)$ is averaged along the trajectory of the desired orbit

$$\bar{\mathbf{\Gamma}}_I = \lim_{T \rightarrow \infty} \frac{1}{T} \int_0^T (\mathbf{I}_3 - \mathbf{e}_{\mathbf{b}_I}(t) \mathbf{e}_{\mathbf{b}_I}^T(t)) dt, \quad (3.44)$$

where $\bar{\mathbf{b}}_I(t)$ represents the Earth's magnetic field along the orbit, expressed in the inertial frame. The matrix $\bar{\mathbf{\Gamma}}_I$ is positive definite as long as the orbit plane does not coincide with the geomagnetic equator. This was shown by Bhat in [20].

According to Lemma 1 in [26], the positive definiteness of $\bar{\mathbf{\Gamma}}_I$ implies that there exists an upper bound ω_M for the spacecraft's angular velocity $\|\boldsymbol{\omega}_{BI}\| < \omega_M$ such that $\bar{\mathbf{\Gamma}} > \mathbf{0}$ for all $t > \bar{t}$ for the lower bound $0 < \bar{t} < \infty$ with

$$\bar{\mathbf{\Gamma}} = \lim_{T \rightarrow \infty} \frac{1}{T} \int_0^T (\mathbf{I}_3 - \mathbf{e}_{\mathbf{b}_B}(t) \mathbf{e}_{\mathbf{b}_B}^T(t)) dt \quad (3.45)$$

being the average of the input matrix $\mathbf{\Gamma}(t)$ from (3.42). This Lemma is proven in [26] for the particular case $\boldsymbol{\omega}_{BI} = \mathbf{0}$. The averaged input matrix $\bar{\mathbf{\Gamma}}$ along the trajectory is only singular if the magnetic field \mathbf{b}_B is constant in the body reference frame for all $t \in [0, \infty)$. This particular case can only arise if the satellite's angular velocity is sufficiently large to compensate the natural variation of the Earth's magnetic field \mathbf{b}_B (cf. [26] and especially [51]).

In Figure 3.4, the evolution of the eigenvalues of the averaged input matrix $\bar{\mathbf{\Gamma}}$ along the *QB50* orbit is depicted. At $t = 0$ the matrix $\bar{\mathbf{\Gamma}}$ is singular with eigenvalues $(1, 1, 0)$ converging to a nonsingular matrix fulfilling the controllability condition $\bar{\mathbf{\Gamma}} > \mathbf{0}$. Therefore, controllability on average is given.

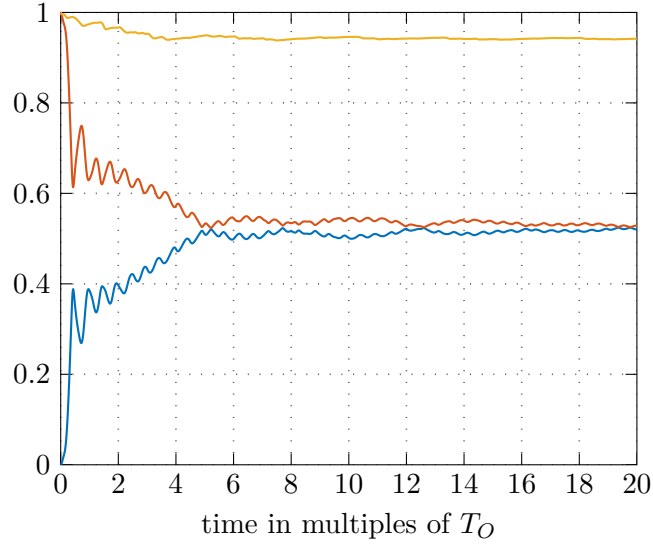


Figure 3.4: Eigenvalues of the averaged matrix $\bar{\Gamma}$ along the *QB50* orbit.

Attitude stabilization

Using the state feedback PD control law (3.41), Lovera and Astolfi make the following proposition.

If $\mathbf{0} < \bar{\Gamma}_I < \mathbf{I}_3$ is fulfilled, then there exist some $\epsilon^* > 0, k_{\mathbf{q}} > 0, k_{\boldsymbol{\omega}} > 0$ with

$$k_{\boldsymbol{\omega}}^2 > k_{\mathbf{q}} \frac{\sigma_{\min}^2(\bar{\Gamma})}{\sigma_{\min}(\mathbf{J}_B)} \sqrt{\text{CN}(\bar{\Gamma})}, \quad (3.46)$$

where $\sigma_{\min}(\mathbf{J}_B)$ is the minimal singular value of the matrix \mathbf{J}_B and $\text{CN}(\bar{\Gamma})$ is the condition number of $\bar{\Gamma}$ (cf. [56]), such that for any $0 < \epsilon < \epsilon^*$ the control law (3.41) ensures local exponential stability of the closed-loop system for the equilibrium $\mathbf{x}_e = \begin{bmatrix} \mathbf{q}_I \\ \mathbf{0} \end{bmatrix}$.

The Lyapunov function

$$V_1(\mathbf{q}_{BO}, \boldsymbol{\omega}_{BO}) = \frac{\lambda}{2} \boldsymbol{\omega}_{BO}^T \mathbf{J}_B^2 \boldsymbol{\omega}_{BO} - \frac{1}{2} \boldsymbol{\omega}_{BO}^T \mathbf{J}_B \mathbf{R}(\mathbf{q}_{BO}) \mathbf{M}(t) \mathbf{R}^T(\mathbf{q}_{BO}) \mathbf{J}_B \boldsymbol{\omega}_{BO}, \quad (3.47)$$

with a sufficiently large $\lambda > 0$ and $\mathbf{M}(t) = \int_0^t (\mathbf{e}_{\mathbf{b}_I}(\tau) \mathbf{e}_{\mathbf{b}_I}^T(\tau) - \mathbf{N}) d\tau$, with the constant matrix $\mathbf{N} \geq \mathbf{0}$ is used to show that $\bar{\Gamma} > \mathbf{0}$. The time derivative of (3.47) implies that for any $\boldsymbol{\omega}_M > \mathbf{0}$ there exists an $\epsilon > 0$ such that the angular velocities of the satellite are bounded $\|\boldsymbol{\omega}_{BO}\| < \boldsymbol{\omega}_M$. Together with Lemma 1 from [26] this proves $\bar{\Gamma} > \mathbf{0}$.

Introducing a coordinate transformation of the form

$$\mathbf{z}_1 = \mathbf{q}_{BO,1:3}, \quad \mathbf{z}_2 = \frac{\boldsymbol{\omega}_{BO}}{\epsilon}, \quad \mathbf{z} = \begin{bmatrix} q_{BO,0} \\ \mathbf{z}_1 \\ \mathbf{z}_2 \end{bmatrix}, \quad (3.48)$$

substituting into the dynamic system of the satellite (2.14), and utilizing the control law (3.42) gives the time-variant dynamic system of the closed-loop

$$\dot{\mathbf{z}}_1 = \epsilon \frac{1}{2} \left[\begin{array}{c} 0 \\ \mathbf{z}_2 \end{array} \right] \otimes \mathbf{z}_1 \quad (3.49a)$$

$$\mathbf{J}_B \dot{\mathbf{z}}_2 = -\epsilon [\mathbf{z}_2 \times] \mathbf{J}_B \mathbf{z}_2 + \epsilon \Gamma(t) (-k_q \mathbf{z}_1 - k_\omega \mathbf{J}_B \mathbf{z}_2) . \quad (3.49b)$$

The time-variant dynamic system (3.49) fulfills all conditions to apply Khalil's averaging theory [25], yielding the time-invariant averaged system

$$\dot{\mathbf{z}}_1 = \epsilon \frac{1}{2} \left[\begin{array}{c} 0 \\ \mathbf{z}_2 \end{array} \right] \otimes \mathbf{z}_1 \quad (3.50a)$$

$$\mathbf{J}_B \dot{\mathbf{z}}_2 = -\epsilon [\mathbf{z}_2 \times] \mathbf{J}_B \mathbf{z}_2 + \epsilon \bar{\Gamma} (-k_q \mathbf{z}_1 - k_\omega \mathbf{J}_B \mathbf{z}_2) . \quad (3.50b)$$

The averaging theory applied to (3.49) states that there exists an $\epsilon^* > 0$ such that for any $0 < \epsilon < \epsilon^*$ the trajectory of (3.50) is close to the trajectory of (3.49) and if (3.50) is stable the time-variant system (3.49) is stable as well.

Considering the Lyapunov function

$$V_2(\mathbf{z}_2) = \frac{1}{2} \mathbf{z}_2^T \mathbf{J}_B^2 \mathbf{z}_2 , \quad (3.51)$$

gives the possibility to show

$$\|\mathbf{z}_2\| \leq \frac{k_q}{k_\omega \sigma_{\min}(\mathbf{J}_B)} \sqrt{\text{CN}(\bar{\Gamma})} = K , \text{ for all } t > t^* , \quad (3.52a)$$

where $\sigma_{\min}(\mathbf{J}_B)$ is the minimal singular value of the matrix \mathbf{J}_B and $\text{CN}(\bar{\Gamma})$ is the condition number of $\bar{\Gamma}$ (cf. [56]). Therefore, for any $K > 0$ the set

$$Z_K = \{(\mathbf{z}_1, \mathbf{z}_2) : \|\mathbf{z}_2\| < K\} \quad (3.52b)$$

represents an attractive, positively invariant set. By choosing k_q and k_ω , K can be made arbitrarily small.

Using the Lyapunov function

$$V_3(\mathbf{z}_1, \mathbf{z}_2) = \frac{1}{2} k_q (\mathbf{z}_1^T \mathbf{z}_1 + (q_{BO,0} - 1)^2) + \frac{1}{2} \mathbf{z}_2^T \bar{\Gamma}^{-1} \mathbf{z}_2 , \quad (3.53)$$

applying Lyapunov's direct method and Krasovskii-LaSalle's invariance principle shows the asymptotic stability of the averaged system if condition (3.46) is fulfilled, for all trajectories starting in the set Z_K .

Linearizing the dynamic system (3.50) around the equilibrium $\mathbf{z}_e = \begin{bmatrix} \mathbf{q}_I \\ \mathbf{0} \end{bmatrix}$ yields

$$\Delta \dot{\mathbf{z}}_1 = \frac{1}{2} \epsilon \Delta \mathbf{z}_2 \quad (3.54a)$$

$$\mathbf{J}_B \Delta \mathbf{z}_2 = -\epsilon \bar{\Gamma} (k_q \Delta \mathbf{z}_1 + k_\omega \mathbf{J}_B \Delta \mathbf{z}_2) . \quad (3.54b)$$

Applying Lyapunov's direct method to the linearized system (3.54) using the Lyapunov function

$$V_4(\Delta \mathbf{z}_1, \Delta \mathbf{z}_2) = 2k_q \Delta \mathbf{z}_1^T \Delta \mathbf{z}_1 + \Delta \mathbf{z}_2^T \bar{\Gamma}^{-1} \Delta \mathbf{z}_2 \quad (3.55)$$

shows the local exponential stability of the averaged system at \mathbf{z}_e .

Introducing the definition of almost global stability as written in [26], "Given a system $\dot{x} = f(x)$ we say that an equilibrium x_0 is almost globally asymptotically stable if it is locally asymptotically stable, all the trajectories of the system are bounded and the set of initial conditions giving rise to trajectories which do not converge to x_0 has zero Lebesgue measure" and applying the prior results shows the almost global stability of the averaged closed-loop system. The Lebesgue measure is introduced, e. g., in [57].

Therefore, according to the averaging theory, the magnetic actuated spacecraft described by the dynamic system (2.14) in closed-loop with the control law (3.41) is almost globally stable.

3.4 Chapter conclusion

In this section, a strategy has been presented leading the satellite to a given trajectory. Two different control laws were derived for two different phases of the satellite motion. If high angular velocities are measured, e. g. after tip-off, a detumbling controller is used to slow down the satellite. Using an Extended Kalman Filter, the attitude of the satellite is estimated together with an estimation of the gyroscope bias. With these estimated states, a state feedback law of PD form is used to follow the trajectory.

When the satellite is located in the Earth's shadow the estimator and the controllers are switched off, following the slogan better do nothing than do something wrong. For both control laws the stability of the equilibria has been studied using Lyapunov methods and almost global stability was proven using Khalil's averaging theory.

4 Implementation and simulation

In this chapter, the derived attitude control strategy is verified via simulation. Details concerning the implementation and the used set of parameters are given, followed by various plots of the satellite's states in comparison with the desired trajectories. Plots of the power consumption and magnetorquer currents are given to show that the current limits are met.

After showing the quantities for the full simulation time, a detailed investigation of the different controllers is given. With an enlarged view of two orbits the effect of the underactuation is discussed and the performance of the EKF attitude determination is shown.

The models of Chapter 2 and the control strategy from Chapter 3 are implemented and simulated using MATLAB/SIMULINK¹.

4.1 Implementation

The parameters of the *CubeSat Pegasus* satellite are summarized in Table 4.1. These parameters are used to calculate the model of the rigid body dynamics (2.13b) and the satellite's quantities in the disturbance torques from Section 2.3.3.

quantity	variable	value
length in x_B	l_x	227 mm
length in y_B	l_y	100 mm
length in z_B	l_z	100 mm
total mass	m	1.622 kg
satellite's geometric center in x_B	x_{gc}	-3 mm
satellite's geometric center in y_B	y_{gc}	-0.5 mm
satellite's geometric center in z_B	z_{gc}	-0.5 mm
inertia matrix	J_{xx}	$2.70 \cdot 10^{-3} \text{ kg m}^2$
	J_{yy}, J_{zz}	$8.30 \cdot 10^{-3} \text{ kg m}^2$
	J_{xy}, J_{xz}	$-2.43 \cdot 10^{-6} \text{ kg m}^2$
	J_{yz}	$-40.55 \cdot 10^{-6} \text{ kg m}^2$
drag coefficient	C_d	2

Table 4.1: Simulation parameters of *CubeSat Pegasus*.

The symmetric, positive definite inertia matrix \mathbf{J}_B (cf. [42]) with the principal moments of inertia J_{xx}, J_{yy}, J_{zz} and the cross products of inertia J_{xy}, J_{xz}, J_{yz} from Table 4.1 follows

¹version 8.6 (R2015b)

as

$$\mathbf{J}_B = \begin{bmatrix} J_{xx} & J_{xy} & J_{xz} \\ J_{xy} & J_{yy} & J_{yz} \\ J_{xz} & J_{yz} & J_{zz} \end{bmatrix} = \begin{bmatrix} 2.70 \cdot 10^{-3} & -2.43 \cdot 10^{-6} & -2.43 \cdot 10^{-6} \\ -2.43 \cdot 10^{-6} & 8.3 \cdot 10^{-3} & -40.55 \cdot 10^{-6} \\ -2.43 \cdot 10^{-6} & -40.55 \cdot 10^{-6} & 8.3 \cdot 10^{-3} \end{bmatrix} \text{ kg m}^2 . \quad (4.1)$$

The desired trajectory (2.18) is calculated as explained in Section 2.2.1 using the orbital elements from Table 4.2. The initial time t_0 and the initial angles Ω_0 and ν_0 are arbitrary in principle, the inclination i and the altitude a are given by the *QB50* requirements.

quantity	variable	value
initial time	t_0	April 16, 2016, 20:15, UTC0
altitude	a	450 km
eccentricity	e	0
initial anomaly	ν_0	84°
inclination	i	98°
initial right ascension	Ω_0	250°
argument of perigee	ω	0

Table 4.2: Simulation parameters of the *QB50* orbit.

The parameters of the environment are listed in Table 4.3 (cf. [49]), where the atmospheric density ρ is calculated using the Exponential Decaying Model (cf. [31]).

quantity	variable	value
Earth's radius	r_E	6371 km
Earth's mass	M	$5.974 \cdot 10^{24}$ kg
gravitational constant	G	$6.67384 \cdot 10^{-11}$ m ³ /(kg s ²)
period of a tropical year	T_{trop}	31 556 925.261 s
atmospheric density	ρ	$1.585 \cdot 10^{-12}$ kg/m ³

Table 4.3: Simulation parameters of the environment.

According to [31] the velocity of the satellite along the orbit is calculated as

$$v_B = \sqrt{\frac{\mu}{r_O}} , \quad (4.2)$$

where $\mu = GM$ is the gravitational parameter of the Earth and $r_O = r_E + a$ is the radius of the orbit. Using the given values of the orbit and the environment from Table 4.2 and Table 4.3, the satellite's velocity v_B follows as

$$v_B = 7.6453 \text{ km/s} .$$

The orbit period T_O of the *QB50* mission is calculated by

$$T_O = \frac{2\pi r_O}{v_B} \quad (4.3)$$

and follows as

$$T_O = 5605.7 \text{ s} = 93 \text{ min } 25.7 \text{ s} ,$$

for the particular orbit.

The measurement errors introduced in Section 2.4.2 are characterized by the parameters of Table 4.4. The variances of the measurement errors are chosen using the sensor datasheets and taking redundancies and oversampling into account. The power spectral densities (PSD) are tuned to result in this given variances using band-limited white noise with a sampling time of $T_s = 100 \text{ ms}$.

In order to simulate the gyroscope bias, a sine wave with an amplitude β_{amp} and the period of the orbit T_O is added to the angular velocity. The additional bias $\beta(t)$ from (2.36) is implemented as

$$\beta(t) = \sin\left(\frac{2\pi t}{T_O}\right) \begin{bmatrix} \beta_{amp} \\ -\beta_{amp} \\ \beta_{amp} \end{bmatrix} . \quad (4.4)$$

The simulation of the Earth's shadow is implemented by multiplying the measured Sun vector $\tilde{\mathbf{s}}$ with a trapezoid function $\Pi(t)$, defined as

$$\Pi(t) = \begin{cases} \frac{0.35-t_r}{0.1}, & 0.25 < t_r < 0.35 \\ 0, & 0.35 < t_r < 0.55 \\ \frac{t_r-0.55}{0.1}, & 0.55 < t_r < 0.65 \\ 1, & \text{else} \end{cases} , \quad \text{with } t_r = \frac{(t \bmod T_O)}{T_O} \quad (4.5)$$

where $(t \bmod T_O)$ is the modulo of t by T_O (cf. [58]).

quantity	variable	value
PSD of the magnetometer measurement noise	$P_{\eta,\mathbf{b}}$	$1 \cdot 10^{-14} \text{ T}^2/\text{Hz}$
PSD of the Sun vector measurement noise	$P_{\eta,\mathbf{s}}$	$1 \cdot 10^{-5} \text{ 1/Hz}$
PSD of the gyroscope measurement noise	$P_{\eta,\omega}$	$1 \cdot 10^{-7} \text{ rad}^2/(\text{s}^2 \text{ Hz})$
variance of the magnetometer measurement noise	$\sigma_{\mathbf{b}}$	$3.22 \cdot 10^{-7} \text{ T}$
variance of the Sun vector measurement noise	$\sigma_{\mathbf{s}}$	$10.2 \cdot 10^{-3}$
variance of the gyroscope measurement noise	σ_{ω}	$1 \cdot 10^{-3} \text{ rad/s}$
variance of the bias	σ_{β}	$21.3 \cdot 10^{-3} \text{ rad/s}$
amplitude of the gyroscope bias	β_{amp}	$20 \cdot 10^{-3} \text{ radian/s}$

Table 4.4: Simulation parameters of the sensors.

Using the design method for the magnetorquers presented in Section 2.4.1 optimal values for the number of turns n^* and the width of the trace w_t^* are calculated. The optimization problem with constraints

$$(n^*, w_t^*) = \arg \max_{(n, w_t)} m(n, w_t) \quad (4.6a)$$

$$\text{s.t. } 0 \leq i_{max} - i(n, w_t) \quad (4.6b)$$

$$0 \leq (l_y - l_{y,in}) - 2nl_{\Delta} \quad (4.6c)$$

$$w_t \geq 150 \mu\text{m} , \quad (4.6d)$$

where the additional restriction $w_t \geq 150 \mu\text{m}$ arises from manufacturing reasons, is given. The fixed values used in the calculation are provided in Table 4.5. Using MAT-

quantity	variable	value
magnetorquer length	l_x	187 mm
magnetorquer width	l_y	93.5 mm
supply voltage	U_s	5 V
maximal current	i_{\max}	100 mA
space between two traces	w_s	150 μm
height of the trace	h_t	105 μm
electrical resistivity of copper	ρ_{Cu}	$17.212 \cdot 10^{-9} \Omega \text{m}$

Table 4.5: Parameters used in the magnetorquer optimization.

LAB/SIMULINK² the optimal values are found to be

$$n^* = 104.8 \approx 105, \quad w_t^* = 150 \mu\text{m}. \quad (4.7)$$

Because of design reasons, slightly different values were actually implemented in *CubeSat*

quantity	variable	value
area of the top surface	$A_{avg,x}$	4971 mm ²
number of turns of top surface	n_x	81
area of the other surfaces	$A_{avg,i}, i \in \{y, -y, z, -z\}$	5313 mm ²
number of turns of the other surfaces	$n_i, i \in \{y, -y, z, -z\}$	130
maximum current for each magnetorquer	i_{\max}	100 mA

Table 4.6: Simulation parameters of the actuators.

Pegasus. The values provided by the TU Wien *Space Team* are listed in Table 4.6.

The scalar tuning gains of the Extended Kalman Filter, introduced in Section 3.2, are given in Table 4.7. Their choice gives a compromise between smoothing and time lag after starting the EKF algorithm. The gains for the PD controller and the chosen limit of the

quantity	variable	value
sampling time	T_s	100 ms
measurement error covariance gain	k_{Σ}	$5 \cdot 10^3$
model error covariance gain	$k_{\mathbf{Q}}$	10
initial error covariance matrix	\mathbf{P}_0	\mathbf{I}_6

Table 4.7: Simulation parameters of the Extended Kalman Filter.

angular velocity, where the control laws are switched, are summarized in Table 4.8.

The PD control law (3.42) utilizes the satellite's inertia matrix. To simulate the effect of model errors, a slightly different inertia matrix is used for the controller. Assuming a

²version 8.6 (R2015b), `fmincon` with `sqp` algorithm

homogeneous mass distribution and using the mass and dimensions from Table 4.1, the inertia matrix for the control law follows as

$$\mathbf{J}_B = \begin{bmatrix} \frac{1}{12}m(l_y^2 + l_z^2) & 0 & 0 \\ 0 & \frac{1}{12}m(l_x^2 + l_z^2) & 0 \\ 0 & 0 & \frac{1}{12}m(l_x^2 + l_y^2) \end{bmatrix} = \begin{bmatrix} 2.7 & 0 & 0 \\ 0 & 8.3 & 0 \\ 0 & 0 & 8.3 \end{bmatrix} 1 \cdot 10^{-3} \text{ kg m}^2, \quad (4.8a)$$

with zeros cross products of inertia.

quantity	variable	value
sampling time	T_s	100 ms
scalar gain for the PD controller	ϵ	$1 \cdot 10^{-5}$
scalar gain for the attitude error	$k_{\mathbf{q}}$	100
scalar gain for the angular velocity error	$k_{\boldsymbol{\omega}}$	250
angular velocity limit	ω_{PD}	$5 \cdot 10^{-3} \text{ rad/s} = 0.29^\circ/\text{s}$

Table 4.8: Simulation parameters of the controllers.

Choosing the controller gains as stated in Table 4.8 fulfills the required stability condition

$$k_{\boldsymbol{\omega}}^2 > k_{\mathbf{q}} \frac{\sigma_{\min}^2(\bar{\boldsymbol{\Gamma}})}{\sigma_{\min}(\mathbf{J}_B)} \sqrt{\text{CN}(\bar{\boldsymbol{\Gamma}})}$$

from (3.46). The evolution of this condition along the *QB50* orbit is presented in Figure 4.1. The condition is clearly fulfilled for the *QB50* orbit, and therefore according to [26] almost global stability is given.

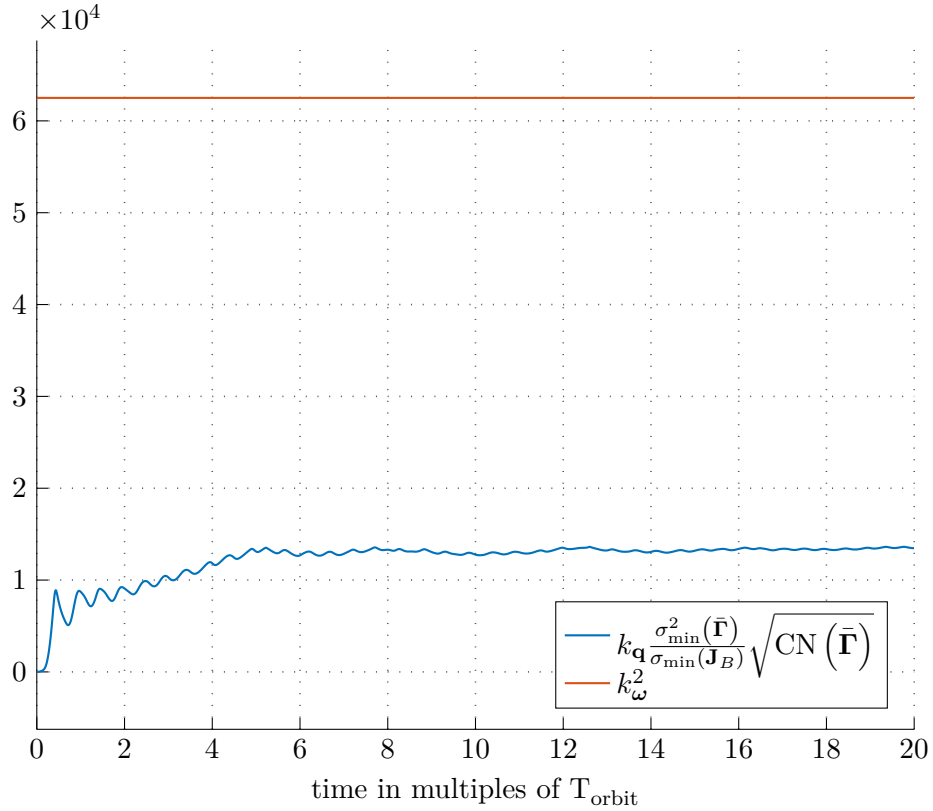


Figure 4.1: Condition (3.46) along the desired orbit.

The gravity gradient and aerodynamic torques acting on the satellite are implemented as explained in Section 2.3.3. An additional Gaussian disturbance torque τ_{η} representing the neglected disturbances is taken into account in the simulation as well. The power spectral density of τ_{η} is assumed to be $P_{\eta,\tau} = 1 \cdot 10^{-20} \text{ N}^2 \text{ m}^2/\text{Hz}$ with a sampling time of 100 ms. The disturbance torque introduced in (2.13b) is calculated as

$$\tau_{B,d} = \tau_{gg} + \tau_{ad} + \tau_{\eta} . \quad (4.9)$$

In Figure 4.2, the groundtrack of the simulated flight is shown to support the imagination of the simulation.

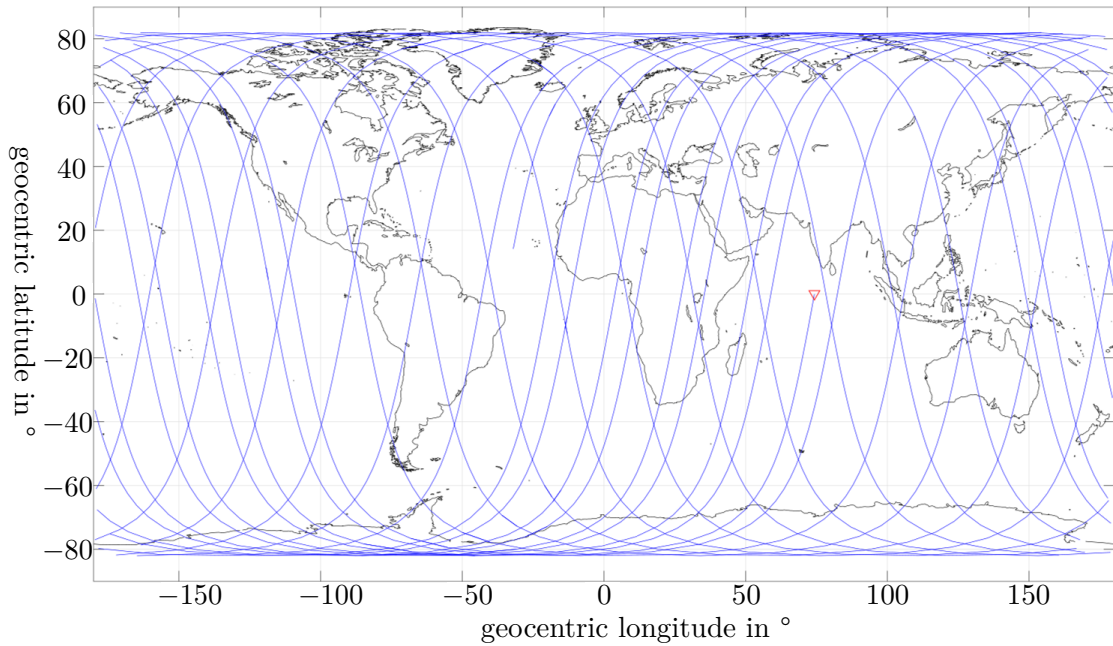


Figure 4.2: Groundtrack of the simulated scenario. The red triangle denotes the satellite's initial position and flight direction.

4.2 Simulation results

The *QB50* mission requires to stabilize the satellite within three days with a pointing accuracy of $\pm 10^\circ$. Expressed in multiples of the orbit period T_O from (4.3) three days are about $46T_O$. Since the derived control algorithm stabilizes the satellite much faster than required only $20T_O$ are shown throughout this section.

In Figure 4.3, the satellite's attitude with respect to the inertial frame is shown, expressed in the roll, pitch, and yaw angles as introduced in [42]. In the beginning, where the detumbling control law (3.4) is active, the attitude is not of interest. After switching to the PD-controller at about $1.3T_O$ the satellite's attitude is slowly approaching the desired trajectory.

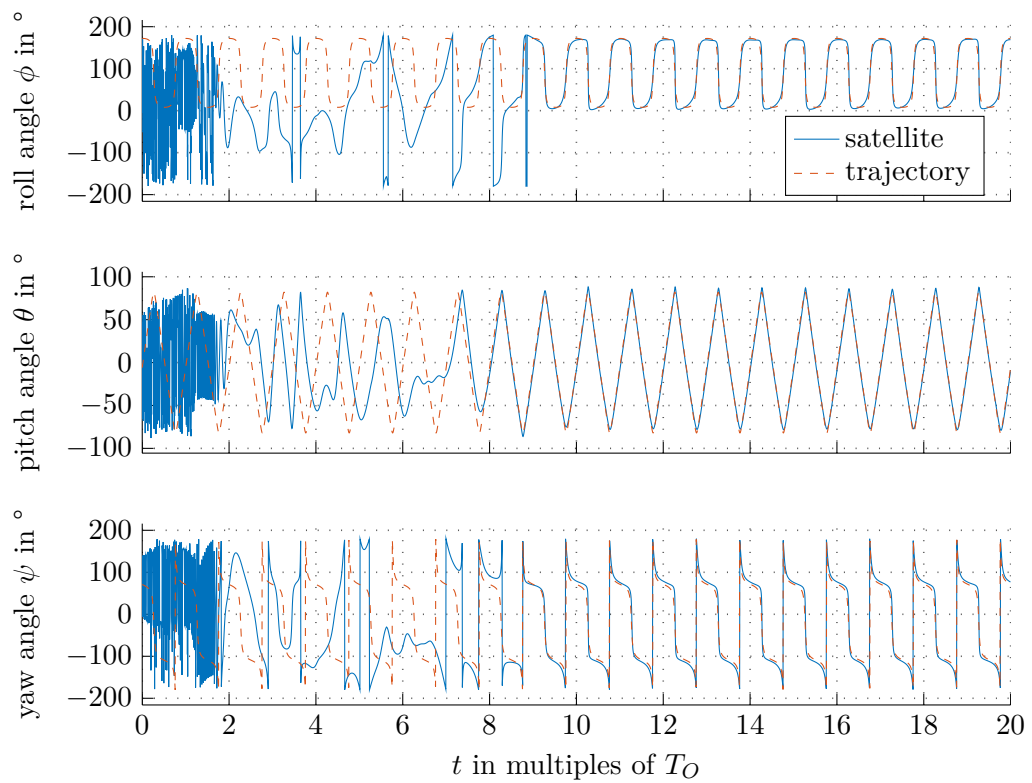


Figure 4.3: Attitude of the satellite with respect to the inertial frame, for the full simulation time.

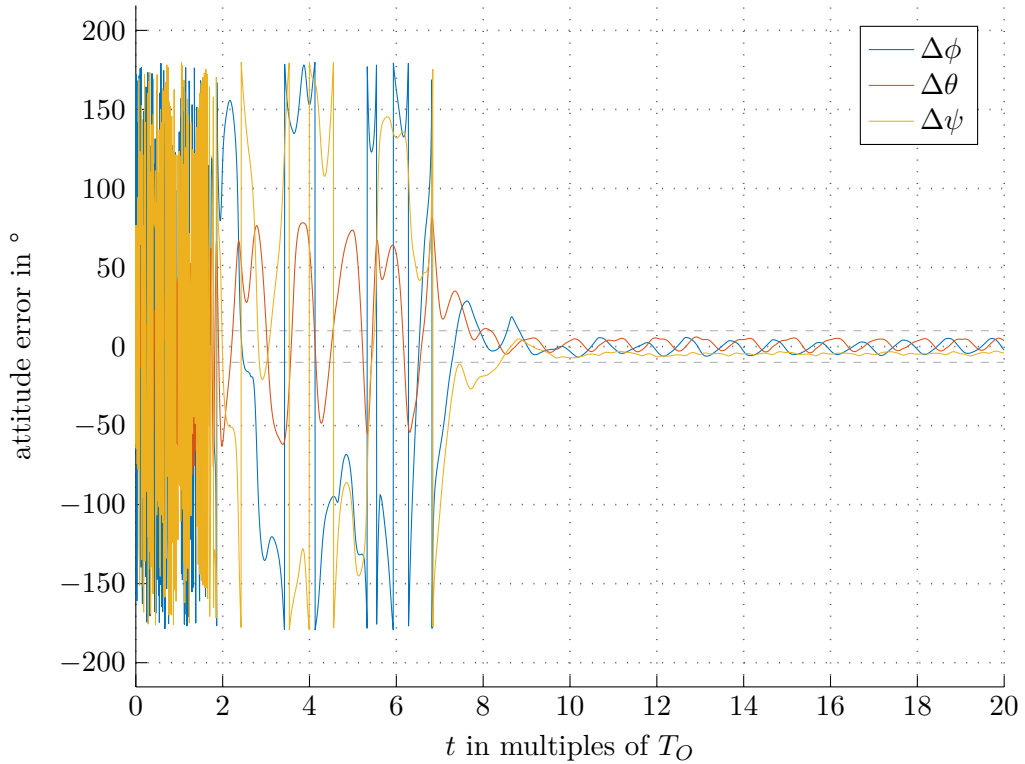


Figure 4.4: Attitude error in r.p.y. angles for the full simulation time. The dashed lines show the required pointing accuracy.

The attitude error is presented in Figure 4.4 and shows relatively fast decay. The dashed lines in Figure 4.4 represent the required accuracy of $\pm 10^\circ$. Once the attitude error falls below the required accuracy, the controller is capable to stabilize the satellite within this requirements as can be seen for the time after $10T_O$.

The satellite's angular velocity is shown in Figure 4.5. As desired, the high angular velocities after detaching from the launch vehicle decays relatively fast. Once the maximum absolute value of the measured angular velocities $\tilde{\omega}_{BI}$ falls below the limit ω_{PD} , the control strategy is switched from detumbling to attitude stabilization.

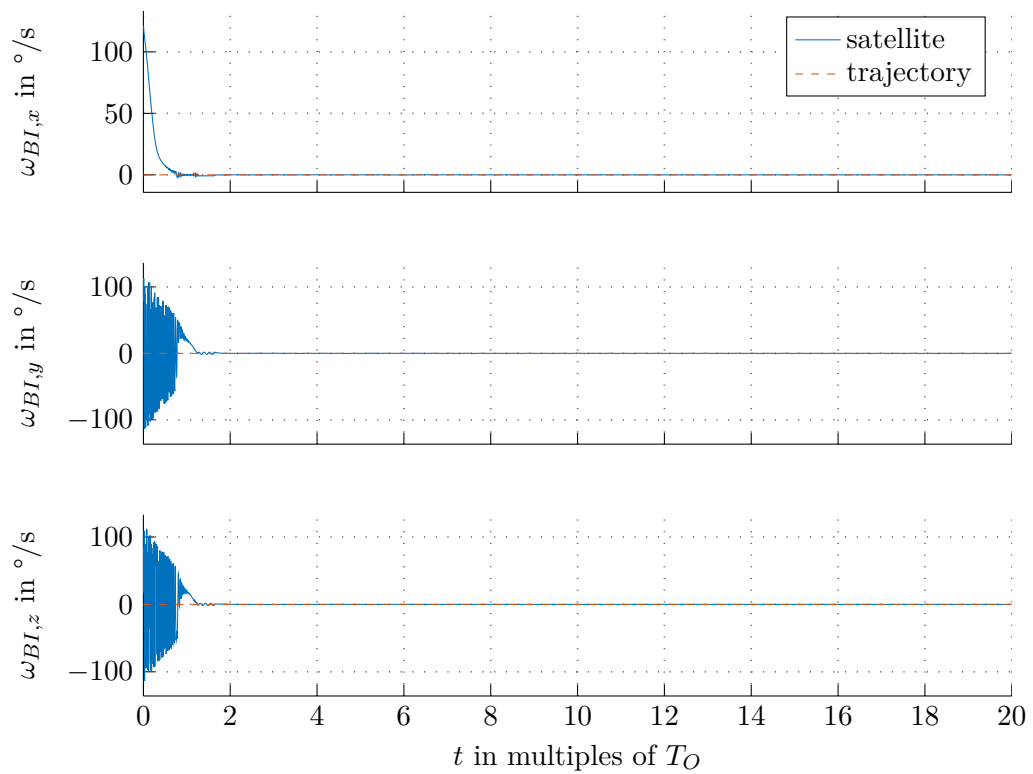


Figure 4.5: Angular velocity of the satellite w.r.t. the inertial frame for the full simulation.

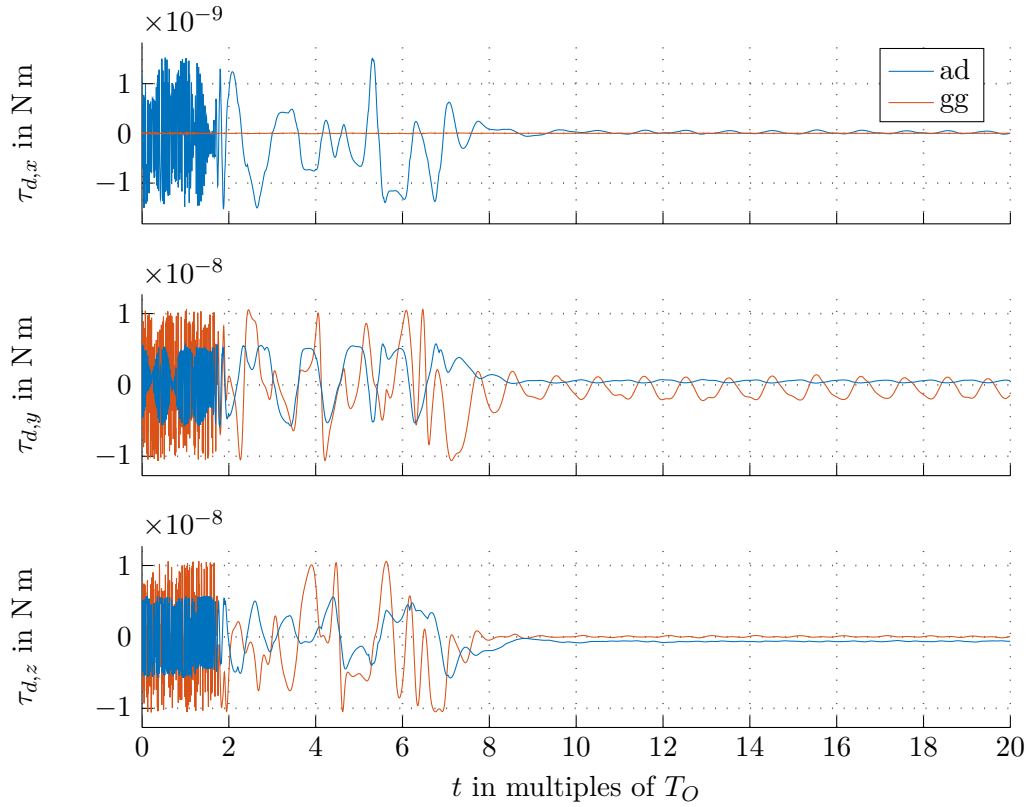


Figure 4.6: Simulated gravity gradient and atmospheric drag acting on the satellite for the full simulation.

The disturbance torques of the gravity gradient τ_{gg} and the aerodynamics τ_{ad} are depicted in Figure 4.6. Both disturbances show a decaying behavior as well, which can be physically explained. The gravity gradient torque τ_{gg} arises from the gradient of the gravitational force along the satellite's body. Once the satellite is stabilized little effective torque is produced, with the x_B -axis being the axis of maximum moment of inertia pointing perpendicular to the gravitational force. About the x_B -axis, only little gravity gradient torque is produced in general, because the satellite is built symmetrically around this axis.

Similar statements apply to the aerodynamic torque. The stabilized satellite, facing the air flow with the smaller squared face is only affected by little aerodynamic torques τ_{ad} compared to the arbitrary orientation in the beginning.

4.2.1 Detumbling controller

Using the detumbling control law (3.4) with the described procedure to achieve time-optimal detumbling the angular velocity of the satellite is reduced until ω_{PD} is reached. In Figure 4.7, it is shown that the angular velocity decays in relatively short time. The detumbling controller takes about two hours to reduce the satellite's angular velocity from about $100^\circ/\text{s}$ to the limit of $0.29^\circ/\text{s}$. The oscillation of the angular rates $\omega_{BI,y}$ and $\omega_{BI,z}$

arises from the uneven moments of inertia and represents the nutation of the satellite.

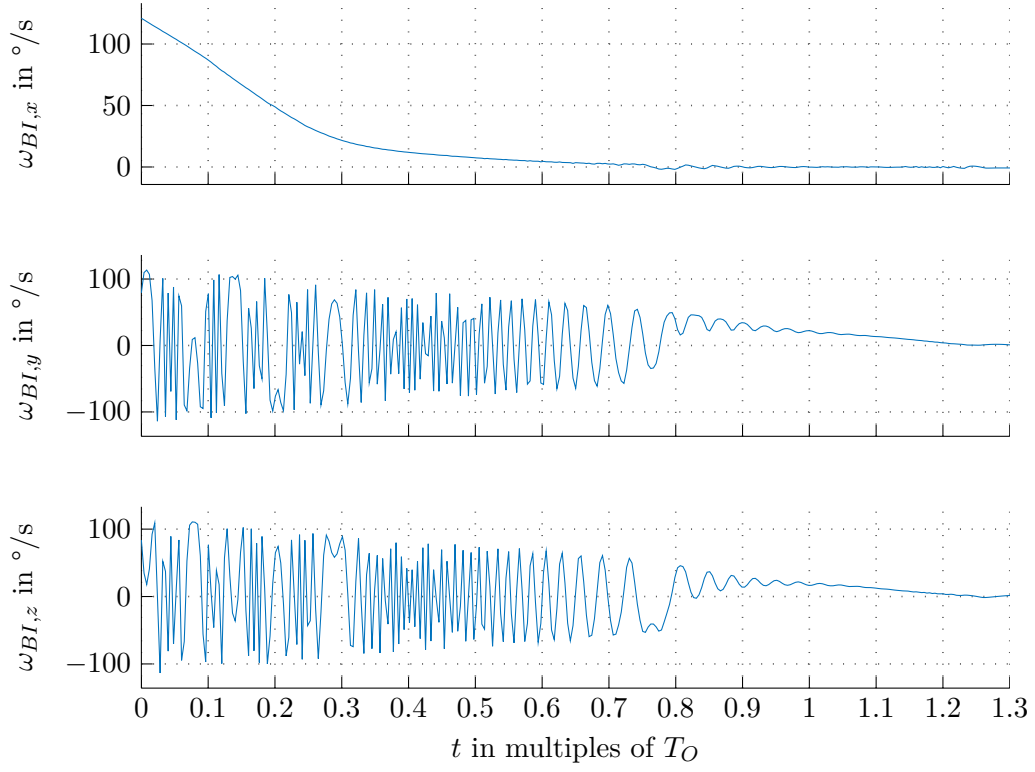


Figure 4.7: Angular velocity of the satellite w.r.t. the inertial frame for the detumbling phase.

Due to the bang-bang detumbling controller, one of the coil-currents is always at the maximum possible value of $i_{\max} = 100$ mA. This can be seen in Figure 4.8, where the power consumption is depicted as well. At $t \approx 1.3T_O$ the detumbling is completed and the algorithm is switched to the PD control law.

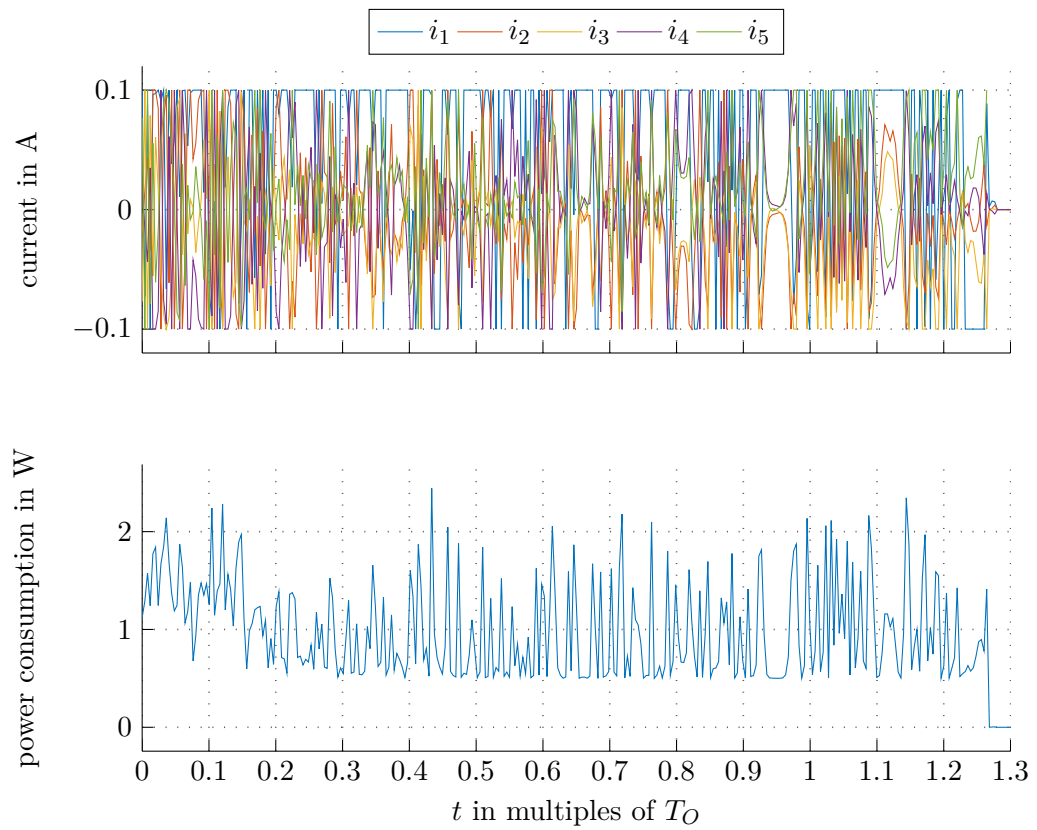


Figure 4.8: Current for each magnetorquer (upper graph) and the power consumption (lower graph) for the detumbling phase.

4.2.2 Attitude controller

The PD controller stabilizes the satellite on the desired trajectory (2.18). Since no direct attitude measurement is available on-board as described in Section 1.2, the satellite's attitude used in the PD control law (3.41) is provided by the Extended Kalman Filter. During periods where no Sun vector is measurable the control and estimation algorithm is switched off. This situation is determined by the intensity of the measured light. Although control is only available about $2/3$ of the time for each orbit, good control performance is achieved.

In Figure 4.9, the trend of the attitude error after switching to the PD control law (3.41) is shown for the time after switching until the requirements are met. The desired attitude (2.18) is reached in about $9T_O$ after switching and about $10T_O$ after detaching. Compared to the required $46T_O$ the control algorithm performs quite fast, thanks to the time-optimal detumbling. The gray areas in Figure 4.9 show the time periods where the satellite is in the Earth's shadow and the controller is disabled.

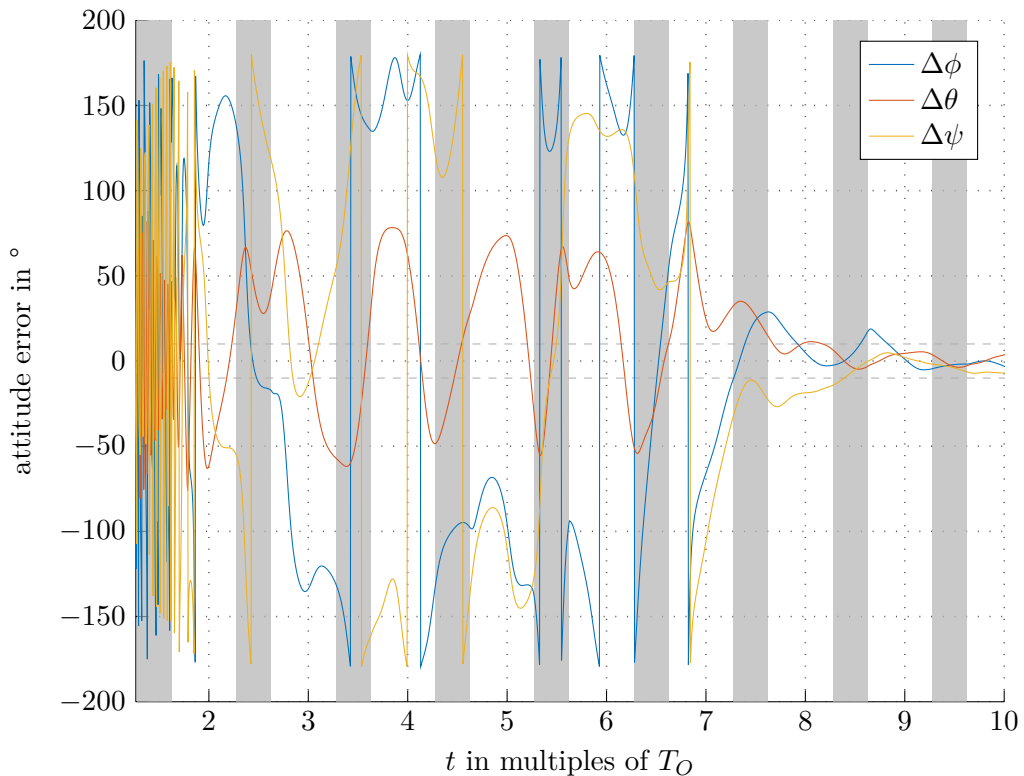


Figure 4.9: Attitude error in r.p.y. angles for the attitude control phase. The dashed lines show the required pointing accuracy.

The magnetorquer currents and power consumption for this period are shown in Figure 4.10. Figure 4.11 shows the related control torques. When the attitude controller takes over, the attitude error is rather high, more control action is required and therefore more power is consumed by the control algorithm. Once on the trajectory, the disturbance

torques are small as explained in Section 4.2 and the control action reduces significantly. Compared to the maximum possible current of $i_{\max} = 100 \text{ mA}$ the required control currents are very small and the current restrictions are clearly met.

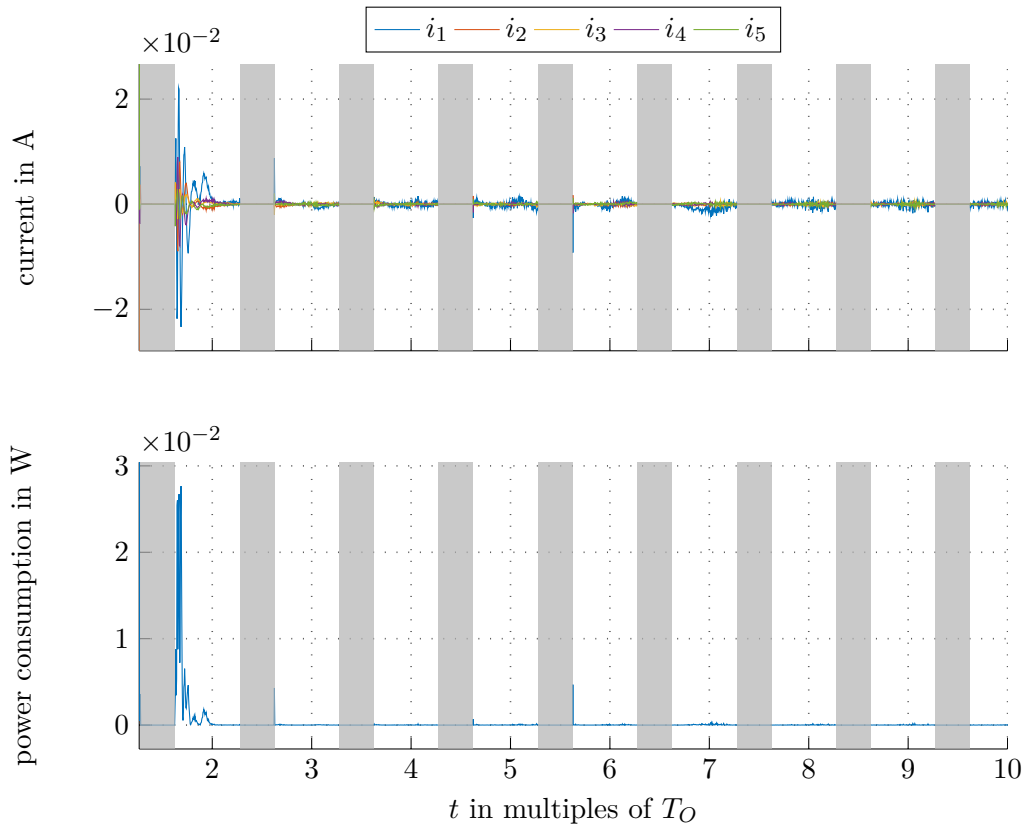


Figure 4.10: Current for each magnetorquer (upper graph) and the power consumption (lower graph) for the attitude control phase.

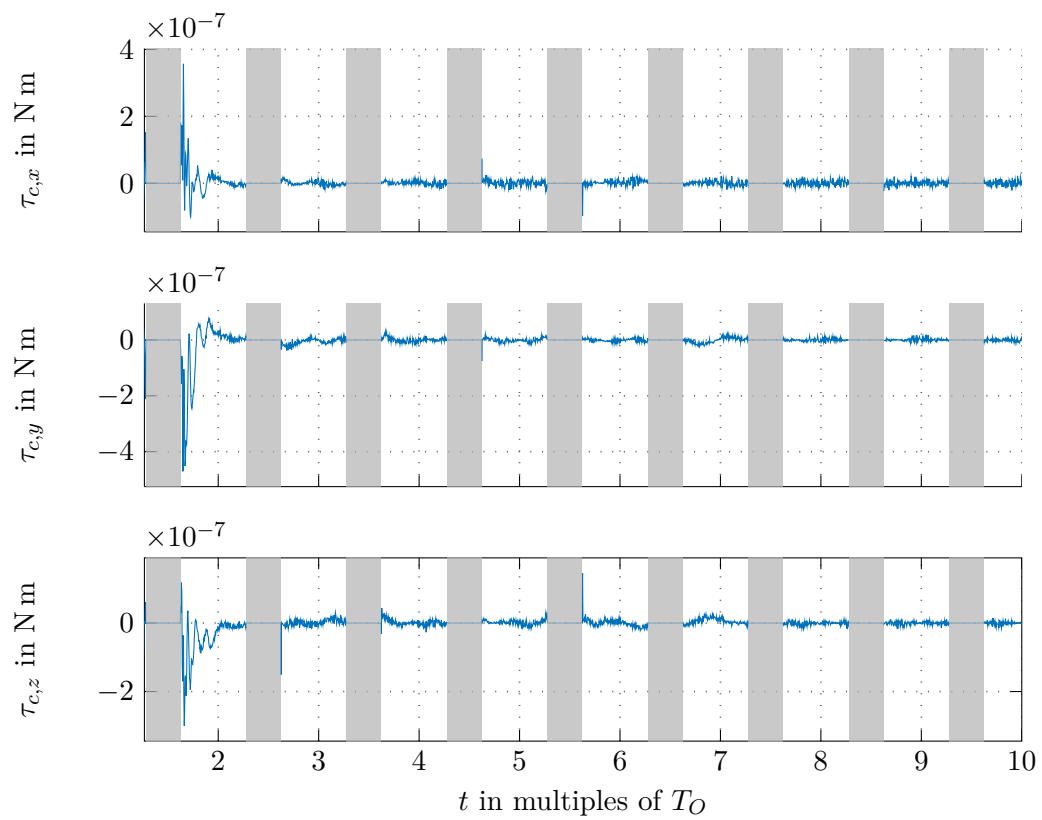


Figure 4.11: Control torques for the attitude control phase.

4.2.3 Enlarged view of stabilized flight

In Figure 4.12, the satellite's attitude compared to the desired trajectory is shown in detail, showing good confidence. Again the gray areas denote the times where the control algorithm is switched off. The related attitude errors are shown in Figure 4.13, proving that the accuracy fulfills the requirements of $\pm 10^\circ$.

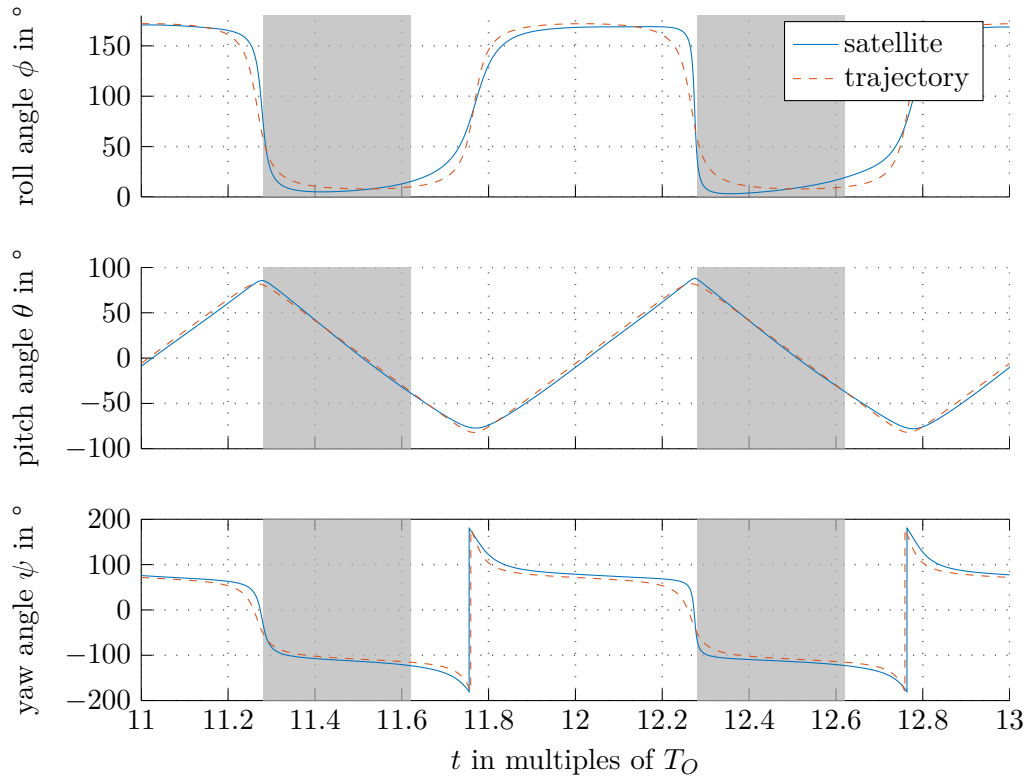


Figure 4.12: Attitude of the satellite w.r.t. the inertial frame, expressed in r.p.y. angles in a closer view.

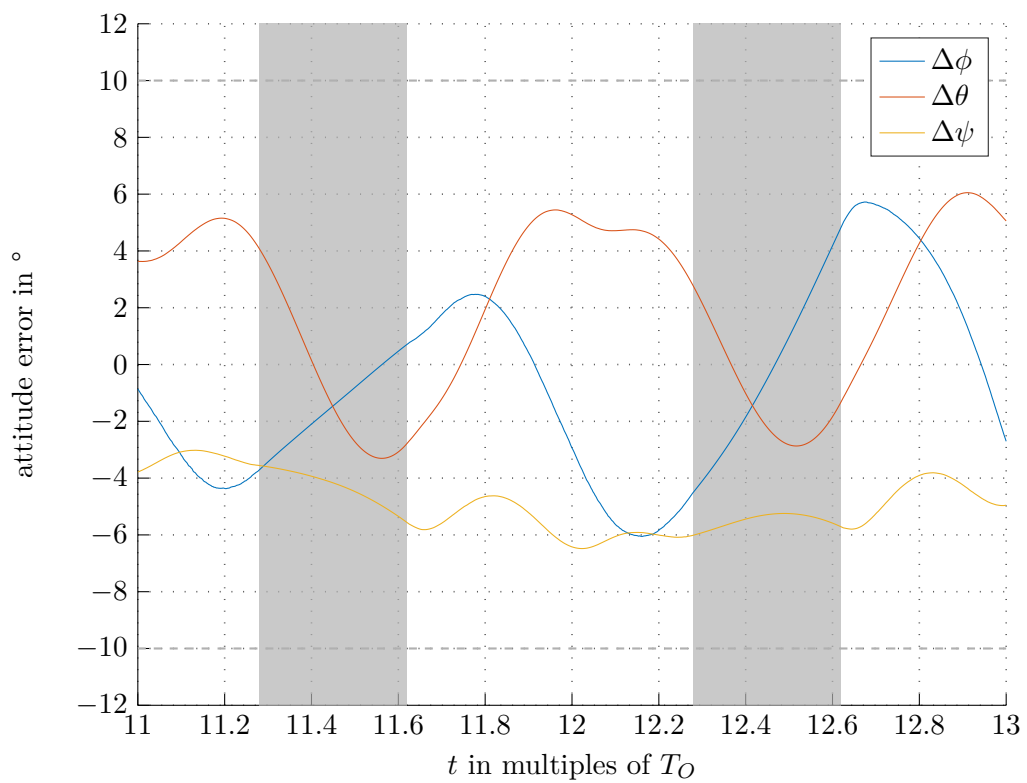


Figure 4.13: Attitude error in r.p.y. angles in a closer view.

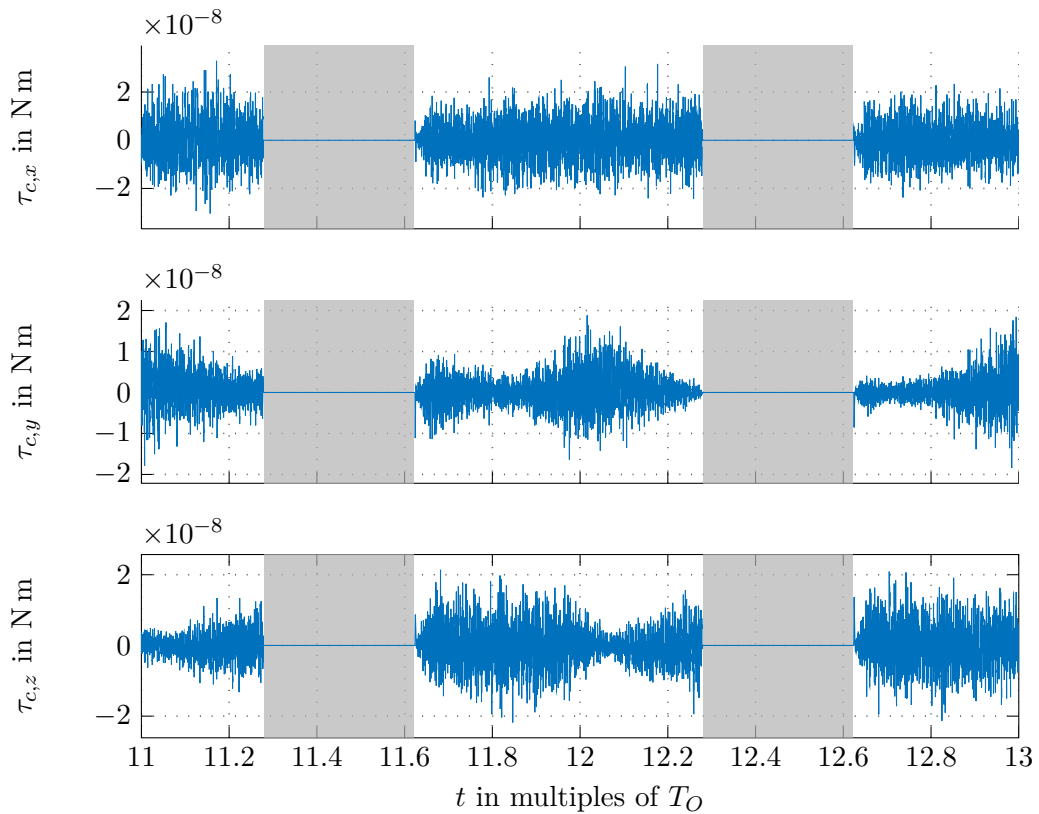


Figure 4.14: Control torque in the stabilized phase.

Figure 4.14 shows the control torques during the stabilized phase, where amplitudes up to $2 \cdot 10^{-8} \text{ N m}$ occur.

As described in Section 4.2, the disturbances acting on the satellite, if stabilized on the trajectory, are quite small compared to the possible control action. In Figure 4.15, the disturbances for this case are depicted. The disturbance torques show amplitudes up to $2 \cdot 10^{-9} \text{ N m}$, which is about 10 times smaller than the control torque generated by the magnetorquers.

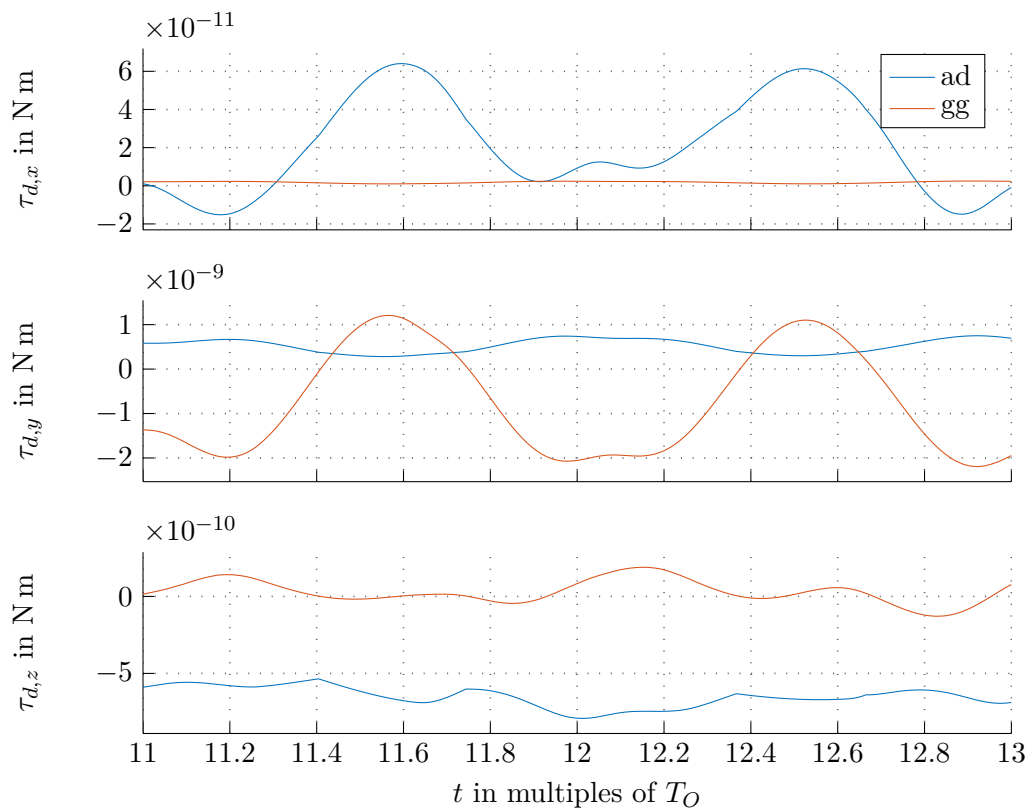


Figure 4.15: Gravity gradient and atmospheric drag acting on the satellite in a closer view.

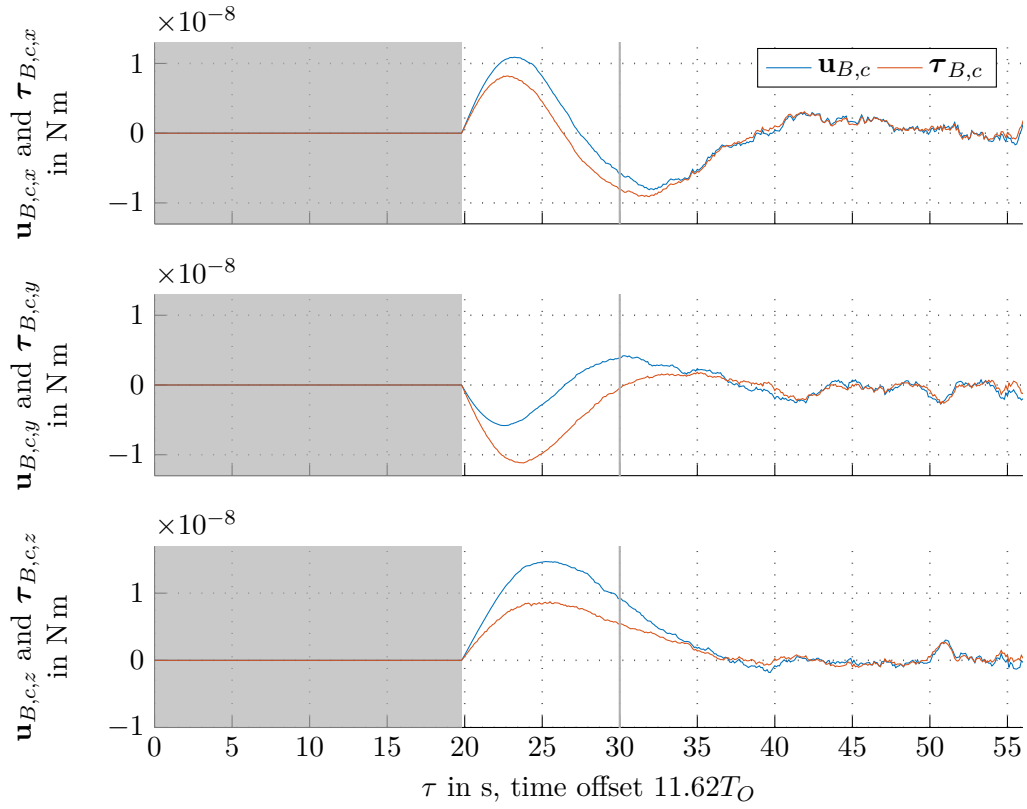


Figure 4.16: Comparison between the fully actuated torque and the projected torque.

As stated, the magnetic actuated satellite suffers from underactuation (cf. Chapter 1). In Figure 4.16, the difference between the desired control action denoted as $\mathbf{u}_{B,c}$ and the applied effective control torque $\boldsymbol{\tau}_{B,c}$ can be seen. Since Figure 4.16 shows a very short time period, a new time axis is introduced with τ for the following plots. The projection of the full torque $\mathbf{u}_{B,c}$ to the effective plane, which is perpendicular to the magnetic field $\tilde{\mathbf{b}}_B$, is depicted in Figure 4.17. The projection of the vectorial quantities are given for the time $\tau = 30$ s.

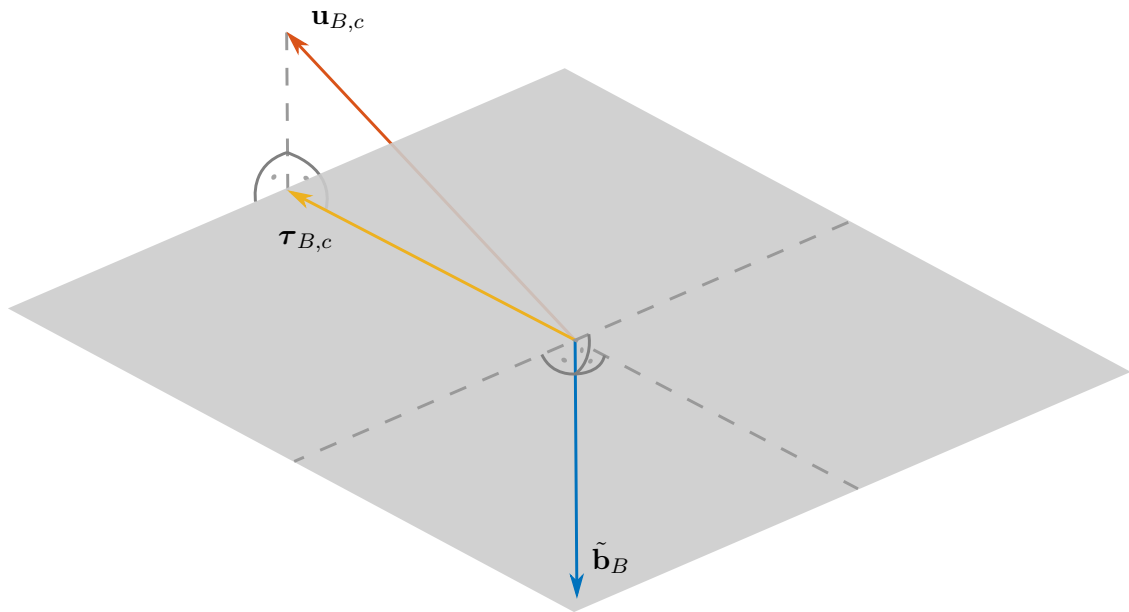


Figure 4.17: The projection of $\mathbf{u}_{B,c}$ to the effective plane, perpendicular to $\tilde{\mathbf{b}}_B$.

In Figure 4.18 and Figure 4.19, the behavior of the EKF for a restart after a period of Earth's shadow is shown. It takes about 20-30 seconds for the EKF to reduce the observer errors close to zero. Using two independent vector measurements, the attitude can be calculated instantaneously. The time lag arises from the smoothing of the EKF used to reduce noise. With the chosen set of gains from Table 4.7 a good compromise is given.

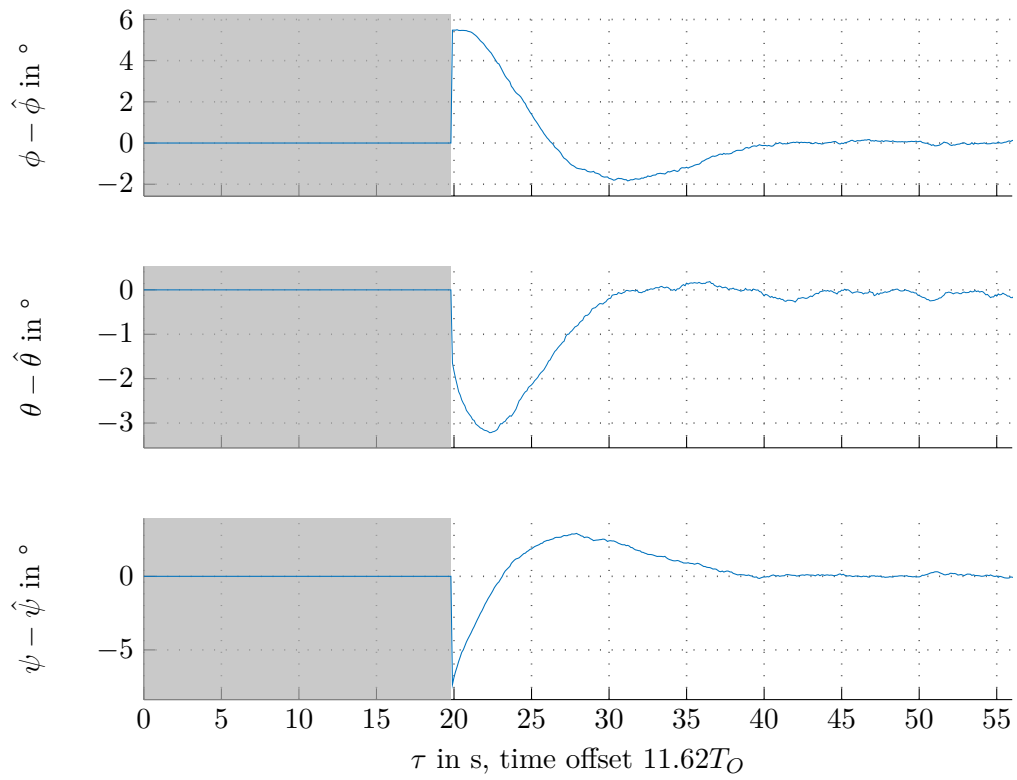


Figure 4.18: Estimation error of the estimated attitude after switching to the EKF.

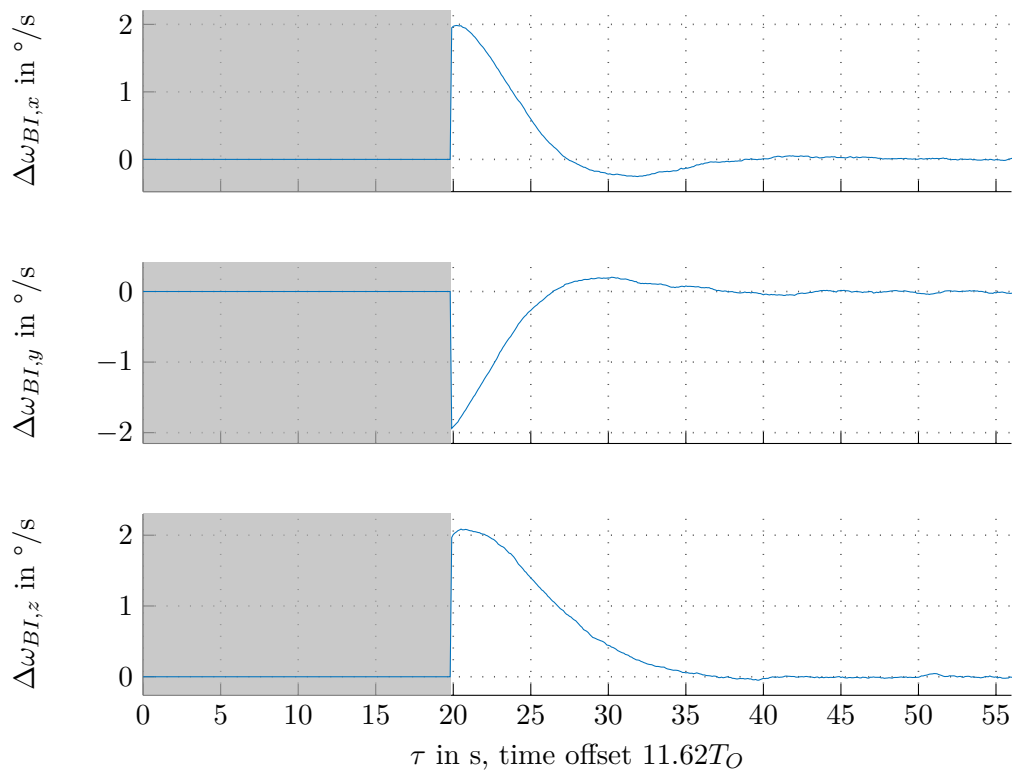


Figure 4.19: Error of the estimated angular velocities after switching to the EKF.

4.3 Chapter conclusion

The presented simulation results support the chosen control strategy. The given requirements of the *QB50* mission regarding the attitude control system are clearly satisfied. The required pointing accuracy of $\pm 10^\circ$ is achieved after a relatively short time and the long time plots show that the error stays within the required limits.

The power consumption of the control system clearly stays below the maximum possible values, what saves battery power.

5 Summary and outlook

The aim of this work was to develop an attitude control system for the *CubeSat Pegasus*. The models derived in Section 2.1 give a general description of the attitude dynamics of a rigid body. Together with the models of the disturbances acting on a spacecraft in low altitudes given in Section 2.3 a mathematical framework, describing the rotational motion of the given satellite, is obtained. These results serve as the basis for future satellite projects of the TU Wien *Space Team*. The presented idea of designing a magnetorquer layout and the given models for the sensors, which are widely used in the literature, completes the actuator and sensor description needed for the implementation of the attitude control system.

The derived attitude estimation and control strategy with the proof of stability represents one possibility to solve the attitude control problem for the particular class of satellites. The problem of underactuation, arising from the actuation principle using magnetic coils, is discussed in detail in Section 3.3. The underactuation was taken into account in the proof of stability for the attitude stabilization. Special attention was given to computational robustness of the system, meaning that regular software crashes should not harm the control performance seriously.

The simulation results of Chapter 4 with the included disturbances and measurement errors show that the satellite can be stabilized with the proposed control strategy under realistic conditions.

The most problematic part of the considered task was found to be the lack of Sun measurement when the satellite is located in the shadow of the Earth, resulting in the decision to switch off the control algorithms for about $1/3$ of each orbit. Using additional or different measurements like star trackers would help to get rid of this issue and improve the overall performance.

Using special aerospace hardware which is shielded against radiation instead of commercial off-the-shelf parts would reduce the probability of software crashes significantly. Without the risk of regular reboots, a control law depending on information from the past like Model Predictive Control could be used to enhance the performance. Aerospace hardware is much more expensive than commercial products and would require a multiple times higher project budget.

A Quaternion mathematics

The definitions of the quaternion mathematics are based on the introduction given in [31]. A profound analysis of the quaternion concept is given in [40] and [41].

Rotation quaternion definition

The rotational quaternion is defined as

$$\mathbf{q}(\mathbf{e}, \vartheta) = \begin{bmatrix} \cos\left(\frac{\vartheta}{2}\right) \\ \mathbf{e} \sin\left(\frac{\vartheta}{2}\right) \end{bmatrix} = \begin{bmatrix} q_0 \\ q_1 \\ q_2 \\ q_3 \end{bmatrix}, \quad (\text{A.1})$$

with the unit rotation axis \mathbf{e} and the rotation angle about this axis ϑ . Since the rotation axis \mathbf{e} is a unit vector with $\|\mathbf{e}\| = 1$, the rotation quaternion satisfies the constraint $\|\mathbf{q}\| = 1$. The elements of the four-dimensional quaternion can be subdivided into the scalar part q_0 and the vector part $\mathbf{q}_{1:3}$.

The identity quaternion, following from $\vartheta = 0$ is given by

$$\mathbf{q}_I = \begin{bmatrix} 1 \\ \mathbf{0} \end{bmatrix}, \quad (\text{A.2})$$

having a scalar part of 1 and zero vector part.

Quaternion product and cross product

A pair of quaternions $\mathbf{q}_a, \mathbf{q}_b$ is multiplied using the quaternion product operation \otimes defined as

$$\mathbf{q}_a \otimes \mathbf{q}_b = \begin{bmatrix} q_{a,0}q_{b,0} - \mathbf{q}_{a,1:3} \cdot \mathbf{q}_{b,1:3} \\ q_{a,0}\mathbf{q}_{b,1:3} + q_{b,0}\mathbf{q}_{a,1:3} - \mathbf{q}_{a,1:3} \times \mathbf{q}_{b,1:3} \end{bmatrix}, \quad (\text{A.3a})$$

with \cdot as the Euclidean inner product and the three-dimensional cross product \times .

Introducing the matrix representation of the quaternion and cross product, denoted by $[\otimes]$ and $[\times]$ gives

$$\mathbf{q}_a \otimes \mathbf{q}_b = [\mathbf{q}_a \otimes] \mathbf{q}_b = \begin{bmatrix} q_{a,0} & -\mathbf{q}_{a,1:3}^T \\ \mathbf{q}_{a,1:3} & q_{a,0}\mathbf{I}_3 - [\mathbf{q}_{a,1:3} \times] \end{bmatrix} \mathbf{q}_b, \quad (\text{A.3b})$$

with the three-dimensional identity matrix \mathbf{I}_3 . The three-dimensional cross product in matrix representation for a general vector $\mathbf{v}^T = [v_1 \ v_2 \ v_3]$ is defined as

$$[\mathbf{v}\times] = \begin{bmatrix} 0 & -v_3 & v_2 \\ v_3 & 0 & -v_1 \\ -v_2 & v_1 & 0 \end{bmatrix}, \quad (\text{A.3c})$$

representing a skew-symmetric matrix.

Conjugate and inverse quaternion

The conjugate \mathbf{q}^* is defined by changing the sign of the vector part $\mathbf{q}_{1:3}$ and leaving the scalar part q_0 unchanged

$$\mathbf{q}^* = \begin{bmatrix} q_0 \\ \mathbf{q}_{1:3} \end{bmatrix}^* = \begin{bmatrix} q_0 \\ -\mathbf{q}_{1:3} \end{bmatrix}. \quad (\text{A.4a})$$

The inverse of a quaternion \mathbf{q}^{-1} is defined as

$$\mathbf{q}^{-1} = \frac{\mathbf{q}^*}{\|\mathbf{q}\|^2}, \quad (\text{A.4b})$$

with the Euclidean vector norm $\|\cdot\|$.

The definition of the inverse quaternion ensures

$$\mathbf{q} \otimes \mathbf{q}^{-1} = \mathbf{q}_I, \quad (\text{A.4c})$$

as required for an inverse.

Considering that a rotational quaternion satisfies the constraint $\|\mathbf{q}\| = 1$ the inverse of a rotation quaternion is equal to its conjugate.

Rotation matrix representation of a rotation quaternion

The rotation quaternion \mathbf{q} can be represented as a rotation matrix $\mathbf{R}(\mathbf{q})$ using

$$\mathbf{R}(\mathbf{q}) = (q_0^2 - \|\mathbf{q}_{1:3}\|)\mathbf{I}_3 - 2q_0 [\mathbf{q}_{1:3}\times] + 2\mathbf{q}_{1:3}\mathbf{q}_{1:3}^T. \quad (\text{A.5})$$

Rotation of vectors

Rotating a general vector \mathbf{v} using the above definitions is calculated as

$$\mathbf{q} \otimes \begin{bmatrix} 0 \\ \mathbf{v} \end{bmatrix} \otimes \mathbf{q}^* = \begin{bmatrix} 0 \\ \mathbf{R}(\mathbf{q})\mathbf{v} \end{bmatrix}. \quad (\text{A.6a})$$

Defining the quaternion product as stated above allows for calculating sequences of rotations in the same order with rotation matrices and quaternions. A sequence of rotations (cf. [42]) represented as rotation matrices is given by

$$\mathbf{R}_{02} = \mathbf{R}_{01}\mathbf{R}_{12} , \quad (\text{A.6b})$$

where \mathbf{R}_{12} represents the rotational transformation from a coordinate frame 2 to a frame 1. Likewise \mathbf{R}_{01} rotates from frame 1 to frame 0. The two sequential rotations are multiplied to achieve a transformation from frame 2 to frame 0, denoted by \mathbf{R}_{02} .

The same sequence in quaternion representation reads as

$$\mathbf{q}_{02} = \mathbf{q}_{01} \otimes \mathbf{q}_{12} . \quad (\text{A.6c})$$

Quaternion product in exponential representation

Recalling the definition of the rotation quaternion allows to rewrite the quaternion product $[\mathbf{q}(\mathbf{e}, \vartheta) \otimes]$ as

$$[\mathbf{q}(\mathbf{e}, \vartheta) \otimes] = \cos\left(\frac{\vartheta}{2}\right) [\mathbf{q}_I \otimes] + \sin\left(\frac{\vartheta}{2}\right) \left[\begin{bmatrix} 0 \\ \mathbf{e} \end{bmatrix} \otimes \right] . \quad (\text{A.7a})$$

Expanding the sine and cosine in a Taylor series (cf. [56]) leads to the exponential representation of the quaternion product

$$[\mathbf{q}(\boldsymbol{\vartheta}) \otimes] = \sum_{j=0}^{\infty} \frac{\left[\begin{bmatrix} 0 \\ \frac{\boldsymbol{\vartheta}}{2} \end{bmatrix} \otimes \right]^{2j}}{(2j)!} + \sum_{j=0}^{\infty} \frac{\left[\begin{bmatrix} 0 \\ \frac{\boldsymbol{\vartheta}}{2} \end{bmatrix} \otimes \right]^{2j+1}}{(2j+1)!} = \exp\left(\left[\begin{bmatrix} 0 \\ \frac{\boldsymbol{\vartheta}}{2} \end{bmatrix} \otimes \right]\right) , \quad (\text{A.7b})$$

where $\boldsymbol{\vartheta} = \vartheta \mathbf{e}$ is the axis-angle vector, $x!$ denotes the factorial of x and $\exp()$ is the matrix exponential.

Small angle approximation of the rotation quaternion

With the assumption $\vartheta \ll 1$ the small angle approximation

$$\cos(\vartheta) \approx 1, \quad \sin(\vartheta) \approx \vartheta$$

is valid.

This argument, applied to the definition of the rotation quaternion, yields

$$\boldsymbol{\vartheta} = \vartheta \mathbf{e} \quad (\text{A.8a})$$

$$\mathbf{q}(\boldsymbol{\vartheta}) \approx \begin{bmatrix} 1 \\ \frac{\boldsymbol{\vartheta}}{2} \end{bmatrix} = \mathbf{q}_I + \begin{bmatrix} 0 \\ \frac{\boldsymbol{\vartheta}}{2} \end{bmatrix} , \quad \text{for } \vartheta \ll 1 . \quad (\text{A.8b})$$

Bibliography

- [1] *CubeSat Pegasus project homepage*, accessed 6th April 2016. [Online]. Available: <https://spaceteam.at/cubesat/>.
- [2] J. E. Oberright, „Nanosatellite science applications,“ in *Smaller Satellites: Bigger Business*, Dordrecht, Netherlands: Springer, 2002, pp. 83–91.
- [3] J. Bouwmeester and J. Guo, „Survey of worldwide pico- and nanosatellite missions, distributions and subsystem technology,“ *Acta Astronautica*, vol. 67, no. 7, pp. 854–862, 2010.
- [4] J. Hsu, *SpaceX raises \$1 billion from Google and Fidelity for satellite internet project*, accessed 6th April 2016. [Online]. Available: <http://spectrum.ieee.org/tech-talk/aerospace/satellites/spacex-raises-1-billion-from-google-fidelity-for-satellite-internet-project>.
- [5] S. Tsitas and J. Kingston, „6U CubeSat commercial applications,“ *Aeronautical Journal*, vol. 116, no. 1176, pp. 189–198, 2012.
- [6] *CubeSat project homepage*, accessed 6th April 2016. [Online]. Available: <http://www.cubesat.org/>.
- [7] *QB50 mission homepage*, accessed 6th April 2016. [Online]. Available: <https://www.qb50.eu/>.
- [8] C. Scharlemann, D. Birschitzky, H. Fuchs, L. Gury, S. Hauth, F. Kerschbaum, D. Kohl, C. Obertscheider, R. Ottensamer, T. Riel, B. Seifert, R. Sypniewski, M. Taraba, R. Trausmuth, and T. Turetschek, *PEGASUS - an Austrian nanosatellite for QB50*, Poster: European Geosciences Union General Assembly 2015, Vienna, Austria, Apr. 2015.
- [9] J. S. White, F. H. Shigemoto, and K. Bourquin, „Satellite attitude control utilizing the Earth’s magnetic field,“ DTIC Document, Tech. Rep., 1961.
- [10] J. S. White and Q. M. Hansen, „Study of systems using inertia wheels for precise attitude control of a satellite,“ *NASA TN D-691*, Apr. 1961.
- [11] M. Shigehara, „Geomagnetic attitude control of an axisymmetric spinning satellite,“ *Journal of Spacecraft and Rockets*, vol. 9, no. 6, pp. 391–398, 1972.
- [12] P. J. Camillo and F. L. Markley, „Orbit-averaged behavior of magnetic control laws for momentum unloading,“ *Journal of Guidance, Control, and Dynamics*, vol. 3, no. 6, pp. 563–568, 1980.
- [13] F. Martel, P. Pal, and M. Psiaki, „Active magnetic control system for gravity gradient stabilized spacecraft,“ in *Proceedings of the second annual AIAA/USU conference on small satellites*, Logan, USA, Sep. 1988, pp. 1–19.

- [14] J.-Y. Wen and K. Kreutz-Delgado, „The attitude control problem,“ *IEEE Transactions on Automatic Control*, vol. 36, no. 10, pp. 1148–1162, 1991.
- [15] A. Cavallo, G. De Maria, F. Ferrara, and P. Nistri, „A sliding manifold approach to satellite attitude control,“ in *Proceedings of the 12th World Congress, International Federation of Automatic Control*, vol. 5, Sydney, Australia, Jul. 1993, pp. 177–184.
- [16] O. Egeland and J.-M. Godhavn, „Passivity-based adaptive attitude control of a rigid spacecraft,“ *IEEE Transactions on Automatic Control*, vol. 39, no. 4, pp. 842–846, 1994.
- [17] C. I. Byrnes and A. Isidori, „On the attitude stabilization of rigid spacecraft,“ *Automatica*, vol. 27, no. 1, pp. 87–95, 1991.
- [18] H. Krishnan, M. Reyhanoglu, and H. McClamroch, „Attitude stabilization of a rigid spacecraft using two control torques: A nonlinear control approach based on the spacecraft attitude dynamics,“ *Automatica*, vol. 30, no. 6, pp. 1023–1027, 1994.
- [19] M. Reyhanoglu, A. Van der Schaft, N. H. McClamroch, and I. Kolmanovsky, „Dynamics and control of a class of underactuated mechanical systems,“ *IEEE Transactions on Automatic Control*, vol. 44, no. 9, pp. 1663–1671, 1999.
- [20] S. P. Bhat, „Controllability of nonlinear time-varying systems: Applications to spacecraft attitude control using magnetic actuation,“ *IEEE Transactions on Automatic Control*, vol. 50, no. 11, pp. 1725–1735, 2005.
- [21] K. L. Musser and W. L. Ebert, „Autonomous spacecraft attitude control using magnetic torquing only,“ in *Flight Mechanics/Estimation Theory Symposium*, NASA, Goddard Space Flight Center, USA, May 1989, pp. 23–38.
- [22] P. Wang and Y. B. Shtessel, „Satellite attitude control using only magnetorquers,“ in *Proceedings of the AIAA Guidance, Navigation and Control Conference and Exhibition*, IEEE, vol. 1, Boston, USA, Mar. 1998, pp. 222–226.
- [23] M. Krstic, P. V. Kokotovic, and I. Kanellakopoulos, *Nonlinear and adaptive control design*. New York, USA: John Wiley & Sons, Inc., 1995.
- [24] R. Wisniewski and M. Blanke, „Fully magnetic attitude control for spacecraft subject to gravity gradient,“ *Automatica*, vol. 35, no. 7, pp. 1201–1214, 1999.
- [25] H. K. Khalil, *Nonlinear systems*, 2nd ed. Upper Saddle River, USA: Prentice Hall, 1996.
- [26] M. Lovera and A. Astolfi, „Spacecraft attitude control using magnetic actuators,“ *Automatica*, vol. 40, no. 8, pp. 1405–1414, 2004.
- [27] A. Calloni, A. Corti, A. M. Zanchettin, and M. Lovera, „Robust attitude control of spacecraft with magnetic actuators,“ in *Proceedings of the American Control Conference (ACC)*, Montreal, Canada, Jun. 2012, pp. 750–755.
- [28] A. Zanchettin and M. Lovera, „ H_∞ attitude control of magnetically actuated satellites,“ in *Proceedings of the IFAC World Congress*, vol. 18, Milano, Italy, Aug. 2011, pp. 8479–8484.

- [29] M. Wood, W.-H. Chen, and D. Fertin, „Model predictive control of low earth orbiting spacecraft with magneto-torquers,“ in *Proceedings of the IEEE International Conference on Control Applications*, Munich, Germany, Oct. 2006, pp. 2908–2913.
- [30] F. Lizarralde and J. T. Wen, „Attitude control without angular velocity measurement: A passivity approach,“ *IEEE Transactions on Automatic Control*, vol. 41, no. 3, pp. 468–472, 1996.
- [31] F. L. Markley and J. L. Crassidis, *Fundamentals of Spacecraft Attitude Determination and Control*. New York, USA: Springer, 2014.
- [32] J. L. Crassidis, F. L. Markley, and Y. Cheng, „Survey of nonlinear attitude estimation methods,“ *Journal of Guidance, Control, and Dynamics*, vol. 30, no. 1, pp. 12–28, 2007.
- [33] R. E. Kalman and R. S. Bucy, „New results in linear filtering and prediction theory,“ *Journal of Basic Engineering*, vol. 83, no. 1, pp. 95–108, 1961.
- [34] F. L. Markley and D. Mortari, „How to estimate attitude from vector observations,“ in *Proceedings of the AAS/AIAA Astrodynamics Specialist Conference*, vol. 103, Girdwood, USA, Aug. 1999, pp. 1979–1996.
- [35] M. D. Shuster, „The QUEST for better attitudes,“ *The Journal of the Astronautical Sciences*, vol. 54, no. 3-4, pp. 657–683, 2006.
- [36] K. L. Jansen, K. H. Yabar, and J. T. Gravdahl, „A comparison of attitude determination methods: Theory and experiments,“ in *Proceedings of the 62nd International Astronautical Congress*, Cape Town, South Africa, Oct. 2011, pp. 3–7.
- [37] F. L. Markley, „Multiplicative vs. additive filtering for spacecraft attitude determination,“ in *Proceedings of the 6th Conference on Dynamics and Control of Systems and Structures in Space*, vol. 22, Riomaggiore, Italy, Jul. 2004, pp. 467–474.
- [38] J. R. Wertz, *Spacecraft attitude determination and control*, 1st ed. Dordrecht, Netherlands: Springer, 1978.
- [39] W. Steiner and M. Schagerl, *Raumflugmechanik*, 1st ed. Berlin Heidelberg, Germany: Springer, 2004.
- [40] R. Goldman, „Rethinking quaternions,“ in *Synthesis Lectures on Computer Graphics and Animation*, San Rafael, USA: Morgan & Claypool Publishers, 2010.
- [41] J. B. Kuipers, „Quaternions and rotation sequences,“ in *Proceedings of the International Conference on Geometry, Integrability and Quantization*, Sofia, Bulgaria, 2000, pp. 127–143.
- [42] M. Spong and S. Hutchinson, *Robot Modeling and Control*, 1st ed. New York, USA: Wiley, 2005.
- [43] J. Davis, *Mathematical modeling of earths magnetic field*, Technical Note, Virginia Tech, Blacksburg, USA, 2004.
- [44] A. Kugi, *Optimierung, lecture notes (WS 2014/15)*, Automation and Control Institute, TU Wien, Vienna, 2014.

- [45] A. Ali, L. Reyneri, J. de los Rios, H. Ali, and M. Mughal, „Reconfigurable magnetorquer for the CubePMT module of CubeSat satellites,“ in *Proceedings of the 5th International Multitopic Conference (INMIC)*, Islamabad, Pakistan, Dec. 2012, pp. 178–183.
- [46] J. Franklin, *Classical electromagnetism*. Boston, USA: Pearson, 2005.
- [47] D. Titterton and J. Weston, *Strapdown Inertial Navigation Technology, 2nd Edition*, ser. IEE radar, sonar, navigation, and avionics series. Herts, UK: Institution of Engineering and Technology, 2004.
- [48] M. Grewal and A. Andrews, „How good is your gyro [ask the experts],“ *IEEE Transactions on Control Systems*, vol. 30, no. 1, pp. 12–86, 2010.
- [49] D. R. Williams, *Moon and earth fact sheet*, accessed 6th April 2016. [Online]. Available: <http://nssdc.gsfc.nasa.gov/planetary/factsheet/moonfact.html>.
- [50] G. Avanzini and F. Giuliotti, „Magnetic detumbling of a rigid spacecraft,“ *Journal of Guidance, Control, and Dynamics*, vol. 35, no. 4, pp. 1326–1334, 2012.
- [51] M. Lovera and A. Astolfi, „Global magnetic attitude control of spacecraft in the presence of gravity gradient,“ *IEEE Transactions on Aerospace and Electronic Systems*, vol. 42, no. 3, pp. 796–805, 2006.
- [52] F. L. Markley, „Attitude determination using two vector measurements,“ *The Journal of the Astronautical Sciences*, vol. 48, no. 2, pp. 391–404, 1998.
- [53] N. Toda, J. Heiss, and F. Schlee, „Spars: The system, algorithms, and test results,“ in *Proceedings of the Symposium on Spacecraft Attitude Determination*, vol. 1, Aerospace Corp. Report TR-0066 (5306)-12, 1969, pp. 361–370.
- [54] A. Kugi, *Automatisierungstechnik, lecture notes (WS 2011/12)*, Automation and Control Institute, TU Wien, Vienna, 2011.
- [55] W. Kemmetmüller and A. Kugi, *Regelungssysteme 1, lecture notes (WS 2014/15)*, Automation and Control Institute, TU Wien, Vienna, 2014.
- [56] M. Hazewinkel, *Encyclopaedia of Mathematics (set)*, ser. Encyclopaedia of Mathematics. Dordrecht, Netherlands: Springer, 1994.
- [57] J. Elstrodt, *Maß- und Integrationstheorie*, 7th ed. Berlin Heidelberg, Germany: Springer, 2006.
- [58] R. T. Boute, „The euclidean definition of the functions div and mod,“ *ACM Transactions on Programming Languages and Systems (TOPLAS)*, vol. 14, no. 2, pp. 127–144, 1992.

Eidesstattliche Erklärung

Hiermit erkläre ich, dass die vorliegende Arbeit gemäß dem Code of Conduct – Regeln zur Sicherung guter wissenschaftlicher Praxis (in der aktuellen Fassung des jeweiligen Mitteilungsblattes der TU Wien), insbesondere ohne unzulässige Hilfe Dritter und ohne Benutzung anderer als der angegebenen Hilfsmittel, angefertigt wurde. Die aus anderen Quellen direkt oder indirekt übernommenen Daten und Konzepte sind unter Angabe der Quelle gekennzeichnet. Die Arbeit wurde bisher weder im In- noch im Ausland in gleicher oder in ähnlicher Form in anderen Prüfungsverfahren vorgelegt.

Wien, am 7. April, 2016

Martin Meiringer